Numerical simulation on the transport phenomena in microclimates near the skin

Master's Dissertation in Bioengineering

by

Dinis Soares Reis de Oliveira

Institution where research was performed:

Laboratory of Protection and Physiology (401)

EMPA St. Gallen — Switzerland

Institution granting the degree:

Department of Chemical Engineering

Faculty of Engineering, University of Porto

Supervisors:

Dr. Tiago Sotto Mayor, EMPA St. Gallen

Dr. Manuel Vieira Simões, University of Porto

Porto, February 2015.

"I promise nothing complete;
because any human thing supposed to be complete,
must for that very reason infallibly be faulty."

Herman Melville,
Moby Dick, or The Whale

To every Teacher,
both in School and in Life.

Abstract

The microclimate between skin and clothing plays a central role in heat transfer and consequently influences thermal comfort, which can affect the wearer's performance. Both experimental and numerical tools are available to study phenomena occurring in the microclimate. Numerical tools enable independent control over phenomena, as well as to obtain more detailed information, both in space and in time.

The current numerical study focuses on dry heat transfer (conduction; natural and forced convection; radiation) in the microclimate between skin and a parallel layer of fabric. The microclimate is represented by a 2D air-filled 4:1 rectangular enclosure, heated from one of its long edges (isothermal wall, skin) and cooled by forced convection imposed in an external domain. The latter is separated from the internal one by an impermeable fabric. Computational Fluid Dynamics (CFD) laminar-regime simulations were run, using a Finite Volume Method (FVM) commercial code. Two-dimensional stationary fields were assumed.

Effects of altering external air velocity, air gap thickness and emissivity of the inner surface of the fabric were in good agreement with those previously obtained by the team at EMPA. As a central topic, we analyse the effects of varying the inclination of the enclosure, θ, and the thermal resistance of the fabric, R_{CT}.

In vertical enclosures (vertical isothermal wall), natural convection in the microclimate was observed for every air gap thickness (down to 8 mm). However, for a higher air gap thickness of 52 mm, convective Nusselt number (Nu_{conv}) in the enclosure was higher for low inclinations (i.e. closer to horizontal position), corresponding to the multi-cell flow mode. Nu_{conv} was slightly higher for negative θ (ascending external air), probably due to the assisting effect of external natural convection on forced convection. The internal flow affected the thickness of external thermal layers, which varied non-monotonically along the length of the fabric, causing waviness in profiles of external local convective heat transfer coefficient. These oscillations were lessened for higher thermal resistance of the fabric. Finally, it was

relevant to consider radiative heat transfer, since it has the potential to significantly impact temperature fields and other studied variables.

Keywords

CFD (Computational Fluid Dynamics), clothing microclimates, air gaps, buoyancy-driven flows, fluid flow, heat transfer, radiation.

Sumário

O microclima entre pele e vestuário tem um papel central na transferência de calor e influencia, consequentemente, o conforto térmico e o desempenho do utilizador. Existem ferramentas experimentais e numéricas que nos permitem estudar fenómenos neste microclima. Os métodos numéricos permitem controlar cada fenómeno de forma independente, bem como obter informação espacial e temporal mais detalhada.

O presente estudo numérico foca-se na transferência de calor seco (condução; convecção natural e forçada; radiação) no microclima localizado entre a pele e uma camada paralela de tecido têxtil. O microclima representa-se por uma cavidade bi-dimensional e rectangular 4:1, contendo ar, aquecida por uma das fronteiras longas (parede isotérmica, ou pele) e arrefecida por convecção forçada, imposta num domínio externo. O último encontra-se separado do domínio interno por um tecido impermeável. Simulações em regime laminar em CFD (*Computational Fluid Dynamics*) foram executadas num código commercial, usando o Método de Volumes Finitos (FVM). Assumiram-se campos bi-dimensionais estacionários.

Os efeitos da alteração da velocidade do ar externo, espessura do intervalo de ar e emissividade interna do tecido encontram-se de acordo com resultados anteriormente obtidos pela equipa no EMPA. Como assunto central do presente estudo, analisamos os efeitos da alteração da inclinação do microclima, θ, e da resistência térmica do tecido, R_{CT}.

Em cavidades verticais (parede isotérmica vertical), observou-se a ocorrência de convecção natural no microclima para todas as espessuras do intervalo de ar (espessura mínima de 8 mm). No entanto, para uma espessura de 52 mm, o Nusselt convetivo (Nu_{conv}) foi superior para valores baixos de inclinação (i.e. próximo da situação horizontal), correspondendo ao modo de escoamento com múltiplas células convetivas. O Nu_{conv} foi ligeiramente superior para inclinações negativas (ar externo ascendente), provavelmente devido à soma dos efeitos da convecção natural externa aos da convecção forçada. Observou-se que o escoamento interno afeta a espessura das camadas térmicas externas, a qual varia ao longo do comprimento do tecido de

forma não monotónica, causando oscilações nos perfis do coeficiente convetivo de transferência de calor. Estas oscilações diminuíram com um aumento na resitência térmica do tecido. Por fim, a inclusão da radiação no modelo foi relevante, uma vez que tem o potencial de alterar significativa-mente os campos de temperatura e outras variáveis em estudo.

Palavras-chave

CFD (Computational Fluid Dynamics), microclimas em vestuário, espaçamentos de ar, conveção natural, escoamento de fluídos, transferência de calor, radiação.

Acknowledgements

The author of this dissertation would like to acknowledge Dr. Tiago Sotto Mayor, at EMPA St. Gallen (Switzerland), for his attentive support and collaboration, namely for the valuable discussions that culminated in the current work. Acknowledgements are also due to Professor Manuel Simões, at Faculty of Engineering of University of Porto (Portugal).

The author would also like to acknowledge EMPA, for its financial support and for offering the possibility for a unique and enriching experience in a high quality Swiss research institution.

Last but not least, the author would also like to give his warm thanks to his family and friends, the later both in Portugal as in Switzerland, in particular to the very welcoming people at EMPA St. Gallen. Without their support, none of this would be possible.

Nomenclature

AR	Aspect ratio: L/H	[—]
B	Bias factor (ANSYS Meshing): ratio between largest and smallest elemental grid edge in a given direction	[—]
C_2	Inertial resistance factor	[m^{-1}]
C_p	Specific heat capacity	[J kg^{-1} K^{-1}]
D	Characteristic length for Re, Nu and Da	[m]
Da	Darcy number: K/D^2	[—]
E	Total energy	[J/kg]
$\vec{F}$	Force vector	[N]
F_{12}	View factor between segment 1 and 2	[—]
g	Gravitational acceleration	9.81 m s^{-2}
H	Length in the y-direction	[m]
h	Sensible enthalpy	[J /kg]
J	Mass flux	[kg m^{-2} s^{-1}]
k	Thermal conductivity	[W m^{-1} K^{-1}]
K	Permeability (reciprocal of viscous resistance)	[m^2]
K_o	Kozeny constant	[—]
L	Length in the x-direction	[m]
n	Total number of elements in a grid or, if direction is specified, number of elements along one edge.	[—]
Nu	Nusselt number, generically: hD/k	[—]
p	Pressure	[Pa]
Pr	Prandtl number: $\nu/\alpha = \mu C_p/k$	[—]
q	Heat flux	[W m^{-2}]
Q	Heat transfer rate	[W]
R	Radius	[m]
R_{CT}	Thermal resistance for a flat fabric: $R_{CT} = H_{th}/k_s$	[K m^2 W^{-1}]
Ra	Rayleigh number: $Ra = \beta g(T_h - T_c)H^3\rho^2 Pr/\mu^2$	[—]
Re	Reynolds number: $UD/\nu = \rho UD/\mu$	[—]
S_o	Shape factor, quotient between surface area and volume of solid phase in a porous medium	[—]
t	Time	[s]
T	Temperature	[K]
u, v, w	Physical velocity component in the x-, y- and z-direction	[m s^{-1}]
U	Physical velocity	[m s^{-1}]
x, y, z	Coordinate values in space	[m]

α	Thermal diffusivity: $k/(\rho C_p)$	[$m^2\ s^{-1}$]
β	Thermal expansion coefficient	[K^{-1}]
γ	Porosity, ratio between volume of fluid and volume of solid	[—]
ε	Emissivity	[—]
μ	Dynamic viscosity	[Pa s]
ν	Kinematic viscosity	[$m^2\ s^{-1}$]
ρ	Density	[$kg\ m^{-3}$]
σ	Stefan-Boltzmann constant	5.6697×10^{-8} $W\ m^{-2}\ K^{-4}$
θ	Inclination angle, between the vector normal to the inner fabric surface and the gravitational acceleration.	[º]

Subscripts:

∞	far field (free stream)
avrg	average
c	cold
conv	convective
cr	critical
e	entry
E	effective
f	fluid
glob	global
h	hot
in	inlet
max	maximum
min	minimum
rad	radiative
ref	reference value
s	solid
t	thermal
th	thickness
w	wall
x	Reynolds number based on the *x* value (flat plates)
z	in depth

Contents

Figures and Tables

1. Introduction

Thermal comfort is an important issue in protective clothing applications, especially since it can affect the wearer's performance (Rossi, 2005). It is therefore essential to have a better understanding on the relation between different heat transfer phenomena occurring in clothing systems. This can be achieved by use of both experimental (guarded hotplates, thermal manikins and human trials) and numerical approaches (Computational Fluid Dynamics; Couto & Mayor, 2013). The current study concerns the numerical simulation of dry heat transfer in the microclimate between the skin and one layer of fabric.

1.1. Outline and Scope of the Thesis

The current thesis is fundamentally organized into three parts: 1) a brief introduction to the subject of study, identification of the current contribution and stating of modelling assumptions (*Introduction*); 2) description of the modelling procedures (*Materials and methods*); and finally 3) presentation and discussion of current results (*Results and discussion*).

Apart from 3D modelling of the whole body or limb, numerical simulation of heat transfer in clothing systems usually resources to one of two basic configurations: the flat geometry (Figure 1a) and the concentric geometry (Figure 1b). The complete project developed at EMPA for this dissertation concerned both geometries, by analysing both steady-state laminar simulations on a flat geometry (Figure 1a, continuing the work developed at EMPA by Couto & Mayor, 2013) and transient turbulent simulations on a concentric geometry (Figure 1b, building on the initial work of Sobera (2006), though adding the effects of radiation). For reasons of space limits and in order to keep the discussion on the observed phenomena as coherent and detailed as possible, the current thesis will exclusively deal with results obtained for the flat geometry (Figure 1a). The later configuration is thoroughly described in sub-section *1.3. Contribute of the current study*.

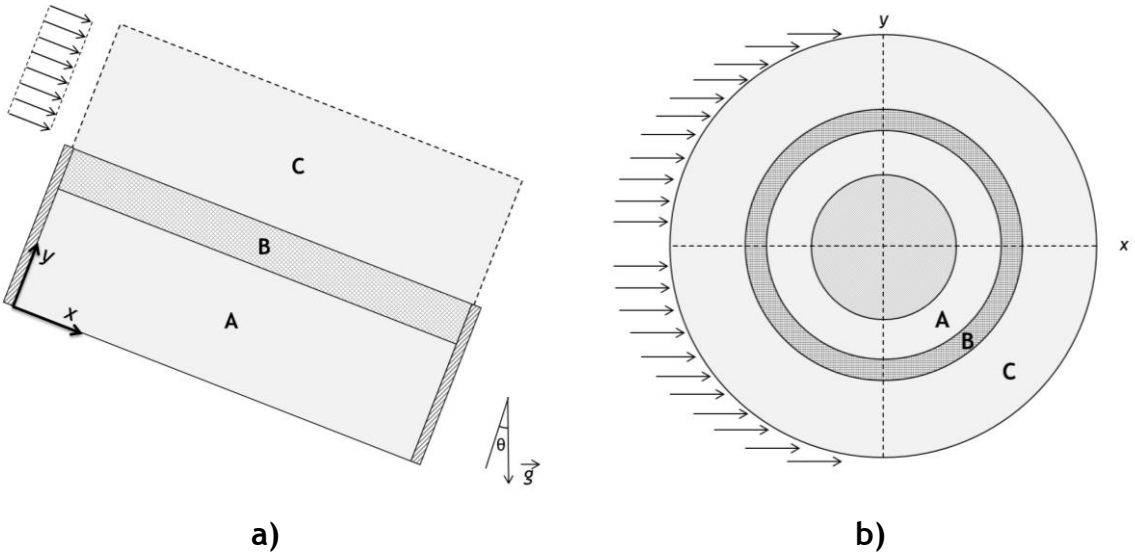

Figure 1 – Examples of different geometries used in numerical simulation of heat transfer in microclimates near the skin: a) flat geometry; **b)** concentric geometry. Domains A, B and C correspond to the microclimate, the fabric and the external domain, respectively. Drawings do not take scale or aspect ratio into account.

1.2. State-of-the-art of numerical simulation approaches

One of the most valuable advantages of numerical methods, as compared to experimental approaches, corresponds to the ability of independently controlling each phenomenon and obtaining detailed spatial and temporal information (Barry et al., 2003). Therefore, the mechanism underlying a given process can be studied and design guidelines can be drawn. Still, Computational Fluid Dynamics (CFD) approaches require validation, which relies on either experimental data or analytical solutions (Neale, Derome, Blocken, & Carmeliet, 2007).

Modelling of heat transfer in microclimates located between the skin and the first layer of clothing by use of CFD tools includes simulation of phenomena such as convective and radiative heat transfer (Couto & Mayor, 2013), as well as sweat-related heat transfer (Barry et al., 2003). The present study focuses on dry phenomena in flat setups (conduction, convection and radiation), whereas latent heat and mass transfer are addressed elsewhere (Barry & Hill, 2003; Min et al., 2007; Murakami et al., 2000).

The topic of natural convection has been extensively studied, both numerically and experimentally. This is mainly due to its importance in many applications, from electronic devices (Tari & Mehrtash, 2013) to solar collectors and facade elements in buildings (Manz, 2003). Main issues discussed in the literature concern the influence of several factors on heat transfer in fluid-filled enclosures, including the aspect ratio of the enclosure, initial solution conditions, boundary conditions, inclination of the enclosure relative to gravity and coupling of radiation models.

Corcione (2003) studied the effect of both boundary conditions and aspect ratio (*AR* from 0.66 to 8) upon flow patterns and local heat fluxes in air-filled enclosures. Soong & Tzeng (1996), and more recently Khezzar et al. (2012), studied the effects of inclination relative to gravity upon flow patterns and Nusselt number, *Nu* (ratio between transferred heat and that corresponding to hypothetical pure conduction). The later authors also addressed the hysteresis effect, i.e. the change in the critical inclination (corresponding to transition between flow-modes) as a function of increasing or decreasing inclination, a phenomenon that is fundamentally related to initial solution conditions (Khezzar et al., 2012; Soong & Tzeng, 1996). Additionally, the interaction between natural convection and radiation in square enclosures was studied by Akiyama & Chong (1997) for square enclosures, and, for higher aspect ratios and different inclinations, by Vivek et al. (2012). Each of these authors considers active walls either as isothermal or with a constant heat flux. However, as Couto & Mayor (2013) noted before, in order to better understand heat transfer in the microclimate between skin and clothing, both internal and external environments should be modelled. This means that the temperature of the fabric (corresponding in other studies to a cold isothermal wall) should be allowed to vary along its length.

Furthermore, for non-flat geometries (e.g., Figure 1b), it might become relevant to model the fabric as a porous region, thus allowing air to permeate it. Porous materials are present in a variety of physical processes, from industrial filtration processes and packed-bed reactors, to ground-water hydrology and thermal insulation in buildings. Theory behind porous media flow dates back at least to the nineteenth century, when Darcy described the pressure drop across a porous membrane

as a linear function of fluid velocity. He thus established the well-known Darcy's law (Dunn, 2000), given by:

$$\frac{\Delta P}{H_{th}} = \frac{\mu}{K} \times U \qquad \text{Equation 1}$$

where permeability *K*, in units of area, is still dependent on properties of the material, such as porosity and pore geometry (Dunn, 2000).

Textiles in clothing are classified as fibrous (Sobera, 2006) and there are currently three groups of mathematical models for describing flow in such materials (as presented by Gooijer et al., 2003): **pore models**, such as the Carman-Kozény model (Van Den Brekel & De Jong, 1989); **drag models**, which describe the flow as one through a system of discrete cylinders (Sobera, 2006) and **orifice models**, which account for flow resistance by a discharge coefficient – a particularly suitable approach when dealing with monofilament fabrics (Gooijer et al., 2003; Wang et al., 2007).

Pore models were originally created to model permeability, *K* (Gooijer et al., 2003). An example is the Carman-Kozény model, given by (Dunn, 2000):

$$K = \frac{1}{K_o {S_o}^2} \times \frac{\gamma^3}{(1-\gamma)^2} \qquad \text{Equation 2}$$

where a value of K_o (Kozeny constant) of 5.5 is referred to as representative of most porous media (Van Den Brekel & De Jong, 1989). Later, MacGregor adapted Eq. 2 for textile beds composed of circular fibres with diameter *d* (Dunn, 2000):

$$K = \frac{d^2}{16\, K_o} \times \frac{\gamma^3}{(1-\gamma)^2} \qquad \text{Equation 3}$$

Since Darcy's law disregards boundary and inertial forces exerted by the solid on the fluid (Vafai & Tien, 1981), non-Darcy models have been introduced, which add a squared-velocity term to Eq.1, yielding (ANSYS, 2013b, p. 225):

$$\frac{\Delta P}{L_{th}} = \frac{\mu}{K} \times U + \frac{\rho_f}{2} \times C_2 \times U^2 \qquad \text{Equation 4}$$

where C_2 corresponds to the inertial resistance factor, in m^{-1} (ANSYS, 2013b, p. 236).

Computational Fluid Dynamics (CFD) enables the simulation of phenomena in porous media and this is usually done according to one of three different approaches: the micro-, meso- and macro-scale approach (Sobera, 2006). While the first aims at modelling permeability and inertia resistance factors (or discharge coefficients) by

solving Navier-Stokes equations at the scale of the micro-structure (Andrade et al., 1999; Angelova et al., 2013; Döbrich et al., 2014; Rief et al., 2011; Sobera, 2006; Wong et al., 2006), the second and third approaches apply the *a priori* derived parameters (K and C_2) to model velocity, pressure and temperature fields by use of macroscopic numerical representations of the porous region (Lauriat & Prasad, 1989; Sobera, 2006; Vafai & Tien, 1981).

Finally, there are situations when, due to the orientation of the fabric relative to the external air flow, no significant flow is expected to permeate the fabric. Thus, in such situations, as e.g. in the case of the flat geometry of Figure 1a, the fabric can be assumed as impermeable to air (Couto & Mayor, 2013).

1.3. Contribute of the current study

This study builds on a configuration previously presented by Couto & Mayor (2013), which represents conditions normally encountered in microclimates between skin and clothing, as depicted in Figure 1a. A rectangular air-filled enclosure (domain A) is heated by an isothermal wall (coincident with the x-axis) representing the human skin. This enclosure has two adiabatic sidewalls. Heat is transferred from the internal domain A to the external domain C through a heat-conducting, impermeable fabric (domain B). Forced air convection is imposed in the exterior domain C, where inlet air flows parallel to the fabric.

The aim of the present study consists in evaluating cases in which the inclination of this enclosure is changed from the horizontal position ($\theta = 0^o$, as in Couto & Mayor, 2013) to the vertical position ($\theta = 90^o$ or $\theta = -90^o$, for descending or ascending external air, respectively) and beyond, to an inverted enclosure ($\theta = \pm 180^o$). This is achieved by analysing the influence of inclination on transferred heat and flow patterns. Additionally, other factors are analysed, such as external air velocity, geometry of the enclosure (air gap thickness), emissivity of the inner surface of the fabric and thermal resistance of the fabric.

To the best of our knowledge, such study is lacking in the current literature for this combination of boundary conditions and geometry, and may contribute to a

better understanding of dry heat transfer in the microclimate located between skin and clothing. The current approach covers cool-weather applications, assuming that thermal effects of sweating can be disregarded, i.e. low levels of user's physical activity. In particular, it relates to conditions in which external natural convection or forced parallel air drafts exist (e.g. in a room with an air-conditioning system).

1.4. Modelling assumptions and mathematical formulation

Stationary two-dimensional simulations were carried out, assuming that computed variables do not change over time (Couto & Mayor, 2013; Vivek et al., 2012) and that the third dimension is large enough (Couto & Mayor 2013).

Constant physical properties were attributed to the fluid, using average temperature values in estimating air properties (Çengel, 2003b, p. 370). Additionally, air was considered as an incompressible fluid, since the pressure of the gas is not expected to vary by more than 20% (Coulson & Richardson, 1999, p. 143) and air velocity is inferior to 10% the velocity of sound, i.e. Mach number is inferior to 0.1 (ANSYS, 2011a, p. 14).

In every simulation, the Boussinesq approximation was adopted in simulating natural convection, which means that the fluid properties are considered constant in all solved equations, except for the buoyancy force. This approximation is valid for relatively low temperature differences within the simulation domain (ANSYS, 2013b, p. 766). Specifically, this approximation is valid when $\beta(T - T_{ref}) \ll 1$ (ANSYS, 2013b, p. 766), which is considered to be the case for the current study, since $\beta(T - T_{ref})$ is always below 0.05.

Assuming an incompressible fluid, the mass conservation equation (continuity equation) corresponds to (ANSYS, 2011a, p. 2):

$$\nabla . \vec{U} = 0 \qquad \text{Equation 5}$$

The momentum equation, as applied to the present study, can be written as (ANSYS, 2011a, p. 3, 2013b, p. 766):

$$\boldsymbol{\rho_{ref}} \cdot \left(\boldsymbol{\nabla} \cdot \vec{\boldsymbol{U}}\right) \cdot \vec{\boldsymbol{U}} = \boldsymbol{\nabla} \cdot \left(-\boldsymbol{p} + \boldsymbol{\mu}\left(\boldsymbol{\nabla}\vec{\boldsymbol{U}} + \left(\boldsymbol{\nabla}\vec{\boldsymbol{U}}\right)^{\boldsymbol{T}}\right)\right) + \vec{\boldsymbol{F}} \qquad \text{Equation 6}$$

where the last term concerns buoyancy forces. This buoyancy term is given according to the Boussinesq approximation by (ANSYS, 2013b, p. 766):

$$\vec{\boldsymbol{F}} = \left(\boldsymbol{\rho} - \boldsymbol{\rho_{ref}}\right)\vec{\boldsymbol{g}} = -\boldsymbol{\rho_{ref}}\boldsymbol{\beta}(\boldsymbol{T} - \boldsymbol{T_c})\vec{\boldsymbol{g}} \qquad \text{Equation 7}$$

The energy equation was enabled, corresponding to (ANSYS, 2011a, p. 140):

$$\boldsymbol{\nabla} \cdot \left[\vec{\boldsymbol{U}}\left(\boldsymbol{\rho_{ref}}\boldsymbol{E} + \boldsymbol{p}\right)\right] = \boldsymbol{\nabla} \cdot \left[\boldsymbol{k}\boldsymbol{\nabla}\boldsymbol{T} - \boldsymbol{h}\boldsymbol{J} + \boldsymbol{\mu}\left(\boldsymbol{\nabla}\vec{\boldsymbol{U}} + \left(\boldsymbol{\nabla}\vec{\boldsymbol{U}}\right)^{\boldsymbol{T}}\right) \cdot \vec{\boldsymbol{U}}\right] \qquad \text{Equation 8}$$

where the total energy, *E*, and sensible enthalpy, *h*, are respectively given by:

$$\boldsymbol{E} = \boldsymbol{h} - \frac{\boldsymbol{p}}{\boldsymbol{\rho_{ref}}} + \frac{\|\vec{\boldsymbol{U}}\|^2}{2} \qquad \text{Equation 9}$$

$$\boldsymbol{h} = \boldsymbol{C_p} \cdot (\boldsymbol{T} - \boldsymbol{T_{ref}}) \qquad \text{Equation 10}$$

The radiation model adopted in this study corresponds to the Surface-to-Surface (S2S) model, whose main assumption consists in ignoring absorption, emission or scattering of radiation by the medium (ANSYS, 2011a, pp. 176–178). The geometrical function "view factor", F_{12}, defined as the fraction of radiation leaving *surface 1* and directly striking *surface 2* (Çengel, 2003a, p. 606), is calculated in ANSYS Fluent by taking into account the size, separation distance and orientation of surfaces.

2. Materials and methods

2.1. Hardware and software

The machine used in all simulations had two 2.59 GHz Xeon® processors and 32 GB RAM. Software used was ANSYS Fluent, version 15.0 within ANSYS Workbench 2.0 framework, version 15.0.0 (includes ANSYS CFD-Post). Geometries were built in ANSYS DesignModeler and meshes were obtained using ANSYS Meshing. Parallel computing was not adopted, since natural convection patterns were observed to depend on mesh partition (please refer to Annex 5 – Parallel processing). Each simulation was therefore run in series. Computation time for each simulation ranged from about 20 minutes (approx. 400,000 grid elements) to about 17 hours (approx. 1 million grid elements) ([1]).

2.2. Configuration and boundary conditions

Figure 2 represents the current configuration, in which boundaries and domains are identified by numbers 1-10 and letters A-C, respectively.

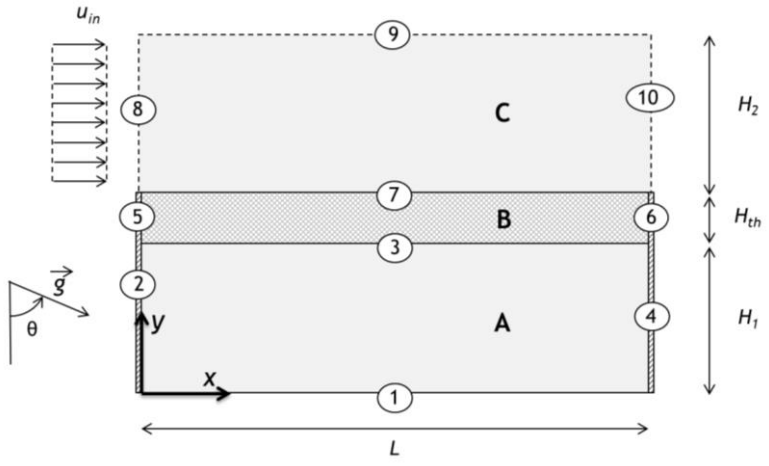

Figure 2 – Configuration under study (drawing does not take scale or aspect ratio into account).

[1] Computation time is not proportional to the size of the computational grid due to the increasing complexity of flow patterns associated with increasing aspect ratio of the enclosure (*AR*).

The configuration comprises two fluid domains (domain A – enclosure, and domain C – external domain), separated by a thin solid domain B (fabric). In the later domain (fabric), pure conduction takes place. The external air flow is perpendicular to boundary 8 (uniform velocity inlet). All boundary conditions are detailed in Table 1.

Table 1 – Boundary conditions.

Boundaries	Fluid Flow Conditions	Heat Transfer Conditions
1	Wall, no-slip condition	Constant temperature T_h = 309.15 K, ε = 0.95
2 , 4	Wall, no-slip condition	Adiabatic, perfect irradiator (ε = 0)
3	Wall, no-slip condition	Coupled [2], $\varepsilon = \varepsilon_{inner\ fabric}$
5 , 6	Wall	Adiabatic
7	Wall, no-slip condition	Coupled [2], ε = 0.77
8	Uniform velocity inlet: velocity u_{in} (normal to boundary)	Inlet temperature T_c = 283.15 K Radiation temperature: T_c = 283.15 K, ε = 1
9	Wall, slip condition	Constant temperature T_c = 283.15 K, ε = 1
10	Pressure outlet: Gauge p = 0 Pa	Backflow temperature: T_c = 283.15 K Radiation temperature: T_c = 283.15 K, ε = 1

It should be noted that the slipping wall condition of boundary 9 allows to keep velocity gradients null at this boundary (symmetry condition regarding momentum), while enabling radiative heat exchange from the fabric's outer surface to ambient. This would not be feasible in Fluent by using a symmetry condition, since the S2S radiation model only considers radiative heat exchange between walls, flow inlets and outlets.

Distance H_2 (i.e. the distance between the slipping wall, boundary 9, and the top of the fabric, boundary 7; Figure 2) was kept at 0.05 m for the current aspect ratio of AR = 4. Validation regarding this aspect is included in Annex 4 – Validation of distance *H2*.

[2] Temperature is continuous across the interface between fluid and solid domains.

2.3. Domain conditions (Cell Zone Conditions)

In what concerns conditions for fluid domains A and C, these were attributed constant fluid properties at the reference temperature, calculated as T_{ref} = (T_h + T_c)/2. These properties are presented in Table 2.

Table 2 – Fluid properties at T_{ref} = 296.15 K.

Property	Units	Value
C_p	J kg^{-1} K^{-1}	1006
k_f	W m^{-1} K^{-1}	0.0260
ρ	kg m^{-3}	1.192
μ	Pa s	1.829x10^{-5}
β	K^{-1}	0.0033767

Regarding the solid domain B, which has a fixed thickness of H_{th} = 1 mm, the fabric material was attributed a thermal conductivity k_s of 0.095240 W m^{-1} K^{-1}, as previously used by Couto & Mayor (2013, 58), except otherwise noted.

2.4. Parametric analysis

Table 3 summarizes simulated conditions for each parametric study. The following parameters were varied: air gap thickness (H_1), air velocity (u_{in}), inclination of the enclosure (θ) and thermal resistance of the fabric (R_{CT} = H_{th}/k_s). For each study, two extreme values of emissivity of the inner fabric were tested ($\varepsilon_{inner\ fabric}$ = = 0.05 and 0.95, as well as two inclinations of the enclosure (θ = 0º and 90º). Each set of conditions was labelled according to Annex 2 – *Labelling of simulation cases*.

Table 3 – Parameter values for each parametric study. All combinations for each study were simulated. Ranges of parameters are given as "*first*:*increment*:*last*".

Parameter	**Air Gap Thickness,** inclination and emissivity	**Air Velocity,** inclination and emissivity	**Inclination** and emissivity	**Fabric's Thermal Resistance,** inclination and emissivity
Air gap thickness, H_1 [m]	{0.008, 0.025, 0.052}	0.052	0.052	0.052
Skin temperature, T_h [K]	309.15	309.15	309.15	309.15
Inlet air temperature, T_c [K]	283.15	283.15	283.15	283.15
Inlet air velocity, u_{in} [m s^{-1}]	0.5	{0.5, 3.0}	0.5	0.5
Inclination, θ [°]	{0, 90}	{0, 90}	{-120, -90:10:-20, -10:1:-5, 0, 5:1:10, 20:10:90, 120, 180}	{0, 90}
Thermal conductivity of the fabric, k_s [W m^{-1} K^{-1}]	9.524×10^{-2}	9.524×10^{-2}	9.524×10^{-2}	{9.524×10^{-2}, 9.524×10^{-3}}
Thermal resistance of the fabric, R_{CT} [K m^2 W^{-1}]	0.0105	0.0105	0.0105	{0.0105, 0.1050}
Emissivity, $\varepsilon_{inner\ fabric}$ [-]	{0.05, 0.95}	{0.05, 0.95}	{0.05, 0.95}	{0.05, 0.95}

2.5. Meshing

Structured, quadrilateral meshes were obtained for the above configuration. In order to locally increase the density of meshes in critical zones (e.g. near inlets and where gradients are expected to be greater), the "Bias" option was activated. This means that the edge length of elements increases in a chosen direction and, by defining a bias factor *B*, the larger elemental edge will be *B* times larger than the smallest elemental edge in a given direction (ANSYS, 2013a, p. 184). For further details regarding meshing parameters, please refer to Annex 1 – Meshing parameters.

In order to insure that present results are grid-independent, grid tests were performed by comparing results from increasingly denser meshes (please refer to Annex 8 - Grid sensitivity tests). Thus, mesh 3 ([3]) was selected for the parametric analysis presented in this study.

[3] I.e. the third of four tested meshes, each with a 4-fold increase in number of grid elements.

2.6. Solution methods

The pressure-based solver was used in every simulation, since this is normally preferred for incompressible or mildly compressible fluid flows (ANSYS, 2013b, p. 1405). Gravitational acceleration ($|\vec{g}| = 9.81\ m\ s^{-2}$) was enabled in the general solution setup and its components were changed as a function of the inclination of the enclosure (θ), as given by:

$$\vec{g} = (|\vec{g}| \sin(\theta) , -|\vec{g}| \cos(\theta)) \qquad \text{Equation 11}$$

The pressure-velocity coupling scheme was set to "Coupled", which is a full pressure-velocity coupling method (in contrast with SIMPLE, which is a pressure-based segregated algorithm; ANSYS 2013, 1415). The "Coupled" scheme is regarded as more robust and efficient for single-phase steady-state problems (ANSYS, 2013b, p. 1416). Since considerable body forces are expected to arise from buoyancy effects (natural convection), the pressure interpolation scheme was set to "Body Force Weighted" (ANSYS, 2013b, p. 1410). All other schemes were kept as default (second-order schemes for momentum and energy). Under-relaxation factors were retained as default, except when convergence could not be achieved. Such cases are summarized in Table 4 (labels according to Annex 2 – Labelling of simulation cases), along with the description of the convergence issue and the respective measure taken in order to attain convergence.

2.7. Solution initialization

Natural convection problems are sensitive to initial conditions provided to the solver (Couto & Mayor, 2013; Hart, 2006; Khezzar et al., 2012; Soong & Tzeng, 1996). Differently from previous studies, which use solutions for higher/lower inclinations as initial guesses for subsequent inclinations (Khezzar et al., 2012; Soong & Tzeng, 1996; H. Wang & Hamed, 2006), in the present study this method was not adopted, since it was not aimed to address the hysteresis effect. Initial conditions were there-

fore maintained constant for all simulations, by selecting the "Standard Initialization" option, and conditions were set to: gauge pressure $p = 0$ Pa; velocity components $u = v = 0.001$ m s^{-1}; temperature $T = T_{ref} = 296.15$ K.

Table 4 – Convergence issues and respective measures taken in order to improve convergence.

Simulation Cases	Convergence issue	Measure to improve convergence
AR_4_Teta_40_epsilon_05 (mesh 3) AR_4_Teta_50_epsilon_95 (mesh 3) AR_4_Teta_90_H1_0008_epsilon_95 (mesh 3)	Solver diverged (it did not reach the maximum number of iterations)	Flow Courant Number (FCN) was initially lowered from 200 to 100; towards convergence, FCN was reset to the default value (200) and the final solution was obtained.
AR_4_Teta_0_U_3_epsilon_05 (mesh 4) AR_4_Teta_90_U_3_epsilon_05 (mesh 4)	Oscillating residuals (maximum number of iterations was reached)	
AR_4_Teta_-80_epsilon_05 (mesh 3) AR_4_Teta_-50_epsilon_05 (mesh 3) AR_4_Teta_-30_epsilon_05 (mesh 3) AR_4_Teta_180_epsilon_05 (mesh 3) AR_4_Teta_180_epsilon_95 (mesh 3) AR_4_Teta_90_U_3_epsilon_05 (mesh 1 - 4)		Energy under-relaxation factor was lowered from 1 to 0.9 and maintained throughout the entire computation.

2.8. Convergence criteria

Residuals (for continuity, velocity and energy) were used in this study as criteria for convergence. Unless otherwise noted, the maximum value for continuity and velocity residuals was set to 10^{-6}, with a lower value of 10^{-9} for energy residuals. The maximum number of iterations (in case convergence is not achieved according to the above criteria) was set to 20,000.

For the calculation of radiative heat exchange, the maximum value for radiosity residuals was set to 10^{-6}, the maximum number of iterations to 100 and the number of energy iterations per radiation iteration was set to 1.

2.9. Calculation of the view factor

View factor calculation was performed using the "Ray tracing" method ("Face to Face" option was selected). "Resolution" was set to 1000, which, in 2D, corresponds to 500 computed rays ("Resolution" divided by 2) at each elemental face or

Surface Cluster (ANSYS, 2011b, p. 1795). In order to reduce view factor computation time, Fluent enables the clustering of elemental faces in so-called Surface Clusters. The number of faces per Surface Cluster (FPSC) has a default value of 1 (i.e., no clustering), which can be increased by the user in order to reduce both memory requirement and size of the resulting file containing view factor data for S2S (ANSYS, 2011b, p. 759). In this study, no clustering was performed (FPSC = 1), which usually yields more accurate results (ANSYS, 2011b, p. 759).

All boundaries were included in the calculation of the view factor, except for boundaries 5 and 6, which correspond to adiabatic walls in direct contact with the solid domain B (these do not exchange radiative heat).

3. Results and discussion

In this section, results are presented and analysed regarding the effects of air gap thickness, external air velocity, inclination and thermal conductivity of the fabric. Validation of computational methods is included in the Annexes (please refer to Annex 9 – Validation of computational methods); validation was performed prior to the current parametric analysis, by comparing results to those of previous works (Corcione, 2003; Couto & Mayor, 2013; Davis, 1983; Vivek et al., 2012).

3.1. Effects of Air Gap Thickness

Air gap thickness, H_1, was varied in the range 8 to 52 mm. *Ra* thus varied between 9.0×10^2 and 2.8×10^5 (Table 5). These values are below 3×10^5, the critical *Ra* usually accepted as the upper limit for steady solutions, both for vertical (Christon et al., 2002) and horizontal enclosures (Çengel, 2003c, p. 478). Obtained average *Nu* values on the skin ([4]) are presented in Table 5. Temperature and velocity contours are displayed in Figure 3. Heat flux profiles along the skin and the top of the fabric are presented in Figure 4, while corresponding profiles for local temperature and

Table 5 – Average *Nu* values on the skin (boundary 1, Figure 2) as a function of air gap thickness, enclosure's inclination and emissivity of inner fabric.

θ [°]	$\varepsilon_{inner\ fabric}$ [-]	H_1 = 8 mm				H_1 = 25 mm				H_1 = 52 mm			
		Nu_{conv} [-]	Nu_{rad} [-]	Nu_{total} [-]	*Ra* [-]	Nu_{conv} [-]	Nu_{rad} [-]	Nu_{total} [-]	*Ra [-]*	Nu_{conv} [-]	Nu_{rad} [-]	Nu_{total} [-]	*Ra* [-]
0	**0.05**	1.000	0.092	1.092	1.11E+03	3.511	0.290	3.801	3.06E+04	6.040	0.603	6.644	2.72E+05
	0.95	1.002	1.533	2.535	9.09E+02	3.236	4.837	8.073	2.40E+04	5.498	10.095	15.593	2.03E+05
90	**0.05**	1.104	0.092	1.196	1.09E+03	2.913	0.289	3.202	3.15E+04	5.029	0.602	5.631	2.80E+05
	0.95	1.048	1.535	2.583	8.99E+02	2.654	4.836	7.490	2.44E+04	4.529	10.107	14.635	2.05E+05

[4] Please refer to *Annex 6 – Mathematical formulae*.

convective heat flux coefficient h_{conv} ([4]) along the top of the fabric are displayed in Figure 5. Finally, average heat fluxes on skin are compared in Figure 6.

From velocity contours of Figure 3 (right column), one observes that velocity magnitudes in the enclosure are practically null for θ = 0º and H_1 = 8 mm (Figure 3g and Figure 3j), meaning that no natural convection is detected. The corresponding isotherms are almost parallel (Figure 3a and Figure 3d) and heat flux profiles along the skin and the top of the fabric are less wavy than those for higher values of H_1 (Figure 4a and Figure 4b, black lines), except for the top of fabric at low x-coordinates (the sharp variation is due to the development of the external thermal

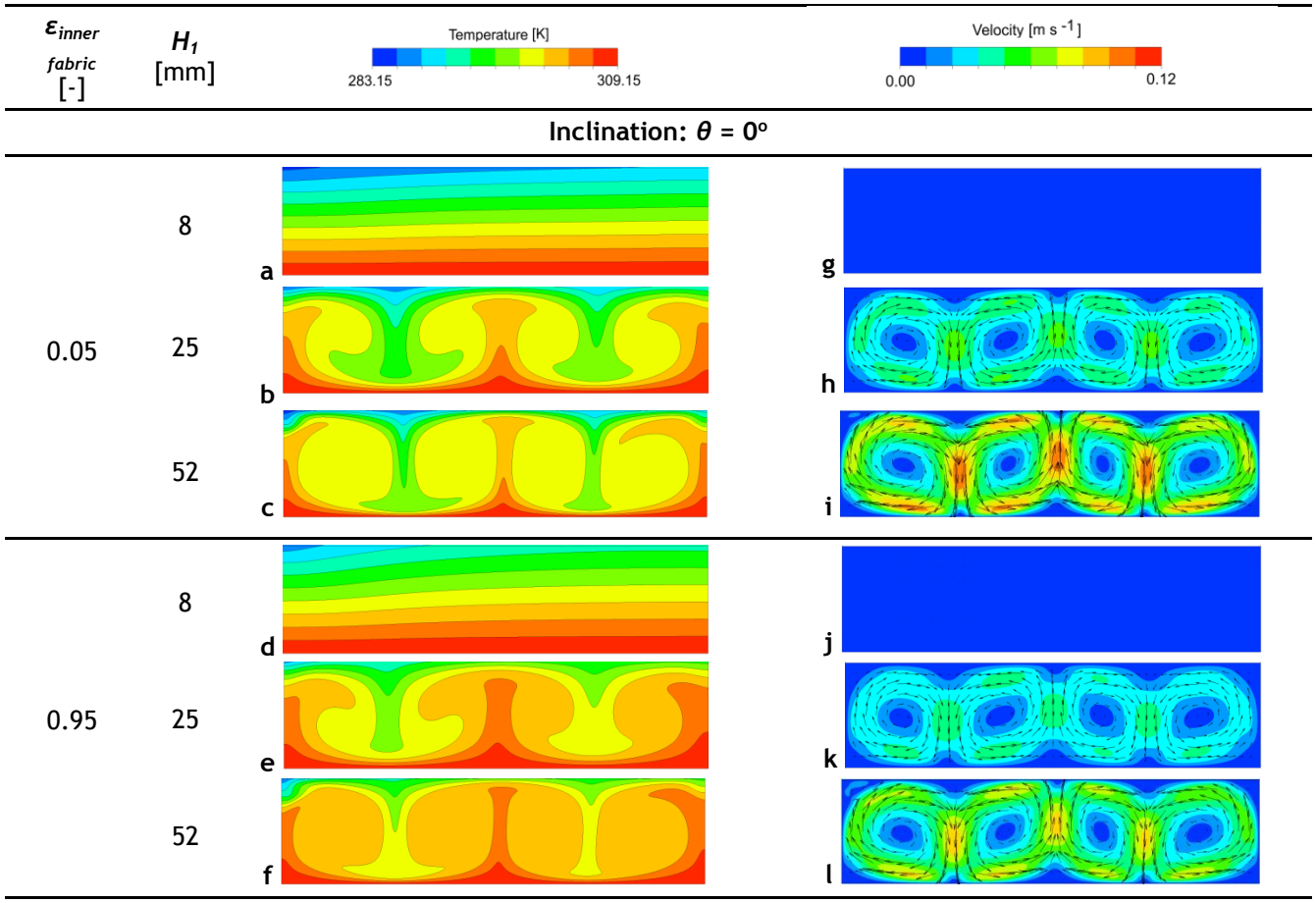

Figure 3 – Temperature and velocity contours in the air gap (domain A, Figure 1a) for several air gap thicknesses (8, 25 and 52 mm), inclinations of the enclosure (0º and 90º) and values of inner fabric emissivity (0.05 and 0.95). For sake of graphical simplicity, different length scales were used (*AR* is constant).
[continued on the next page]

boundary layer). The resulting average Nu_{conv} values are practically equal to 1 (Table 5, H_1 = 8 mm and θ = 0º), confirming the occurrence of pure conduction. These results are justified by *Ra* values (Table 5) well below 1708, the accepted upper limit for pure conduction in horizontal enclosures (Çengel, 2003c, p. 478). However, it is observed that such limit does not apply for vertical enclosures, since convection takes place for θ = 90º and H_1 = 8 mm, though corresponding to *Ra* < 1708 (Table 5): from θ = 0º to 90º, velocities in the enclosure increase, forming single clockwise-rotating roll cells (Figure 3s and Figure 3v), isotherms become slightly wavy (Figure 3m and Figure 3p) and, as a result, local heat fluxes vary significantly along the skin and the fabric (Figure 4c and Figure 4d, black lines). Finally, the resulting average Nu_{conv} is up to around 10% higher than the unit (Table 5, H_1 = 8 mm and θ = 90º), evincing natural convection.

$\varepsilon_{inner\ fabric}$ [-]	H_1 [mm]	Temperature [K] 283.15 – 309.15	Velocity [m s^{-1}] 0.00 – 0.12
		Inclination: θ = 90º	
0.05	8	m	s
	25	n	t
	52	o	u
0.95	8	p	v
	25	q	w
	52	r	x

Figure 3 - [continued].

As H_1 is increased from 8 to 25 to 52 mm, one notices a general increase in velocity magnitudes throughout the enclosure (Figure 3, right column). For θ = 0º, there is also an increase in the number of roll cells from 0 cells, at H_1 = 8 mm, to 4 cells, at H_1 = 25 mm. All these changes are due to the fact that *Ra* escalates with increasing H_1 (Table 5), meaning increased buoyancy forces, which drive natural convection. In agreement with this, there is a general increase in Nu_{conv} values with increasing H_1 (Table 5).

Unexpectedly, for θ = 0º and H_1 = 25 mm (Figure 3h and Figure 3k), the number of roll cells differs from that previously obtained by Couto & Mayor (2013): the referred authors obtained 2 instead of 4 roll cells (present study). Consequently, Nu_{conv} values differ up to 16% from the mentioned study. It can be hypothesized that both flow modes (with 2 and 4 cells) might be real, adding that numerical results for natural convection are strongly tied to initial conditions given to the solver. Also, these results may be dependent on the numerical method, since the mentioned study was based on a different commercial CFD code. In addition, similar changes in number of roll cells had already been observed for both *AR* = 4 and *AR* = 12 during the study of parallel computing (Annex 5 – Parallel processing, regarding results' dependency on partitioning of the mesh). These results suggest the existence of multiple steady-states, even when initial conditions are maintained.

Local heat flux profiles of Figure 4 show almost opposite variations for the skin and the top of the fabric, whenever natural convection occurs (i.e. all cases except for θ = 0º with H_1 = 8 mm). Thus, *x*-coordinates corresponding to local maxima on one of the surfaces almost exactly match *x*-coordinates for local minima on the opposing wall. This behaviour is typical of natural convection and it is explained by flow and temperature maps observed in Figure 3, in which local temperature gradients near each wall vary along *x*: local heat flux maxima correspond to spots where cold air (or warm air) moves towards the skin (or fabric), creating higher temperature gradients, while local minima correspond to the inverse situation (air moving away from the wall and correspondingly lower temperature gradients). This is similar to what had been previously reported (Couto & Mayor, 2013).

The effect of H_1 on the temperature of the fabric (Figure 5a and Figure 5b) corresponds to a temperature rise as H_1 is increased. Additionally, the higher the air gap thickness, the higher the resulting waviness of temperature along the fabric. These variations along the fabric are significant and suggest possibly large errors when taking the fabric as an isothermal surface for estimating local heat fluxes in clothing applications. However, such variations along x are not as significant in the centre of the vertical enclosure (for θ = 90º, maximum variation corresponds to 2.3 degrees for x/L = [0.2, 0.8]; Figure 5a and Figure 5b, dashed lines) as compared to cases of horizontal enclosures (for θ = 0º, maximum variation corresponds to 5.1 degrees for and x/L = [0.2, 0.8], Figure 5a and Figure 5b, solid lines).

Regarding h_{conv} curves (Figure 5c and Figure 5d), the apparent decrease in h_{conv} with increasing H_1 is solely due to the fact that x-coordinates are made dimensionless by dividing x by L (where L increases with H_1, for constant aspect ratio). Differently from h_{conv} curves for isothermal surfaces, which correspond to a monotonic decrease along x due to the development of the thermal boundary layer (Lienhard IV & Lienhard V 2003, 304), present h_{conv} curves for the horizontal enclosure (Figure 5c and Figure 5d, solid lines) show non-monotonic behaviour for cases in which internal natural convection occurs ($H_1 \geq 25$ mm). Considering that $h_{conv} = q_{conv}/(T - T_c)$ (Equation A.1, Annex 6 – Mathematical formulae), the fact that h_{conv} does not decrease monotonically means that the local convective heat flux, q_{conv}, is locally higher (or lower) than would be expected based on the temperature difference between the fabric (T) and the inlet air (T_c). It follows that the impact of internal flow patterns on local heat fluxes through the fabric is due not only to changes in the temperature along the fabric, but also to changes in the local heat transfer coefficient h_{conv}, due to the waviness of the thermal boundary layer forming along the fabric's external surface (please refer to section 3.3 for further details). For vertical enclosures (θ = 90º, Figure 5c and Figure 5d, dashed lines), h_{conv} profiles exhibit no oscillations along

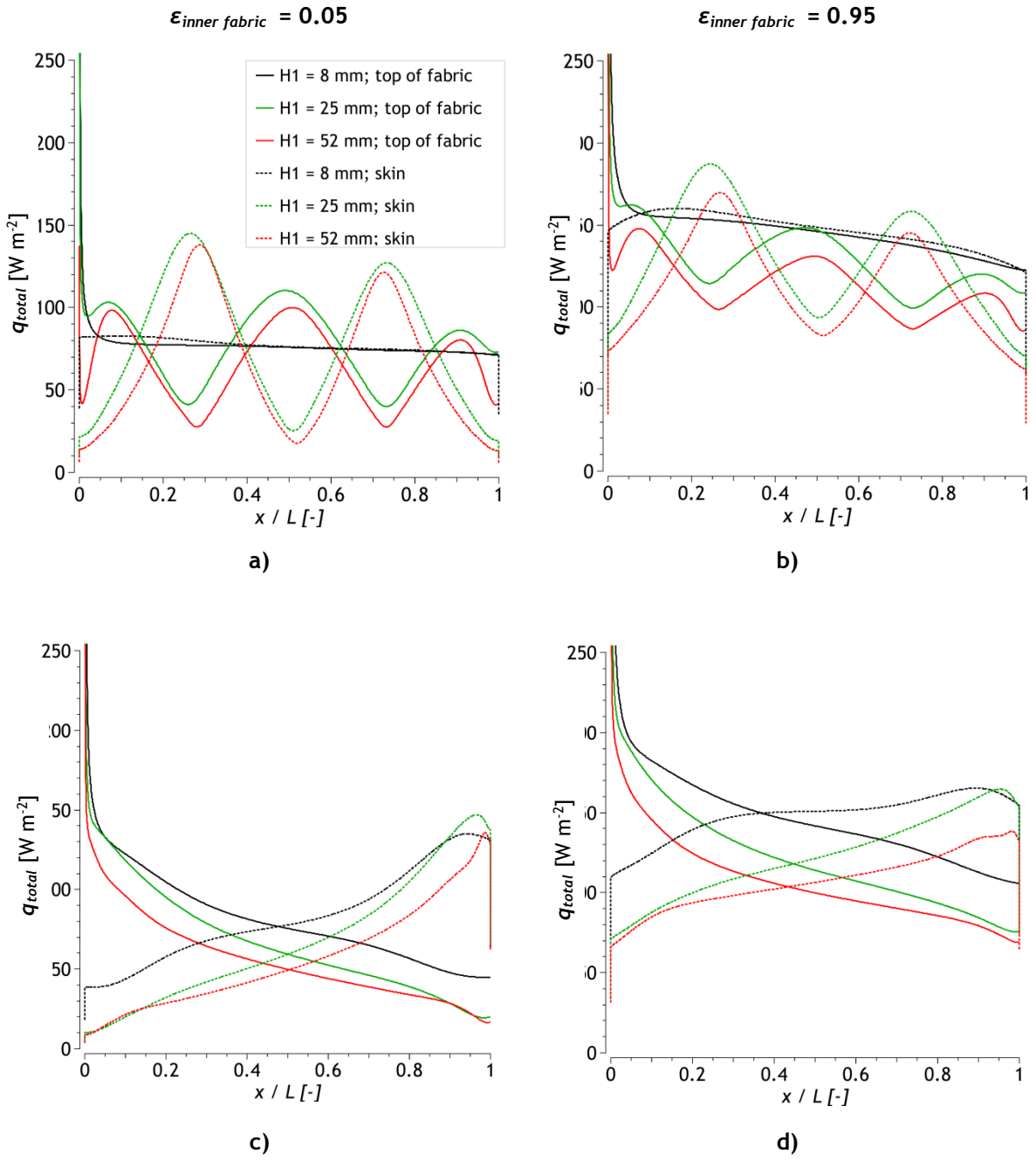

Figure 4 - Comparison of heat flux profiles (q_{total}) along the top of the fabric (boundary 7, Figure 2) and along the skin (boundary 1, Figure 2) for several values of microclimate thickness H_1 (8, 25 and 52 mm) and two values of emissivity: a,c) $\varepsilon_{inner\ fabric}$ = 0.05; b,d) $\varepsilon_{inner\ fabric}$ = 0.95. Two inclinations of the enclosure are considered: a,b) θ = 0º; c,d) θ = 90º.

the *x*-direction, which is consistent with the internal flow patterns presented in Figure 3, since these consist of single roll cells for θ = 90º (Figure 3s-x). Thus, in the absence of multiple roll cells, the shape of temperature and h_{conv} profiles for θ = 90º

(Figure 5, dashed lines) more closely resembles the monotonic behaviour typical of pure conduction (e.g. H_1 = 8 mm at θ = 0º, Figure 5, solid black lines).

The relative importance of convection and radiation can be evaluated by comparing average heat fluxes observed at the skin level (Figure 6). For $\varepsilon_{inner\ fabric}$ = 0.05 (Figure 6, bars with stripes), convection/conduction are the dominant phenomena. This is observed also in Table 5, where Nu_{conv} is always higher than Nu_{rad} for $\varepsilon_{inner\ fabric}$ = 0.05. Conversely, for $\varepsilon_{inner\ fabric}$ = 0.95, radiation becomes dominant over convection: radiation accounts for more than 50% of the total heat losses (Figure 6, filled bars), while Nu_{rad} is around 50% to 100% higher than Nu_{conv} (Table 5). Additionally, as in Couto & Mayor (2013), an increase in radiative heat transfer (through increasing $\varepsilon_{inner\ fabric}$) is accompanied by a decrease in the intensity of convection. This is shown in Figure 6, where average convective heat fluxes decrease for higher $\varepsilon_{inner\ fabric}$. Such effect is due to the existence of lower temperature gradients near the skin for higher emissivity values, as seen in temperature contours of Figure 3: by comparing contours for the same θ and H_1 (e.g., contour *f* compared to contour *c*), thermal boundary layers in the vicinity of the skin are thicker at higher emissivity of the inner fabric. Also, fabric's temperature is higher for $\varepsilon_{inner\ fabric}$ = 0.95 (Figure 5b) when compared to $\varepsilon_{inner\ fabric}$ = 0.05 (Figure 5a), meaning lower temperature differences between skin and fabric and, consequently, lower *Ra* values (Table 5) and lower buoyancy forces.

It is further noticed that, contrary to *Nu* values of Table 5, which always increase with increasing H_1 (meaning increased efficiency of convection/radiation relative to hypothetical pure conduction), average heat fluxes on the skin are almost always decreasing with increasing H_1 (Figure 6). Possible explanations for this fact are next presented, regarding radiation and convection separately.

The decrease in radiative heat flux with increasing H_1 can be explained by the rise in temperature of the fabric with increasing H_1 (Figure 5a and Figure 5b) and the fact that radiative heat exchange decreases with decreasing temperature differences between the two exchanging walls (i.e., the isothermal skin and the inner surface of the fabric).

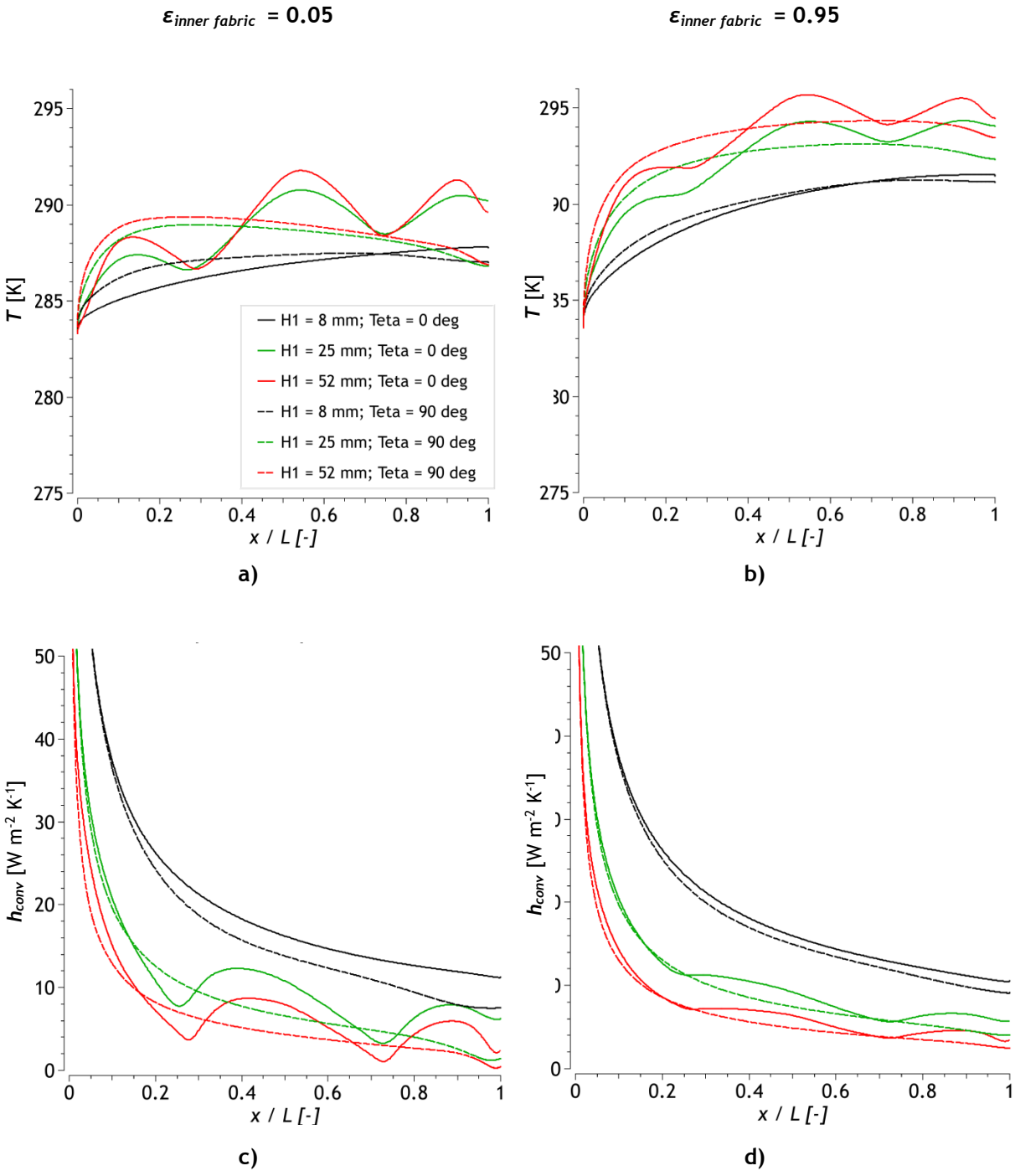

Figure 5 - Comparison of temperature (*T*) and local convective heat transfer coefficient profiles (h_{conv}) along the top of the fabric (boundary 7, Figure 2) for several values of microclimate thicknesses H_1 (8, 25 and 52 mm) and two values of emissivity: a,c) $\varepsilon_{inner\ fabric}$ = 0.05; b,d) $\varepsilon_{inner\ fabric}$ = 0.95. Two inclinations of the enclosure are considered (θ = 0º and 90º).

Similarly, decreases in convective heat fluxes with increasing H_1 are almost always observed (Figure 6), this being also due to the decreasing temperature differences between the skin and the fabric and the consequent decrease in buoyancy forces. However, there is one noteworthy exception for θ = 0º at low inner fabric emissivity (Figure 6a, bars with stripes): as H_1 is increased from 8 to 25 mm, heat flux is practically constant, this being due to the transition from pure conduction to convection inside the enclosure. In fact, the occurrence of convection at H_1 = 25 mm compensates for the insulating effect of increasing H_1 from 8 to 25 mm. Still, for the corresponding cases of higher inner fabric emissivity (Figure 6a, filled bars), heat fluxes are not constant (there is a decrease of around -10%, as H_1 is changed from 8 to 25 mm), even though the same transition occurs from pure conduction at H_1 = 8 mm to convection at H_1 = 25 mm. This is due to the fact that, by increasing $\varepsilon_{inner\ fabric}$ from 0.05 to 0.95, increased radiation leads to a lower efficiency of convection (i.e. for $H_1 \geq 25$ mm), as explained before in this section, underlining once again the importance of considering radiation together with convection/conduction in analysing the current configuration. Additionally, it should be noted that, as H_1 is increased more than 5-fold (from 8 to 52 mm), convective heat fluxes decrease only around 17 to 45%. This evinces the increasing importance of internal natural convection as the air gap thickness is increased.

Finally, comparison of average heat fluxes on the skin from horizontal (Figure 6a) to vertical enclosures (Figure 6b), enables to conclude that, for $H_1 \geq 25$ mm, convective heat fluxes decrease around 14 to 17%. This is due to the fact that single-cell convection (Figure 3t-u and Figure 3w-x) is less effective than multi-cell convection (Figure 3h-i and Figure 3k-l) in transferring heat, as will be further detailed in sub-section 3.3. Differently, for H_1 = 8 mm, increases of merely 3-8% are observed in average heat fluxes, these being due to the transition from pure conduction at θ = 0º to convection at θ = 90º. Thus, significant differences (i.e. differences superior to 10%) in average convective heat fluxes from the horizontal to the vertical enclosure are only observed for $H_1 \geq 25$ mm. Regarding radiation, average radiative heat fluxes are observed to be practically constant between horizontal and vertical enclosures (variations within 3%).

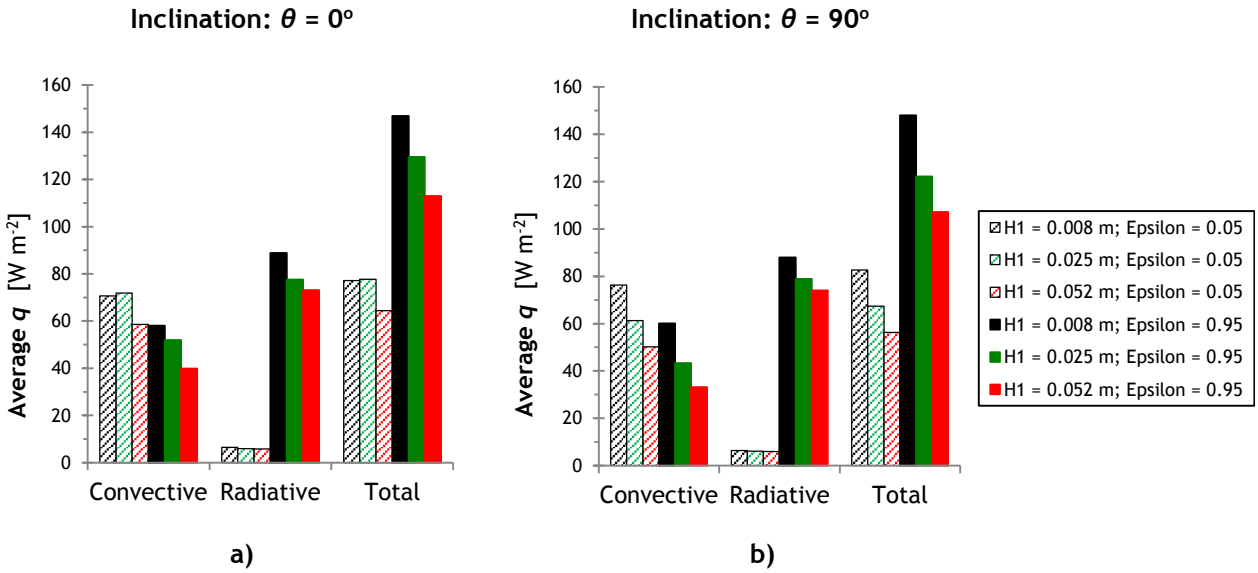

Figure 6 - Comparison of average convective, radiative and total heat fluxes on the skin (boundary 1, Figure 2) for several values of air gap thickness (H_1), emissivity of the inner fabric ("Epsilon") and two inclinations of the enclosure: a) θ = 0º; b) θ = 90º. Since the skin is at a higher temperature than the surroundings, heat fluxes correspond to heat losses from the skin to the environment.

3.2. Effects of Air Velocity

Inlet air velocity was increased from 0.5 to 3.0 m s^{-1}, velocities that encompass the range of speed for a walking human and therefore are relevant in many clothing applications. *Ra* thus varied between 2.0×10^5 and 3.1×10^5 (Table 6). The maximum *Ra* lays around the critical value of 3×10^5, above which the internal flow becomes time-dependent (Çengel, 2003c, p. 478; Christon et al., 2002). This may explain why convergence issues were experienced in such cases of u_{in} = 3.0 m s^{-1} (Table 4 of section 2. *Materials and methods*). Nevertheless, steady-state solutions could be obtained for such cases by lowering the energy under-relaxation factor, as noted above in the *Materials and methods*, section 2.6.

Obtained average *Nu* values on the skin ([5]) are presented in Table 6. Temperature and velocity contours are displayed in Figure 7. Heat flux profiles along the skin and the top of the fabric are presented in Figure 8, while corresponding profiles for local temperature and convective heat flux coefficient h_{conv} ([6]) profiles along the

[5] Please refer to *Annex 6 - Mathematical formulae*.
[6] Please refer to *Annex 6 - Mathematical formulae*.

top of the fabric are presented in Figure 9. Finally, average heat fluxes on the skin are compared in Figure 10.

Table 6 - Average *Nu* on the skin (boundary 1, Figure 2) as a function of inlet air velocity, enclosure's inclination and emissivity of inner fabric.

θ [°]	$\varepsilon_{inner\ fabric}$	u_{in} = 0.5 m s^{-1}				u_{in} = 3.0 m s^{-1}			
	[-]	Nu_{conv} [-]	Nu_{rad} [-]	Nu_{total} [-]	Ra [-]	Nu_{conv} [-]	Nu_{rad} [-]	Nu_{total} [-]	Ra [-]
0	**0.05**	6.040	0.603	6.644	2.72E+05	6.214	0.597	6.812	3.02E+05
	0.95	5.498	10.095	15.593	2.03E+05	5.845	9.968	15.813	2.47E+05
90	**0.05**	5.029	0.602	5.631	2.80E+05	5.130	0.596	5.726	3.09E+05
	0.95	4.529	10.107	14.635	2.05E+05	4.789	9.963	14.752	2.51E+05

An increase in u_{in} from 0.5 to 3.0 m s^{-1} is seen to produce a general increase in velocity magnitudes in the enclosure: from Figure 7 (right column), velocities are observed to increase from *i* to *j*, *k* to *l*, *m* to *n* and *o* to *p*. These changes are associated with higher temperature gradients near the skin for u_{in} = 3.0 m s^{-1}, as seen in temperature contours of Figure 7 (left column): by comparing contours for the same θ and $\varepsilon_{inner\ fabric}$ (e.g., contour *b* compared to contour *a*), thermal boundary layers on the skin are observed to be thinner for the higher external velocity. Additionally, temperature differences between skin and fabric are also higher for u_{in} = 3.0 m s^{-1}, since temperatures along the fabric are lower in such cases (Figure 9a and Figure 9b). Consequently, increased *Ra* values are observed for the higher u_{in} of 3.0 m s^{-1} (Table 6) and increased buoyancy forces result in higher Nu_{conv} values for the higher u_{in} (Table 6, increases of around 2-6% in Nu_{conv}).

By increasing u_{in}, the rise in intensity of internal natural convection is also associated with increased local heat fluxes (Figure 8). Additionally, these heat fluxes have increased amplitude of oscillation along skin and top of the fabric (idem). Interestingly, for low emissivity ($\varepsilon_{inner\ fabric}$ = 0.05), changes are more significant around local maxima (Figure 8a and Figure 8c), while, for $\varepsilon_{inner\ fabric}$ = 0.95, both maxima and minima are increased (Figure 8b and Figure 8d). This is due to a

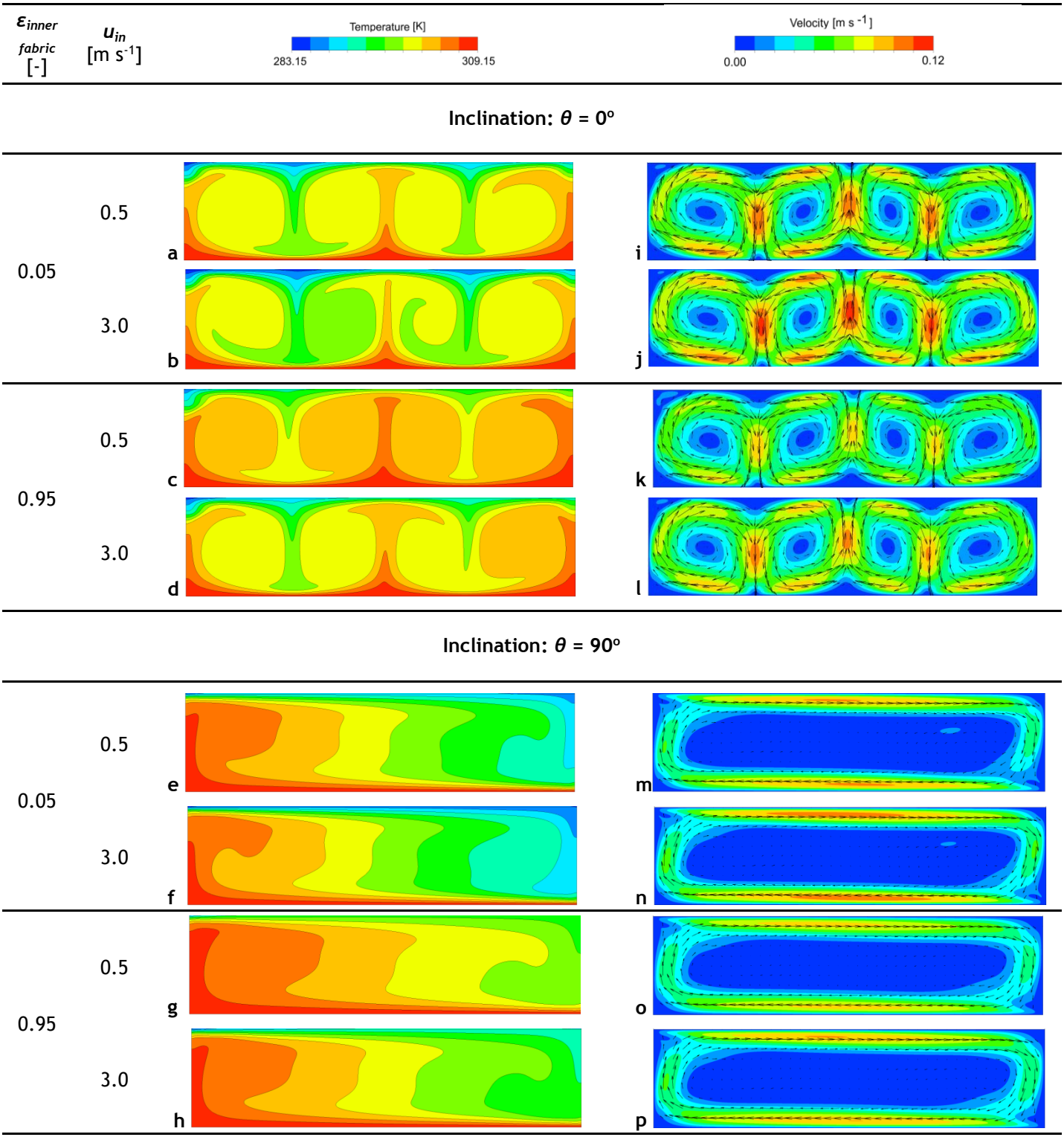

Figure 7 - Temperature and velocity contours in the air gap (domain A, Figure 1a) for two inlet velocities (0.5 and 3.0 m s^{-1}), two inclinations of the enclosure (0º and 90º) and two values of inner fabric emissivity (0.05 and 0.95).

higher relative importance of radiation for $\varepsilon_{inner\ fabric}$ = 0.95: while effects of u_{in} on radiative heat transfer are widespread across the entire span of x-coordinates (due to the fact that radiative heat fluxes are only directly dependent on surface temperatures and view factor), effects on convective heat transfer are more localized (convective heat fluxes are more significant in regions of higher temperature gradients near each surface); this explains why q_{total} curves of Figure 8b and Figure 8d ($\varepsilon_{inner\ fabric}$ = 0.95) show an increase with rising u_{in} that is relatively constant along x, compared to localized increases in curves of Figure 8a and Figure 8c ($\varepsilon_{inner\ fabric}$ = 0.05).

Temperature and h_{conv} profiles on the fabric are presented in Figure 9. It is possible to observe that temperature along the fabric becomes slightly less wavy as u_{in} is increased (Figure 9a and Figure 9b), whereas the opposite is observed for h_{conv} profiles (Figure 9c and Figure 9d). In fact, though the top of the fabric gets closer to the situation of an isothermal wall for increased u_{in}, h_{conv} on the fabric becomes wavier. This is due to local fluxes, which oscillate with increased amplitude as u_{in} increases (as noted above, regarding Figure 8). Thus, for increasing u_{in}, the assumption of an isothermal fabric would lead to increasing errors in estimating local heat fluxes along the fabric. Additionally, differences in h_{conv} profiles between $\theta = 0^o$ and $\theta = 90^o$ (non-monotonic and practically monotonic curves, respectively) become more significant as u_{in} is increased (Figure 9c and Figure 9d).

Regarding radiative heat transfer, Nu_{rad} is practically constant relative to u_{in}, with variations around 1%, whereas average Nu_{conv} values on the skin increase around 2-6% (Table 6). Thus, the efficiency of radiative heat exchange relative to conduction is not significantly altered by external air velocity, at least in the range u_{in} = 0.5 to 3.0 m s^{-1}. However, there is a general increase in average radiative heat fluxes q_{rad} with increasing u_{in}, as seen in Figure 10. Together, these facts indicate that increases in q_{rad} are counteracted by similar increases in the temperature difference, ΔT, according to the definition of *Nusselt* number ($Nu_{rad} = q_{rad} \cdot H_1/(k \cdot \Delta T)$; please refer also to *Annex 6 – Mathematical formulae*).

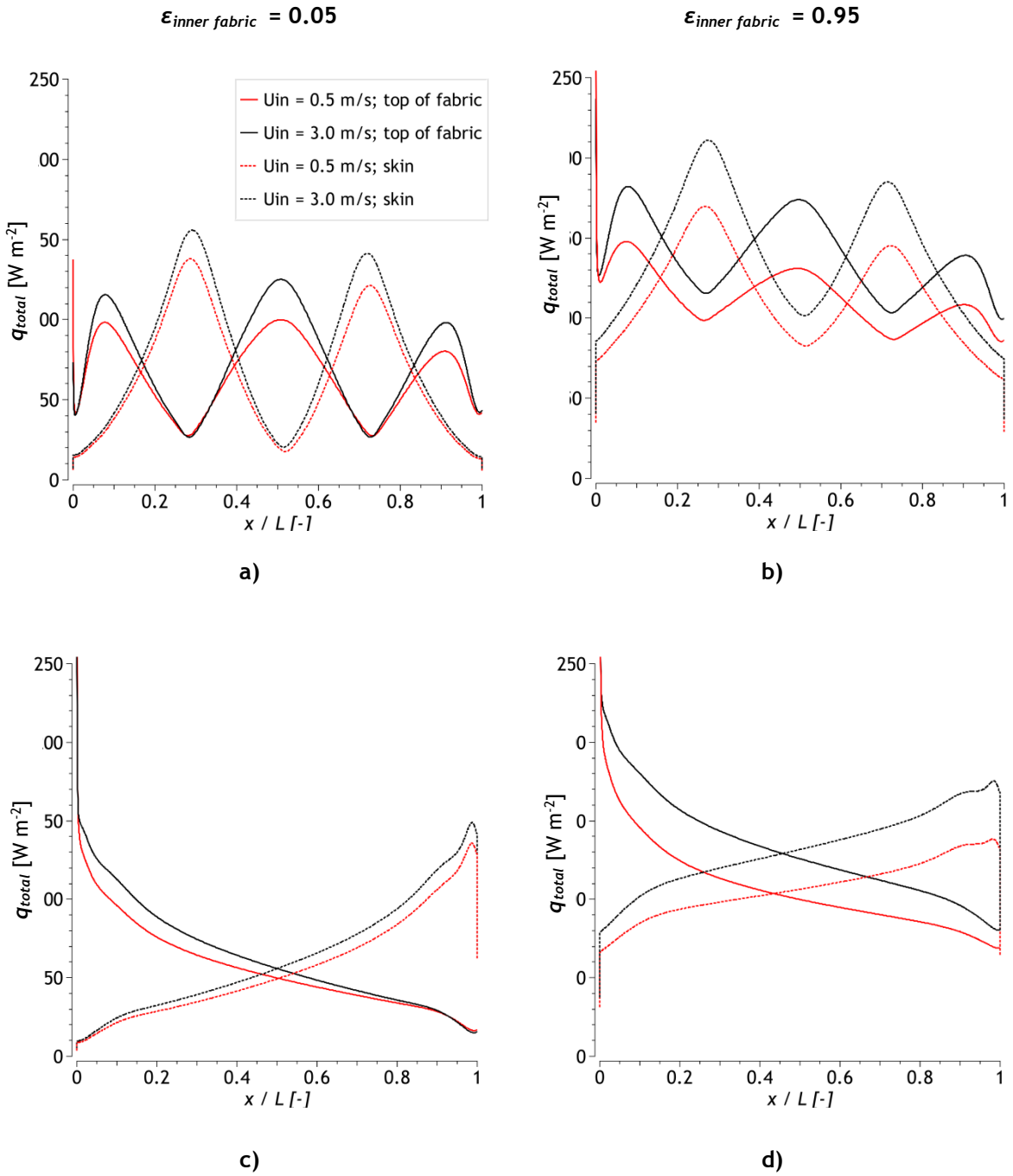

Figure 8 - Comparison of heat flux (q_{total}) profiles along the top of the fabric (boundary 7, Figure 2) and along the skin (boundary 1, Figure 2) for two values of inlet air velocity u_{in} (0.5 and 3.0 m s^{-1}), two inclinations of the enclosure, corresponding to a,b) θ = 0º and c,d) θ = 90º, and two values of emissivity, corresponding to a,c) $\varepsilon_{inner\ fabric}$ = 0.05 and b,d) $\varepsilon_{inner\ fabric}$ = 0.95.

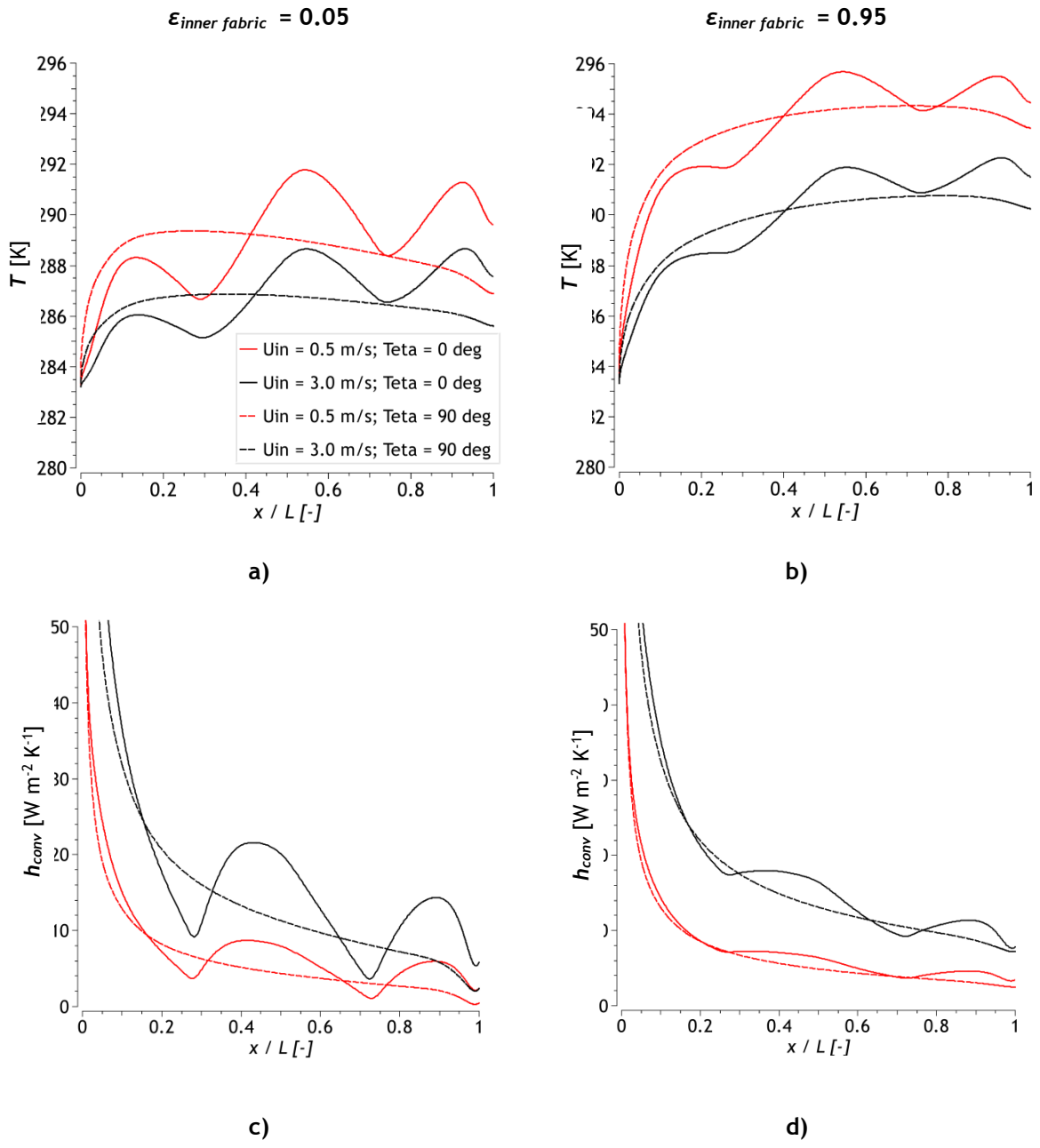

Figure 9 - Comparison of temperature (*T*) and local convective heat transfer coefficient profiles (h_{conv}) along the top of the fabric (boundary 7, Figure 2) for two values of inlet air velocity u_{in} (0.5 and 3.0 m s^{-1}) and two values of emissivity: a,c) $\varepsilon_{inner\ fabric}$ = 0.05; b,d) $\varepsilon_{inner\ fabric}$ = 0.95. Two inclinations of the enclosure are considered (θ = 0º and 90º).

Total average heat fluxes at the skin (Figure 10) are observed to increase as u_{in} is changed from 0.5 to 3.0 m s^{-1} (increases of 12-23%). Such increases are more significant for high $\varepsilon_{inner\ fabric}$ (increases of around 23%) compared to low $\varepsilon_{inner\ fabric}$

(increases of 12-14%). It is therefore of importance to consider radiative heat exchange between skin and fabric, since it can significantly amplify the effect of u_{in} on total heat transfer. For instance, if radiative heat exchange would be disregarded (e.g. by setting emissivity as null), the effect of u_{in} on total transferred heat would be underestimated in up to approx. 50% (i.e. by comparing the 12% increase for low emissivity to the 23% increase for high emissivity).

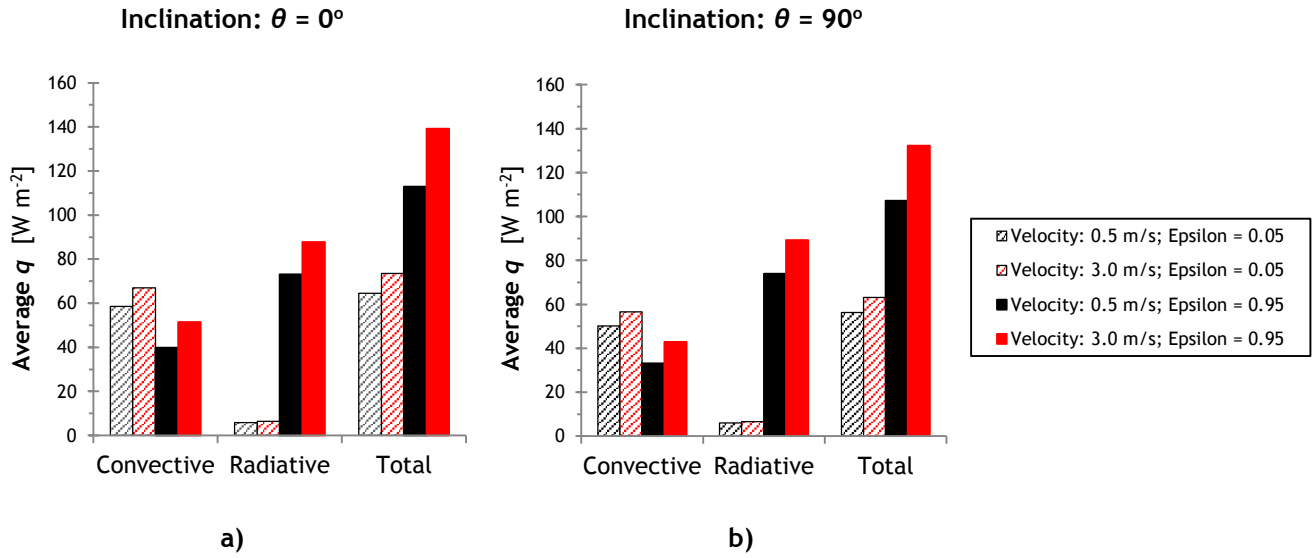

Figure 10 - Comparison of convective, radiative and total average heat fluxes on the skin (boundary 1) for different values of inlet velocity u_{in}, emissivity of the inner fabric ("Epsilon") and two inclinations of the enclosure: a) θ = 0º; b) θ = 90º. Since the skin is at a higher temperature than the surroundings, heat fluxes correspond to heat losses from the skin to the environment.

Finally, comparison of average heat fluxes on the skin from horizontal (Figure 10a) to vertical enclosures (Figure 10b), enables to conclude that convective heat fluxes decrease around 14 to 17%. Regarding radiation, average radiative heat fluxes are, as in the previous section, practically constant between horizontal and vertical enclosures (variations within 3%). These and other aspects will be more thoroughly discussed in the following section, which is dedicated to the effects of inclination.

3.3. Effects of Inclination

The inclination of the enclosure was varied in the range -180º to 180º, while keeping initial solution conditions constant for all simulated cases. The complete range of inclinations covers all situations, from a completely inverted enclosure (θ = ±180º) to the horizontal enclosure (θ = 0º), including also vertical enclosures, with either descending (θ = 90º) or ascending external air flow (θ = -90º). *Ra* varied in the range 2.0×10^5 to 2.9×10^5, except for θ = 180º ($Ra = 3.4 \times 10^5$ for $\varepsilon_{inner\ fabric} = 0.05$), for which convergence issues are reported (Table 4 of section *2. Materials and methods*). However, *Ra* values are not comparable in this section between different inclinations, since the characteristic length for natural convection ([7]) changes with θ and the current definition of *Ra* considers the constant thickness of the air gap ([8]). Thus, for meaningful comparisons, one should use *Ra* values based on the characteristic length (Sobera, 2006, p. 116).

Resulting average *Nu* values on the skin are plotted as function of enclosure's inclination in Figure 11. Selected temperature and velocity contours are presented in Figure 12 and Figure 13, only for $\theta \geq 0º$ (descending external air flow). Heat flux profiles along the skin and the top of the fabric are presented in Figure 14, while corresponding profiles for local temperature and total heat transfer coefficient profiles along the top of the fabric are presented in Figure 15. Finally, average heat fluxes on the skin are compared in Figure 16.

Since average Nu_{conv} values (skin) are practically symmetric at θ = 0º (Figure 11), differing by no more than 10% for $|\theta| \geq 9º$, analysis is next detailed for cases of positive θ. Differences between positive and corresponding negative inclinations will be addressed later in this section.

[7] The characteristic length in natural convection is defined as the maximum distance in the direction of gravity, within the enclosure (Sobera, 2006, p. 116).

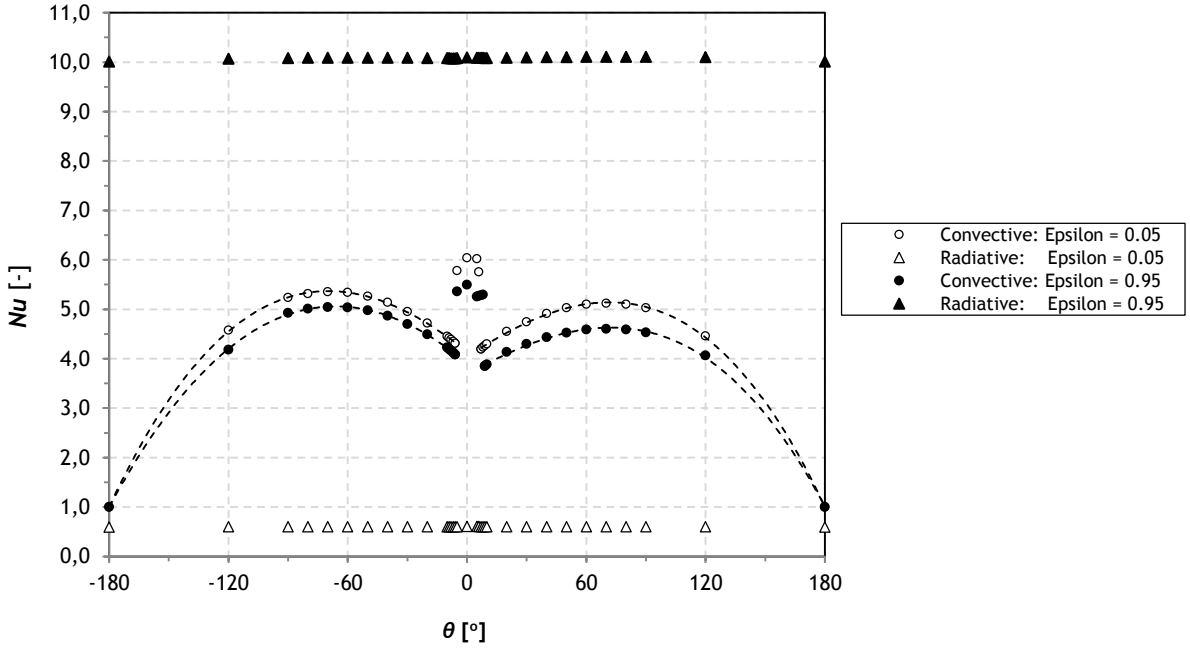

Figure 11 – Average convective and radiative *Nu* values ([8]) on the skin as function of enclosure's inclination, for inner fabric emissivity of 0.05 and 0.95. Dashed trend lines correspond to 3rd order polynomial regressions for inclination values associated with the single-cell flow mode (for expressions, please refer to Annex 7 – *Polynomial regressions*). These regressions exclude points around inclination $\theta = 0^o$ ($-5^o \leq \theta \leq 6^o$, for inner fabric's emissivity 0.95, and $-5^o \leq \theta \leq 8^o$, for emissivity 0.95).

For low values of θ, it is observed a decrease in the number of roll cells with increasing θ (Figure 12 and Figure 13). Specifically, the transition angle from multi- to single-cell flow mode was observed to occur at $\theta = 6^o$ to 7^o, for $\varepsilon_{inner\ fabric} = 0.05$, and at $\theta = 8^o$ to 9^o, for $\varepsilon_{inner\ fabric} = 0.95$. Khezzar et al. (2012) obtained slightly higher transition angles (between 10 to 15º) for zero start-up fields (constant initial conditions). However, differences between both studies should be acknowledged: Khezzar et al. (2012) do not include radiation in their calculations and they consider active walls as isothermal (no external forced convection); besides, these authors use different aspect ratios (AR = 3 and 6, compared to 4, in the present study), as well as different Ra values ($Ra = 1x10^5$ and $1x10^6$, compared to $2.0x10^5 < Ra < 3.0x10^5$, presently). Several authors have also reported that the transition angle is strongly dependent on initial solution conditions, giving rise to the so-called hysteresis effect, which results in different transition angles for increasing or decreasing θ (Khezzar et al., 2012; Soong & Tzeng, 1996; H. Wang & Hamed, 2006). In the present study,

[8] Please refer to *Annex 6 – Mathematical formulae*.

initial conditions were maintained and none of the simulations was initialized with the solution from a consecutive inclination. Thus, the hysteresis effect is not considered in the present study, with the advantage of making each simulation completely independent from all other results. However, it should be noted that alternative (real) solutions, or sequences of solutions, do probably exist.

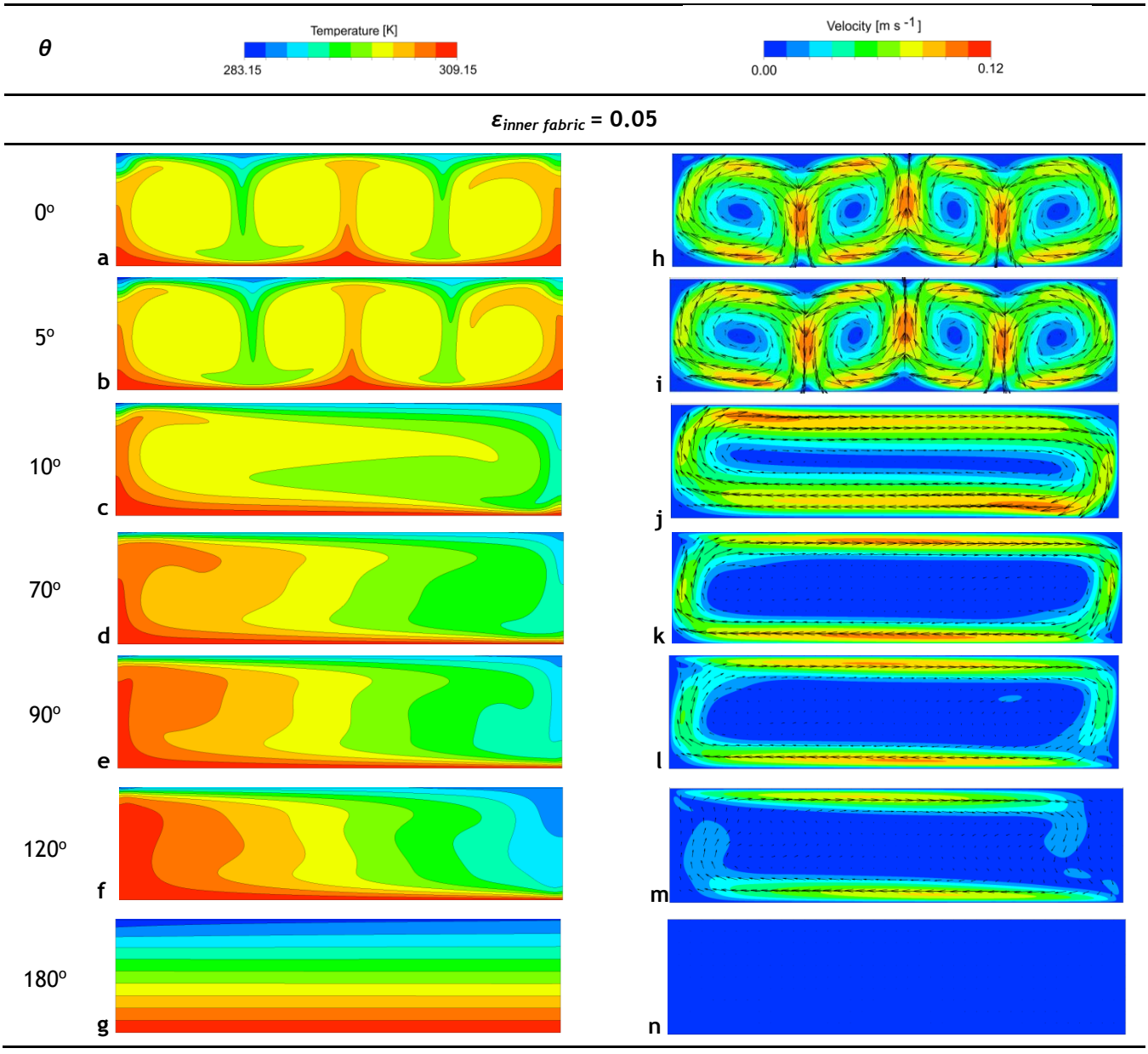

Figure 12 - Temperature and velocity contours in the air gap (domain A, Figure 1a) for inner fabric emissivity of 0.05 and several inclinations of the enclosure (from 0 º to 180º).

The fact that the transition angle is slightly higher for $\varepsilon_{inner\ fabric}$ = 0.95 than for $\varepsilon_{inner\ fabric}$ = 0.05 suggests that an increase in radiative heat exchange contributes to slightly delay the transition from multi- to single-cell flow mode (difference in transition angle of around 2º). Probably, the fact that temperatures in the enclosure are more homogeneous for $\varepsilon_{inner\ fabric}$ = 0.95 (Figure 13 left column, compared to Figure 12, left column) contributes to slightly stabilise multi-cell patterns,

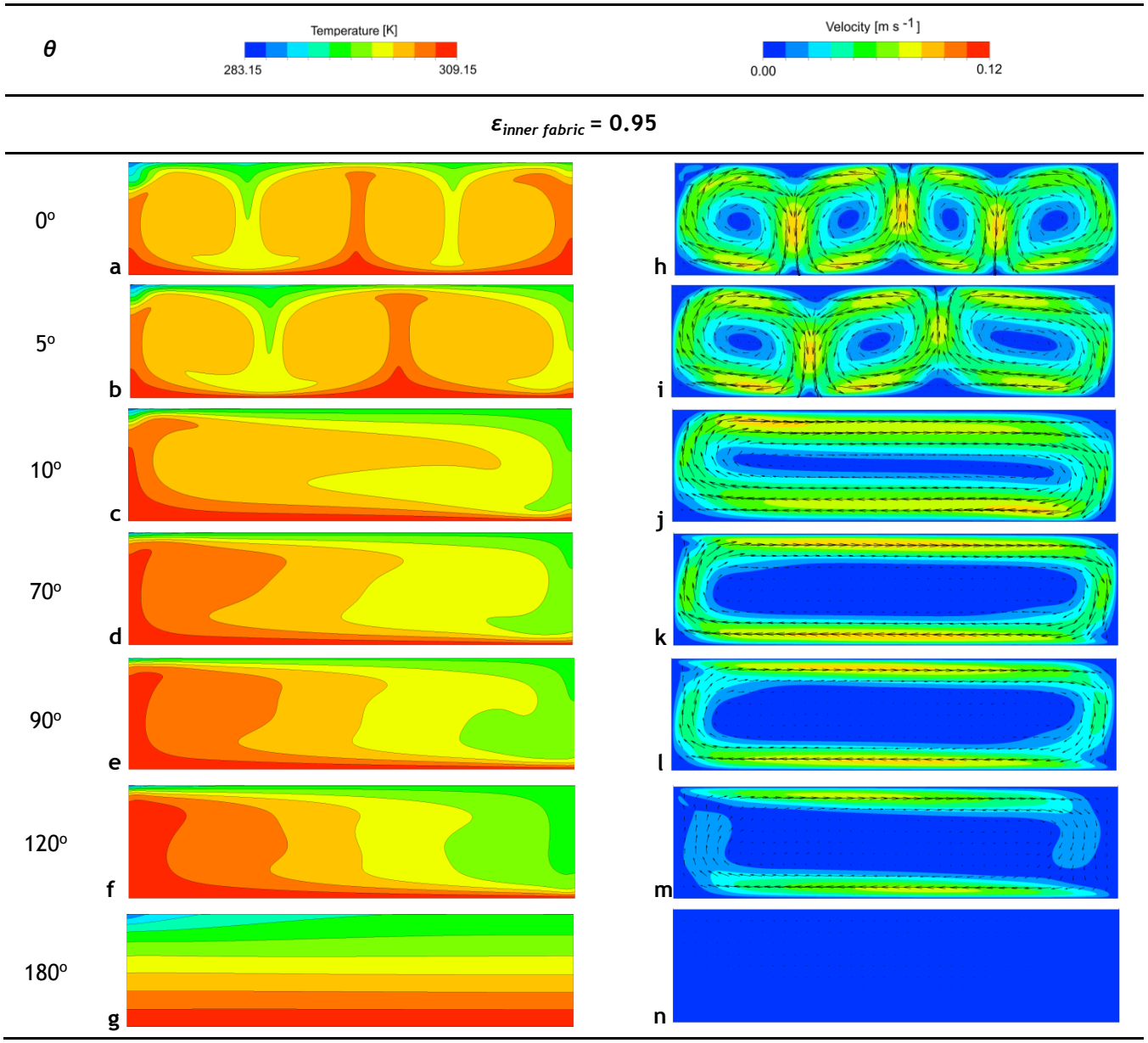

Figure 13 - Temperature and velocity contours in the air gap (domain A, Figure 1a) for inner fabric emissivity of 0.95 and several inclinations of the enclosure (from 0 º to 180º).

through lowering *Ra* values (*Ra* was observed to be up to 45% higher for $\varepsilon_{inner\ fabric}$ = 0.05, compared to $\varepsilon_{inner\ fabric}$ = 0.95).

For inclinations associated with the multi-cell flow mode ($\theta < 9^o$), the decrease in number of roll cells (Figure 12 and Figure 13) is associated with a sharp decrease in Nu_{conv} (Figure 11), demonstrating that a higher number of roll cells corresponds to higher efficiency of convective heat transfer (higher Nu_{conv}).

For inclinations corresponding to the single-cell flow mode ($\theta \geq 9^o$), Nu_{conv} follows a clear trend as a function of θ, which is well represented by 3rd order polynomial regressions (Figure 11; minimum correlation coefficient r^2 of 0.9993; please refer to Annex 7 – Polynomial regressions). It is also observed a local maximum in Nu_{conv} at around $\theta = 70^o$ (Figure 11). This maximum is probably associated with the increase in the characteristic length (the maximum distance in the direction of gravity; Sobera, 2006, p. 116) as the enclosure approaches the vertical position ($\theta = 90^o$). However, the occurrence of the maximum at $\theta < 90^o$ is explained by generally higher velocities in the enclosure for this range of inclinations (Figure 13, e.g. *k* compared to *m*), resulting from the warmer surface (skin) being at a lower position relative to the colder surface (fabric). An increase in Nu_{conv} for $\theta < 70^o$ is consistent with velocity contours of Figure 12 and Figure 13 (from j to k): from $\theta = 10^o$ to $\theta = 70^o$, it is noticeable a decrease in thickness of the moving air layer in the vicinity of the walls and also an increase in the *x*-direction span of the zone of maximum velocity near the walls.

For $\theta > 90^o$, the colder surface (fabric) stands at a lower position relative to the warmer surface (skin). Correspondingly, lower values for Nu_{conv} are observed, as is seen by comparing $\theta = 120^o$ to $\theta = 60^o$ (Figure 11). This is also consistent with a decrease in velocity magnitudes inside the enclosure for $\theta > 90^o$ (Figure 12l-n and Figure 13l-n).

The existence of a local maximum in Nu_{conv} at around $\theta = 70^o$ was also observed by Khezzar et al. (2012). Once differences between the two studies have

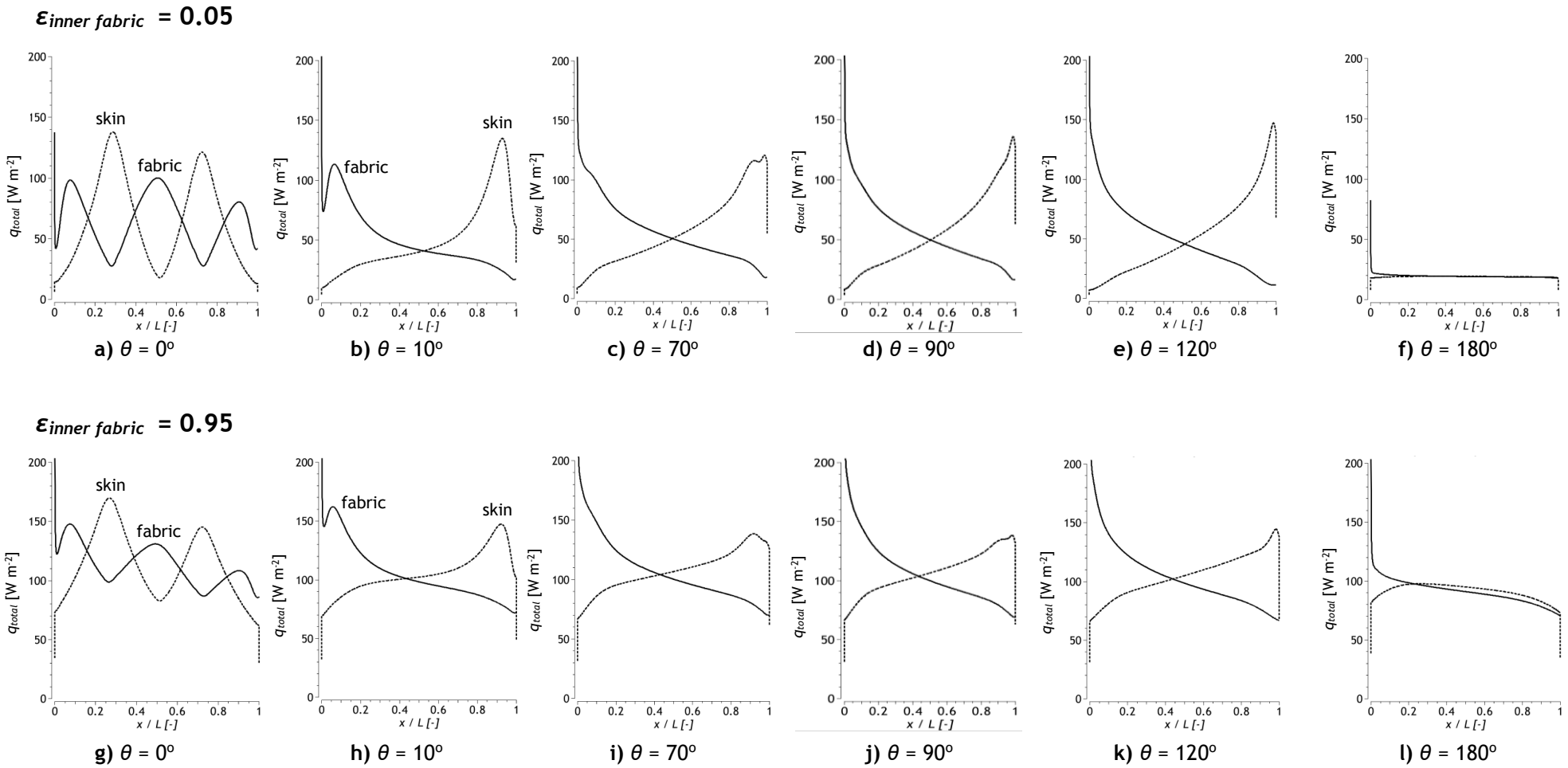

Figure 14 - Comparison of heat flux profiles (q_{total}) along the top of the fabric (solid lines) and along the skin (dashed lines) for several inclinations of the enclosure (θ = 0º, 10º, 70º, 120º, 180º): **a-e)** $\varepsilon_{inner\ fabric}$ = 0.05; **f-j)** $\varepsilon_{inner\ fabric}$ = 0.95.

been acknowledged, the value of inclination corresponding to this local maximum is surprisingly similar, within ±10º from the value reported in the referred study (Khezzar et al., 2012, p. 233). This gives further confidence on current results, along with the fact that Nu_{conv} curves of Figure 11 are confined by curves obtained in previous studies for higher and lower Ra values (Figures 3 and 4 of Khezzar et al. (2012, p. 233), for $Ra = 10^5$ and 10^6, compared to Figure 15 of the present study).

Profiles of Figure 14 and Figure 15 enable us to further analyse how transitions in flow patterns affect local variables on the skin and on the top of the fabric. First of all, profiles for heat flux are not symmetrical at $x/L = 0.5$ for an even number of roll cells ($\theta = 0º$). Secondly, for the single-cell flow mode ($\theta \geq 10º$), profiles for heat flux at the top of the fabric are different from x-wise inverted skin profiles; most notably, concerning the top of fabric, heat fluxes steeply increase for $x/L \rightarrow 0$, which does not happen in skin profiles for $x/L \rightarrow 1$ (Figure 14). All these facts are due to the existence of a developing external thermal boundary layer.

Also, due to this external boundary layer, temperature generally increases along the top of the fabric (Figure 15a and Figure 15b, from $x/L = 0$ to $x/L = 1$). Temperature profiles for a completely inverted enclosure ($\theta = 180º$, Figure 15a and Figure 15b, red lines), which corresponds to pure conduction inside the enclosure (in Figure 11, Nu_{conv} ($\theta = 180º$) ≈ 1; in Figure 12n and Figure 13n, velocity fields are practically null), are good examples of monotonic increases in temperature along the fabric, as created by the developing external thermal boundary layer. However, deviations occur for all cases other than $\theta = 180º$, arising from the onset of internal natural convection, the waviness of these profiles being dependent on the number of roll cells in the enclosure (Figure 12 and Figure 13).

Regarding local convective heat transfer coefficients (Figure 15c and Figure 15d), oscillations are also observed, except for $\theta = 180º$ (pure conduction). This, as explained in previous sections, is due to the fact that q_{conv} is higher (or lower) than would have been expected from the temperature difference between the fabric (local T) and the inlet air (T_c). Additionally, non-monotonic behaviour in h_{conv} profiles is restricted to $\theta < 9º$ (multi-cell flow mode), being practically negligible for $\varepsilon_{inner\ fabr} = 0.95$ (Figure 15d).

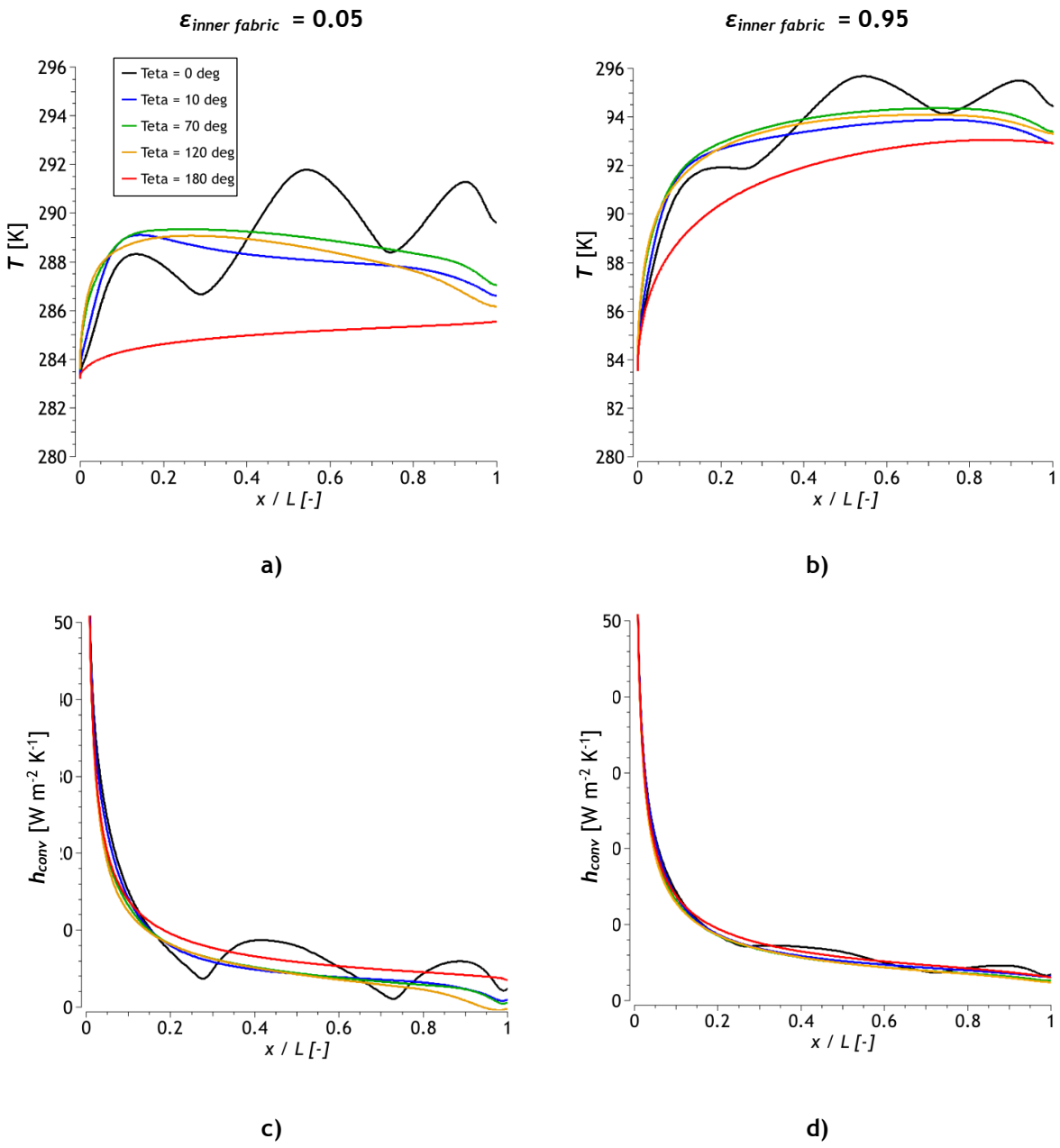

Figure 15 - Comparison of temperature (T) and local convective heat transfer coefficient profiles (h_{conv}) along the top of the fabric (boundary 7, Figure 2) for several values of inclination (θ = 0º, 10º, 70º, 120º, 180º) and two values for the emissivity of the inner fabric: a,c) $\varepsilon_{inner\ fabric}$ = 0.05; b,d) $\varepsilon_{inner\ fabric}$ = 0.95.

Aiming at a more detailed analysis of the oscillatory behaviour of h_{conv} profiles (Figure 15c and Figure 15d), isotherms for the external domain are plotted for θ = 0º and θ = 90º in Figure 17 (only for $\varepsilon_{inner\ fabric}$ = 0.05). The existence of wavy isotherms within the external thermal boundary layer (air layer in which T varies),

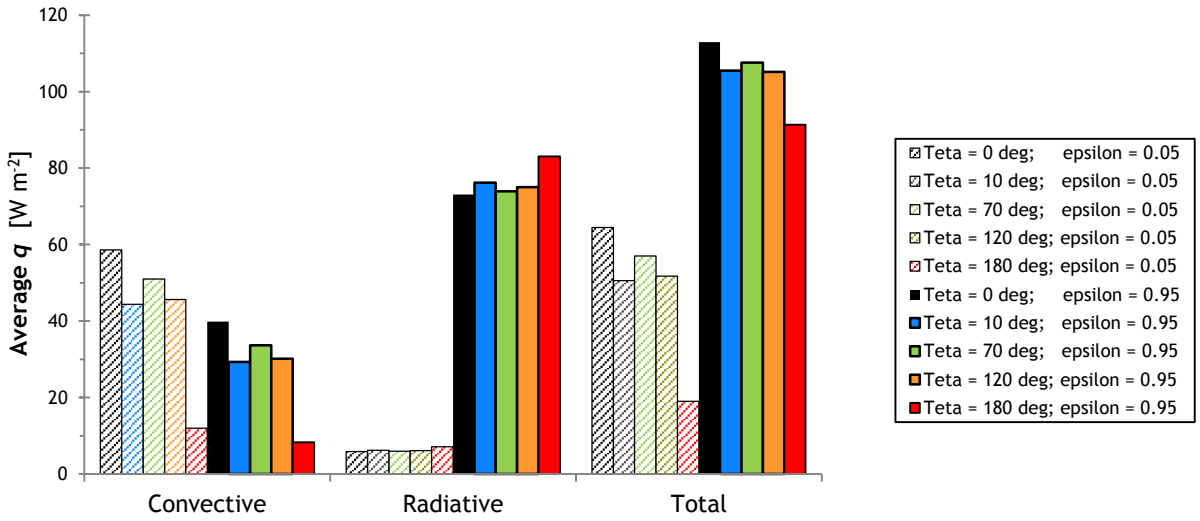

Figure 16 – Average heat fluxes (convective, radiative and total) on the skin, for two emissivity values of the inner fabric (0.05 and 0.95) and several inclinations (θ = 0, 10, 70, 120, and 180º). AR = 4, u_{in} = 0.5 m s^{-1}, H_1 = 0.052 m. Since the skin is at a higher temperature than the surroundings, heat fluxes correspond to heat losses from the skin to the environment.

as observed in Figure 17, indicates that thicknesses of thermal layers in the vicinity of the fabric do not evolve monotonically along x-coordinates. Since the convective coefficient, h_{conv}, is theoretically given by the quotient between the conductivity of these layers (assumed to be constant) and their thickness, variations in layer thickness are accountable for the waviness of h_{conv} in Figure 15c and Figure 15d. It is noteworthy that, also for θ = 90º, isotherms do not evolve monotonically, curving downwards for high x-coordinates (Figure 17b); this is related to a change in the internal flow direction in the vicinity of the inner fabric (Figure 12l, on the right end of the enclosure), which contributes to decreasing the temperature of the fabric.

A comparison of h_{conv} curves obtained in this study to those obtained from a correlation (which assumes a laminar two-dimensional boundary layer over a flat isothermal fabric) is given in Figure 18. The correlation is given by (Lienhard IV & Lienhard V 2003, 304):

$$h_{conv} = 0.332 \cdot k / x \cdot Re^{1/2} Pr^{1/3} \qquad \text{Equation 12}$$

in which the properties of the fluid were obtained by taking into account the inlet air temperature and the average temperature at the top of the fabric for simulated

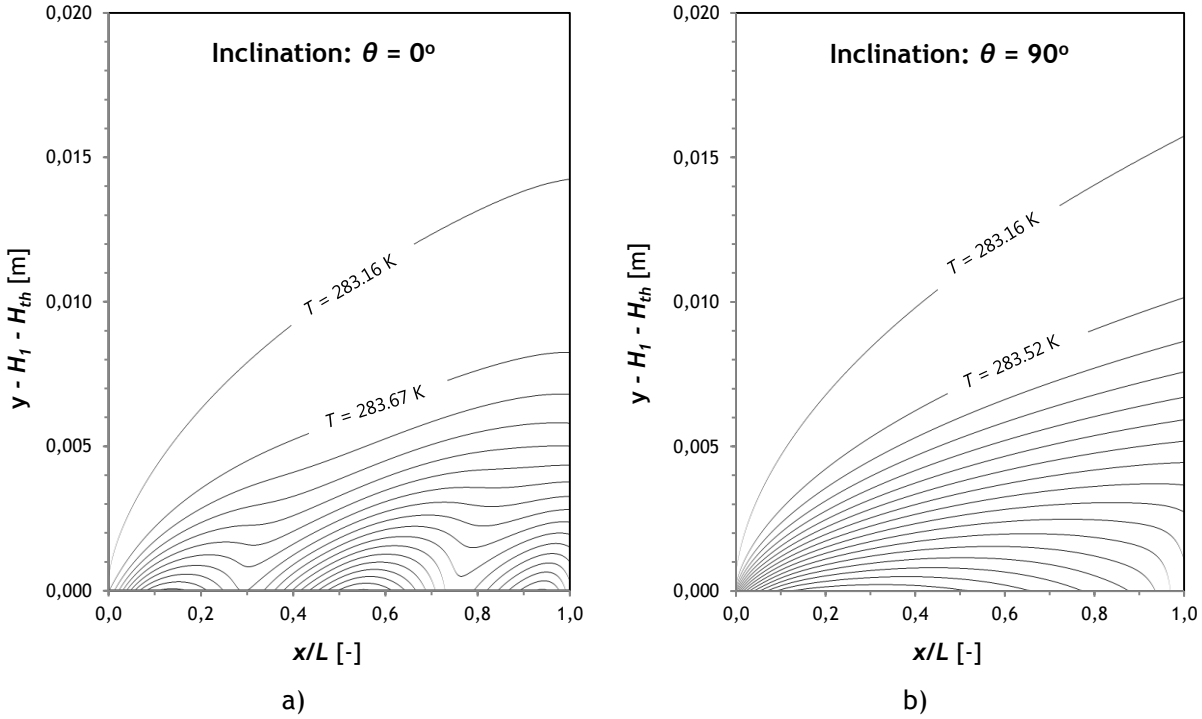

Figure 17 - Isotherms in the external domain (domain C, Figure 1a), for a) horizontal enclosure (θ = 0º) and **b) vertical enclosure** (θ = 90º). 20 isotherms are plotted for each case, with 19 constant temperature intervals in the range T_{min} (= T_c + 0.01 K = 283.16 K) to T_{max}, the later corresponding to the maximum temperature on the top of the fabric: T_{max} = 292.77 K for θ = 0º; T_{max} = 290.09 K for θ = 90º. Conditions: AR = 4, u_{in} = 0.5 m s^{-1}, $\varepsilon_{inner\ fabric}$ = 0.05; H_1 = 52 mm.

cases of $\varepsilon_{inner\ fabric}$ = 0.05. It is observed, from Figure 18, that considerable over- and under-estimation occurs for both horizontal (θ = 0º) and vertical enclosures (θ = 90º). Specifically, the maximum local under-estimation error for the correlation--based h_{conv} is higher than 50% relative to the numerically obtained value (for $x/L \rightarrow 0$, for both θ = 0º and θ = 90º), while the maximum local over-estimation error is higher than 9-fold the numerically obtained value (for θ = 90º, high x-coordinates). This confirms that the use of such simplified correlations to predict heat fluxes may be subjected to significant local errors in the current setup, as was already shown by Couto & Mayor (2013). The current study adds that such discrepancies can be even higher than previously reported, as the inclination is changed from the horizontal to the vertical position; the later discrepancies are especially significant at high x-coordinates, where external isotherms curve downward (Figure 17b, high x-coordinates) and the thickness of thermal layers varies non-monotonically.

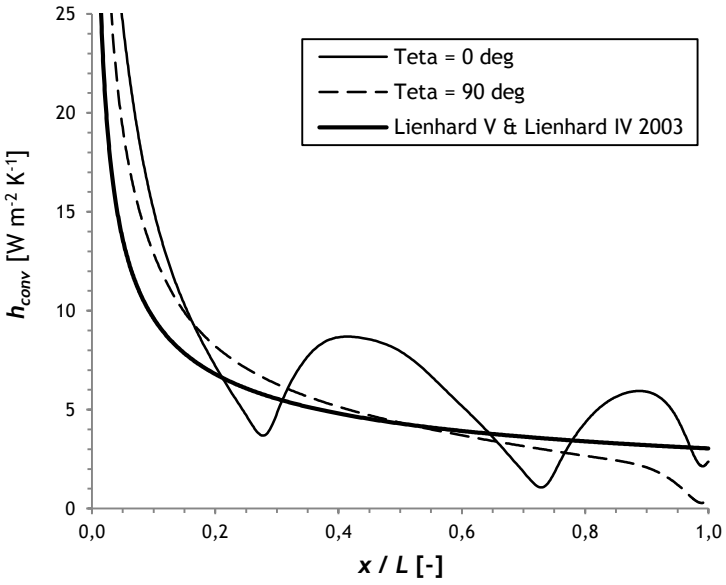

Figure 18 – Comparison of a correlation-based profile for convective heat transfer coefficient, h_{conv}, to results obtained in this study along the top of the fabric (boundary 7, Figure 2). Results from this study correspond to AR = 4, $\varepsilon_{inner\ fabric}$ = 0.05 and two values of inclination (θ = 0 and 90º). The correlation is given by $h_{conv} = 0.332 \cdot k/x \cdot Re^{1/2} Pr^{1/3}$ (Lienhard IV & Lienhard V, 2003, p. 304), being valid for laminar two-dimensional boundary layers over flat **isothermal** surfaces; the inlet air temperature and the average temperature of the fabric for the presently simulated cases were considered in the correlation.

As in previous sections, average Nu_{conv} values (Figure 11) and average convective heat fluxes (Figure 16) are observed to be generally lower for increased inner fabric's emissivity ($\varepsilon_{inner\ fabric}$ = 0.95). This happens for the same reasons presented then: increased radiant heat exchange (for higher emissivity of the inner fabric) decreases temperature gradients, which in turn leads to lower buoyancy forces and, consequently, less convective heat transfer.

Differently from Nu_{conv}, average Nu_{rad} values were observed to be practically independent from inclination, with a maximum variation within 3% (Figure 11). Specifically, for $\varepsilon_{inner\ fabric}$ = 0.95, the minimum and maximum Nu_{rad} values corresponded to 10.01 and 10.11, respectively, whereas for $\varepsilon_{inner\ fabric}$ = 0.05 the minimum and maximum corresponded to 0.59 and 0.60, respectively. These negligible variations in Nu_{rad} are associated with practically constant average radiative heat fluxes for the tested angles (Figure 16). An exception to this is the significant increase in q_{rad} from θ = 120º to θ = 180º (Figure 16, for $\varepsilon_{inner\ fabric}$ = 0.95). This increase is due to the significant cooling of the fabric from θ = 120º to θ = 180º (Figure 15a and Figure 15b), which means increased temperature difference between the fabric and the skin. Since both effects (increasing q_{rad} and increasing ΔT) tend to cancel out (please refer

to Equation A.3, in Annex 6 – *Mathematical formulae*), Nu_{rad} remains fairly constant regarding inclination.

Finally, conclusions drawn for $\theta \geq 0^o$ (descending external air flow) are generally applicable to $\theta < 0^o$ (ascending external air flow). However, there are some differences, which will be next discussed.

The most obvious difference from positive to corresponding negative inclination values consisted in an inversion of flow patterns in the x-direction (please refer to Annex 10 – Flow pattern inversion). Accordingly, local heat fluxes on the skin are practically symmetrical at $x/L = 0.5$ (as shown in Figure 19 for $\theta = \pm 70^o$), except in that local heat fluxes are up to 15% higher for negative inclinations (ascending external air flow). Also, Nu_{conv} values of Figure 11 are observed to be slightly higher for negative inclinations, compared to positive inclinations (differences within 10% for $|\theta| \geq 9^o$; Figure 11). These slight differences are probably due to the fact that, in the present model, natural convection is taken into account also in the external domain. In fact, the ratio Gr/Re^2 ([9]), which is frequently used in evaluating the relative importance of natural and forced convection (Çengel, 2003c, p. 487), was observed to be higher than 0.1 and lower than 10, meaning that neither natural nor forced convection are negligible. Thus, buoyancy-induced motion in the external domain assists forced convection for $\theta < 0^o$ (ascending flows for both natural and forced convection), whereas it opposes forced convection for $\theta > 0^o$ (ascending natural convection flow versus descending forced flow). This explains the higher Nu_{conv} values obtained for negative inclination values (Figure 11).

Additionally, the transition angle (from multi- to single-cell flow mode) was seen to be lower for negative inclinations ($\theta = -5^o$) compared to positive inclination values ($\theta = 6^o$ to 9^o). This is probably also related to the effect of changing the buoyancy-induced motion in the external domain from opposing forced convection ($\theta > 0^o$) to assisting forced convection ($\theta < 0^o$). Thus, from positive to corresponding negative inclination values, slight increases of around 1% in Ra in the enclosure occurred, which might have contributed to decreasing the stability of internal multi-cell flow

[9] Gr corresponds to the Grashof number, defined as $Gr = Ra/Pr$.

modes, in a manner similar to the effect of changing $\varepsilon_{inner\ fabric}$ (as seen above in this section for positive inclinations).

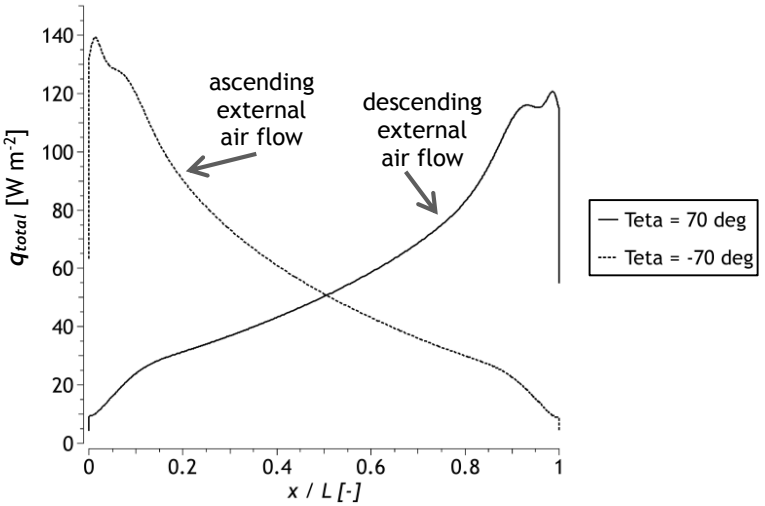

Figure 19 – Comparison of heat flux profiles on the skin between a case with θ = 70º (descending external air flow) and the corresponding case with negative inclination (ascending external air flow).
Conditions: AR = 4; u_{in} = 0.5 m s^{-1}; H_1 = 52 mm; $\varepsilon_{inner\ fabric}$ = 0.05).

3.4. Effects of Fabric's Thermal Resistance

Fabric's thermal conductivity was decreased tenfold (from 9.524x10^{-2} to 9.524x10^{-3} W m^{-1} K^{-1}), which implied an increase in its resistance, R_{CT}, from 0.0105 to 0.1050 K m^2 W^{-1} (constant fabric thickness of 1 mm). Additionally, two values of emissivity were tested. *Ra* varied in the range 1.45x10^5 to 2.72x10^5 (Table 7).

Obtained average *Nu* values on the skin ([10]) are presented in Table 7. Temperature and velocity contours are displayed in Figure 20. Heat flux profiles along the skin and the top of the fabric are presented in Figure 21, while corresponding profiles for local temperature and convective heat flux coefficient h_{conv} ([10]) profiles along the fabric are presented in Figure 22. Finally, average heat fluxes on the skin are compared in Figure 23.

[10] Please refer to *Annex 6 – Mathematical formulae*.

Table 7 - Average *Nu* on the skin (boundary 1, Figure 2) as a function of fabric's thermal resistance and emissivity of inner fabric.

θ [°]	$\varepsilon_{inner\ fabric}$	R_{CT} = 0.0105 K m^2 W^{-1}				R_{CT} = 0.1050 K m^2 W^{-1}			
	[-]	Nu_{conv} [-]	Nu_{rad} [-]	Nu_{total} [-]	Ra [-]	Nu_{conv} [-]	Nu_{rad} [-]	Nu_{total} [-]	Ra [-]
0	**0.05**	6.040	0.603	6.644	2.72E+05	5.809	0.614	6.422	2.23E+05
	0.95	5.498	10.095	15.593	2.03E+05	5.132	10.316	15.447	1.45E+05

An increase in R_{CT} is seen to produce a general decrease in velocity magnitudes in the enclosure: from Figure 20 (right column), velocities are observed to decrease from *e* to *f* and from *g* to *h*. These changes are associated with lower temperature gradients near the skin for high R_{CT}, as seen in temperature contours of Figure 20 (left column): by comparing contours for the same $\varepsilon_{inner\ fabric}$, thermal boundary layers on the skin are observed to be thicker for the higher R_{CT}. However, even though gradients near the skin are lower for high R_{CT}, corresponding to decreased *Ra* values in the enclosure (Table 7), temperatures along the top of the fabric are also lower for high R_{CT} (Figure 22a and Figure 22b, solid lines). This apparent contradiction is explained by the fact that a higher R_{CT} leads to a higher difference between inner and outer fabric's temperature (Figure 22a and Figure 22b, dashed and solid lines, respectively): a difference of approx. 10°C for high R_{CT}, compared to less than 2°C for low R_{CT}. Since what ultimately drives internal natural convection is the **inner** fabric's temperature (Figure 22a and Figure 22b, dashed lines) and temperatures are markedly different between the inner and the outer surfaces of the fabric for high R_{CT}, one should solely rely on temperature gradients inside the enclosure in explaining the decrease in intensity of natural convection with increasing R_{CT}. Thus, since the temperature of the inner fabric is generally higher for high R_{CT}, skin-fabric temperature gradients are lower and the intensity of natural convection is decreased.

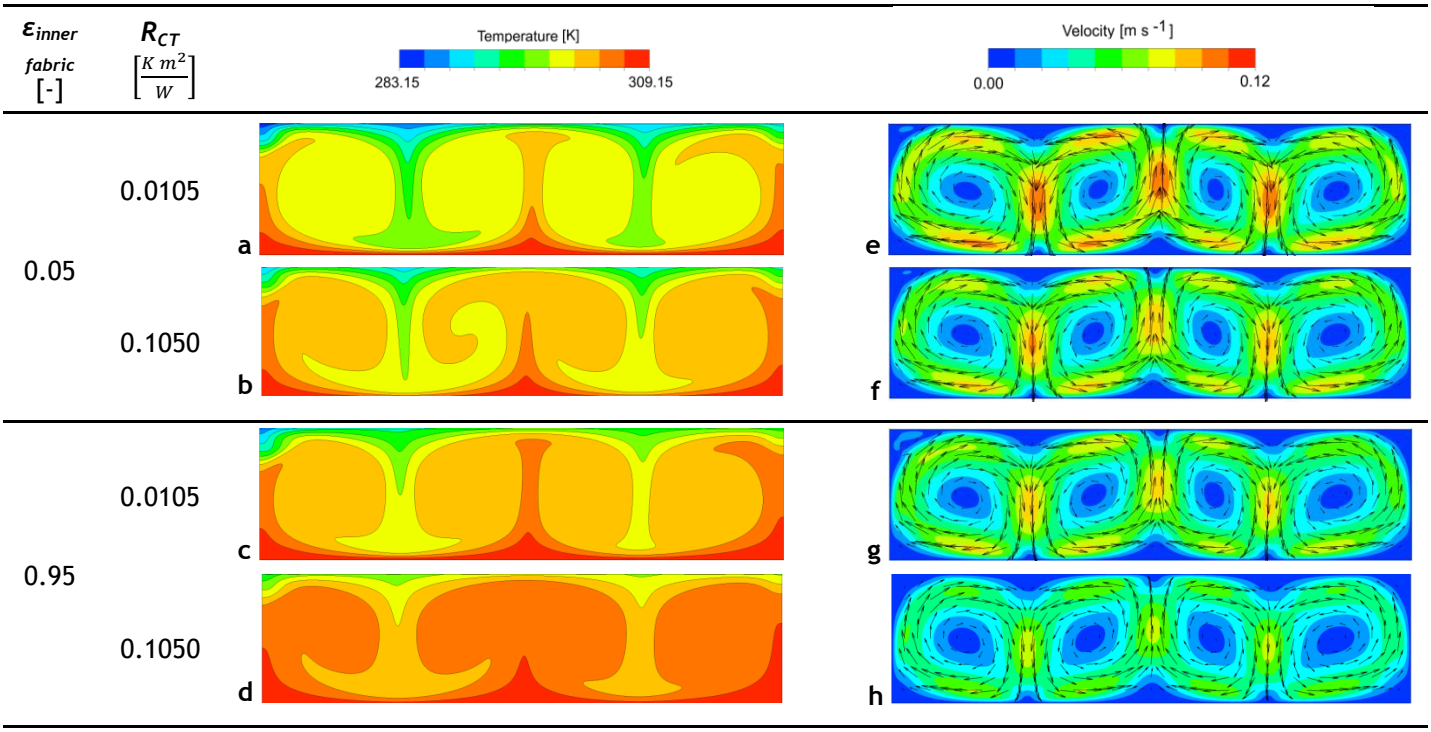

Figure 20 - Temperature and velocity contours in the air gap (domain A, Figure 1) for two values of thermal resistance of the fabric (R_{CT} = 0.0105 and 0.1050 K m^{-1} W^{-1}), and two values of inner fabric emissivity (0.05 and 0.95).

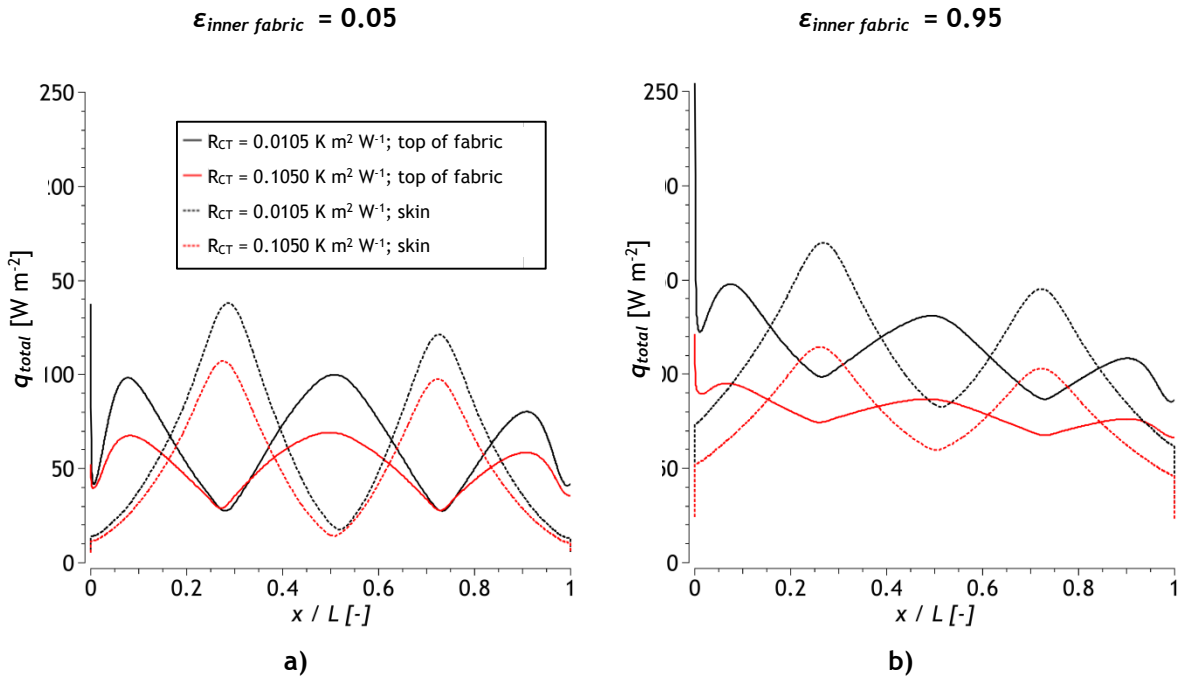

Figure 21 - Comparison of heat flux (q_{total}) profiles along the top of the fabric (boundary 7, Figure 2) and along the skin (boundary 1, Figure 2) for two values of thermal resistance of the fabric (R_{CT} = 0.0105 and 0.1050 K m^2 W^{-1}) and two values of emissivity: **a)** $\varepsilon_{inner\ fabric}$ = 0.05; **b)** $\varepsilon_{inner\ fabric}$ = 0.95.

By increasing R_{CT}, a decrease in intensity of internal natural convection is also associated with decreased local heat fluxes (Figure 21). Additionally, these heat fluxes have decreased amplitude of oscillation along skin and top of the fabric (idem). Similarly to sub-section *Effects of Air Velocity*, for low emissivity ($\varepsilon_{inner\ fabric}$ = 0.05), changes are more significant around local maxima (Figure 21a), whereas for $\varepsilon_{inner\ fabric}$ = 0.95 both maxima and minima are changed (Figure 21b). This is due to a higher relative importance of radiation for higher $\varepsilon_{inner\ fabric}$, as explained above, in sub-section *Effects of Air Velocity*.

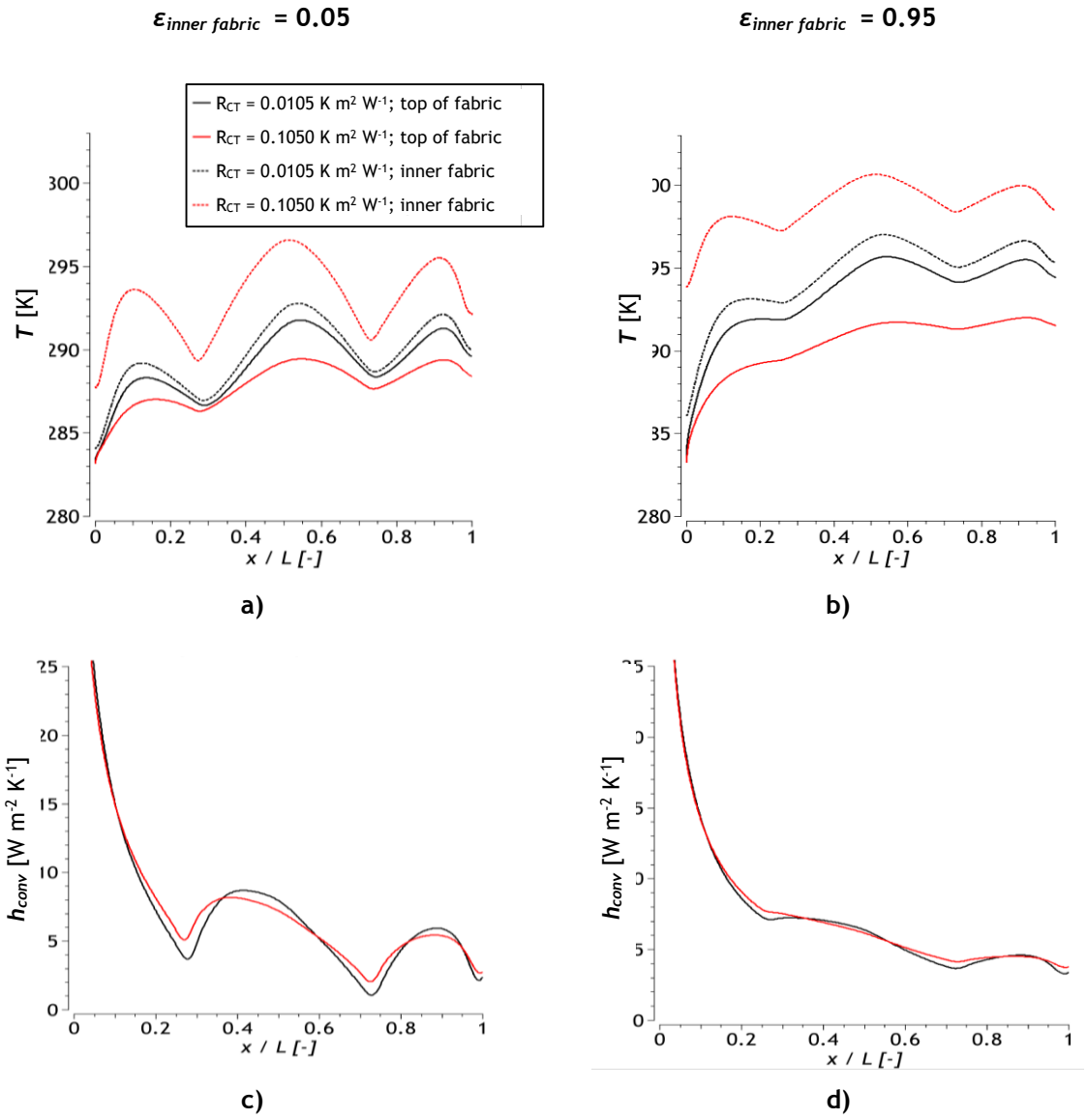

Figure 22 - Comparison of temperature (T) and local convective heat transfer coefficient profiles (h_{conv}) along the top of the fabric (boundary 7, Figure 2) for two values of thermal resistance of the fabric (R_{CT} = 0.0105 and 0.1050 K m² W⁻¹) and two values of emissivity: a,c) $\varepsilon_{inner\ fabric}$ = 0.05; b,d) $\varepsilon_{inner\ fabric}$ = 0.95.

From temperature and h_{conv} profiles on the top of the fabric (Figure 22, solid lines), it is possible to observe that both variables become less wavy as R_{CT} is increased. This is attributed to an increased decoupling of internal and external local heat transfer as the thermal insulation of the fabric increases. Thus, the fabric is seen to have a buffering effect on heat transfer from the body to the environment, which is fully consistent with the protective role of clothing.

Finally, total average heat fluxes at the skin (Figure 23) are observed to decrease in the range 20 to 30% as R_{CT} is increased tenfold. Additionally, the decrease is more significant for high $\varepsilon_{inner\ fabric}$, corresponding to about 29.4% for $\varepsilon_{inner\ fabric} = 0.95$, compared to 20.7% for $\varepsilon_{inner\ fabric} = 0.05$. The importance of considering radiative heat exchange between skin and fabric is once again evident, since the effect of R_{CT} (through changing k_s) on total heat transfer is amplified by increasing the relevance of radiative heat transfer.

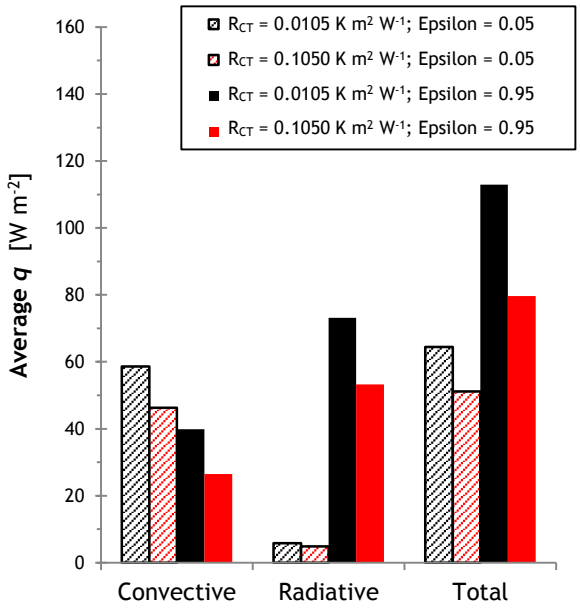

Figure 23 - Comparison of convective, radiative and total average heat fluxes on the skin (boundary 1) for two values of thermal resistance of the fabric (R_{CT} = 0.0105 and 0.1050 K m^2 W^{-1}) and two values of emissivity of the inner fabric (Epsilon = 0.05 and Epsilon = 0.95, where Epsilon = $\varepsilon_{inner\ fabric}$). Since the skin is at a higher temperature than the surroundings, heat fluxes correspond to heat losses from the skin to the environment.

4. Conclusions and future work

The current study provides further insight regarding dry heat transfer in the microclimate located between the skin (represented by an isothermal wall) and the first layer of clothing fabric. This study focused on the effects of the air gap thickness (distance H_1), external forced convection (air velocity u_{in}), inclination relative to gravity (θ) and thermal conductivity of the fabric (k_s) on internal air flow patterns and on both local and global thermal quantities.

Regarding air gap thickness, even though internal natural convection did not occur for a horizontal enclosure with H_1 = 8 mm (in agreement with the obtained Rayleigh numbers), convection took place in the corresponding vertical enclosure (θ = 90º). Effects of air gap thickness were found to be generally in good agreement with previous studies, except for H_1 = 25 mm, for which the number of roll cells did not match previous numeric results obtained Couto & Mayor (2013). This exception is attributed to the possible existence of multiple steady-states.

Regarding the effects of air velocity, results were in good agreement with those of previous studies, with internal natural convection being intensified by an increase in u_{in}. Contrary to internal convection, the efficiency of radiation relative to conduction (as given by Nu_{rad}) was seen to be fairly constant relative to u_{in}, with increases in radiative heat fluxes corresponding to increases in temperature difference between the skin and the fabric.

The enclosure's inclination (θ) was a central parameter to the current study, and valuable conclusions could be drawn from analysis of its effects, namely:

1) Nu_{conv} was higher and varied more significantly in the range $-5º \leq \theta \leq 9º$, which corresponded to the multi-cell flow mode;
2) for $|\theta| \geq 9º$ (single-cell flow mode), Nu_{conv} followed a regular trend as a function of θ, which had local maxima at around θ = 70º and could be represented by 3rd order polynomial regressions ($r^2 \geq 0.9993$);
3) the transition angle from multi- to single-cell flow mode, located in the range $5º \leq |\theta| \leq 9º$, was seen to be slightly dependent on both the emissivity of the inner fabric and the signal of θ (transition angle varied no

more than 4º), which therefore have a weak influence on the stability of multi-cell flow modes;

4) the internal flow was seen to affect the thickness of external thermal layers, which varied non-monotonically along the length of the fabric, causing waviness in profiles of external local convective heat transfer coefficient (h_{conv});
5) when comparing results of local h_{conv} with those estimated using a correlation for an isothermal fabric's outer surface, it was observed that: the correlation had a local under-estimation error of up to 50% relative to the numerically obtained value (at low x coordinates, for both horizontal and vertical enclosures) and an over-estimation error of up to 9-fold the numerically obtained value, registered at high x-coordinates for a vertical enclosure; this indicates that considerable errors may occur when using such correlations to predict local heat fluxes in clothing applications;
6) differences in Nu_{conv} between positive and corresponding negative inclinations were seen to be within 10% for $|\theta| \geq 9^{o}$, with Nu_{conv} being slightly higher for negative θ (ascending external forced convection), probably due to the assisting effect of external natural convection on forced convection;
7) the efficiency of radiation (Nu_{rad}) did not vary significantly with θ.

Finally, the effects of increasing the fabric's thermal resistance were analysed. It was observed a decrease in the intensity of internal natural convection and an increasing decoupling of internal and external local heat transfer, as the thermal resistance of the fabric increased. Globally, total average heat fluxes at the skin decreased around 20-30% for a tenfold increase in thermal resistance of the fabric.

Throughout this study, we also reaffirmed the importance of including radiative heat transfer in modelling clothing microclimates, since radiative effects were seen to be intrinsically related to those of all other studied parameters.

In the current flat setup (rectangular representation of the microclimate), further investigation is needed regarding the effect of changing the aspect ratio of the enclosure, as well as of boundary conditions attributed to lateral walls, on local

and global thermal quantities. Additionally, the effect of changing the porosity of the fabric should be investigated in a concentric geometry, comprising a circular limb covered at a certain distance by a thin layer of fabric (as in Sobera & Kleijn, 2008). To the best of our knowledge, the coupling of a surface-to-surface radiation model (similarly to that used in the current study) to porous media modelling of the fabric have never been attempted within the study of heat transfer in clothing applications. The first steps have been taken in this direction within the project developed at EMPA, though not included in the current document for sake of conciseness. Finally, a more complete modelling approach would include mass transfer and latent heat, in order to consider the important effects of sweating on heat transfer.

References

Akiyama, M., & Chong, Q. P. (1997). Numerical analysis of natural convection with surface radiation in a square enclosure. *Numerical Heat Transfer, Part A: Applications*, *32*(4), 419–433. doi:10.1080/10407789708913899

Andrade, J., Costa, U., Almeida, M., Makse, H., & Stanley, H. (1999). Inertial Effects on Fluid Flow through Disordered Porous Media. *Physical Review Letters*, *82*(26), 5249–5252. doi:10.1103/PhysRevLett.82.5249

Angelova, R. a., Stankov, P., Simova, I., & Kyosov, M. (2013). Computational modeling and experimental validation of the air permeability of woven structures on the basis of simulation of jet systems. *Textile Research Journal*, *83*(18), 1887–1895. doi:10.1177/0040517513481869

ANSYS. (2011a). *ANSYS FLUENT Theory Guide* (14.0 ed.).

ANSYS. (2011b). *ANSYS FLUENT User's Guide* (14.0 ed., Vol. 15317).

ANSYS. (2013a). *ANSYS Fluent Meshing User's Guide* (15.0 ed., Vol. 15317).

ANSYS. (2013b). *ANSYS Fluent User's Guide* (15.0 ed.).

Barry, B. J. J., & Hill, R. W. (2003). Computational Modeling of Protective Clothing. *International Nonwovens Journal*, *12*(3), 25–34.

Barry, J., Hill, R., Brasser, P., Sobera, M. P., Kleijn, C., & Gibson, P. (2003). Computational Fluid Dynamics Modeling of Fabric Systems for Intelligent Garment Design. *Materials Research Bulletin*, *August*, 568–573.

Çengel, Y. A. (2003a). Chapter 12 - Radiation Heat Transfer. In *Heat Transfer: A Practical Approach* (pp. 605–666). McGraw-Hill.

Çengel, Y. A. (2003b). Chapter 7 - External forced convection. In *Heat Transfer: A Practical Approach* (pp. 367–418).

Çengel, Y. A. (2003c). Chapter 9 - Natural Convection. In *Heat Transfer: A Practical Approach* (2nd ed., pp. 459–514). McGraw-Hill.

Christon, M. A., Gresho, P. M., & Sutton, S. B. (2002). Computational predictability of time-dependent natural convection flows in enclosures (including a benchmark solution). *International Journal for Numerical Methods in Fluids*, *40*, 953–980. doi:10.1002/?d.395

Corcione, M. (2003). Effects of the thermal boundary conditions at the sidewalls upon natural convection in rectangular enclosures heated from below and

cooled from above. *International Journal of Thermal Sciences*, *42*(2), 199–208. doi:10.1016/S1290-0729(02)00019-4

Coulson, J. M., & Richardson, J. F. (1999). Volume 1 - Fluid Flow, Heat Transfer and Mass Transfer. In *Coulson & Richardson's Chemical Engineering* (6th ed.). Butterworth Heinemann.

Couto, S., & Mayor, T. S. (2013). *Heat transfer through air-fabric layers with flat and folded surface*. CENTI - Centre for Nanotechnology and Smart Materials, V. N. Famalicão.

Davis, G. D. W. (1983). Natural convection of air in a square cavity - a bench mark numerical solution. *International Journal for Numerical Methods in Fluids*, *3*, 249–264.

Döbrich, O., Gereke, T., & Cherif, C. (2014). Modelling of textile composite reinforcements on the micro-scale. *Autex Research Journal*, *1*(14), 10–15. doi:10.2478/v10304-012-0047-z

Dunn, M. W. (2000). *Investigating fluid flow through fabrics*. Philadelphia.

Gooijer, H., Warmoeskerken, M. M. C. G., & Groot Wassink, J. (2003). Flow Resistance of Textile Materials: Part I: Monofilament Fabrics. *Textile Research Journal*, *73*(5), 437–443. doi:10.1177/004051750307300511

Hart, J. E. (2006). Stability of the flow in a differentially heated inclined box. *Journal of Fluid Mechanics*, *47*(3), 547. doi:10.1017/S002211207100123X

Khezzar, L., Siginer, D., & Vinogradov, I. (2012). Natural convection in inclined two dimensional rectangular cavities. *Heat and Mass Transfer*, *48*, 227–239. doi:10.1007/s00231-011-0876-7

Lauriat, G., & Prasad, V. (1989). Non-Darcian effects on natural convection vertical porous enclosure. *International Journal of Heat and Mass Transfer*, *32*(11), 2135–2148.

Lienhard IV, J. H. ., & Lienhard V, J. H. (2003). *A heat transfer textbook* (3rd ed.). Massachusetts: Phlogiston Press.

Manz, H. (2003). Numerical simulation of heat transfer by natural convection in cavities of facade elements. *Energy and Buildings*, *35*(3), 305–311. doi:10.1016/S0378-7788(02)00088-9

Min, K., Son, Y., Kim, C., Lee, Y., & Hong, K. (2007). Heat and moisture transfer from skin to environment through fabrics: A mathematical model. *International Journal of Heat and Mass Transfer*, *50*(25-26), 5292–5304. doi:10.1016/j.ijheatmasstransfer.2007.06.016

Murakami, S., Kato, S., & Zeng, J. (2000). Combined simulation of airflow, radiation and moisture transport for heat release from a human body. *Building and Environment*, *35*, 489–500.

Rief, S., Laourine, E., Aibibu, D., Cherif, C., & Wiegmann, A. (2011). Modeling and CFD-simulation of woven textiles to determine permeability and retention properties. *AUTEX Research Journal*, *11*(3), 78–83.

Rossi, R. (2005). Interactions between protection and thermal comfort. In R. A. Scott (Ed.), *Textiles for protection* (p. 233). Cambridge: Woodhead Publishing Limited.

Sobera, M. P. (2006). *Flow, heat and mass transfer through protective textiles*. Technische Universiteit Delft.

Sobera, M. P., & Kleijn, C. R. (2008). T-RANS Simulations of Subcritical Flow with Heat Transfer Past a Circular Cylinder Surrounded by a Thin Porous Layer. *Flow, Turbulence and Combustion*, *80*(4), 531–546. doi:10.1007/s10494-008-9150-6

Soong, C. Y., & Tzeng, P. Y. (1996). Numerical study on mode-transition of natural convection in differentially heated inclined enclosures. *International Journal of Heat and Mass Transfer*, *39*(14), 2869–2882.

Tari, I., & Mehrtash, M. (2013). Natural convection heat transfer from inclined plate-fin heat sinks. *International Journal of Heat and Mass Transfer*, *56*(1-2), 574–593. doi:10.1016/j.ijheatmasstransfer.2012.08.050

Vafai, K., & Tien, C. L. (1981). Boundary and inertia effects on flow and heat transfer in porous media. *International Journal of Heat and Mass Transfer*, *24*, 195–203.

Van Den Brekel, L. D. M., & De Jong, E. J. (1989). Hydrodynamics in packed textile beds. *Textile Research Journal*, *59*(8), 433–440. doi:10.1177/004051758905900801

Vivek, V., Sharma, A. K., & Balaji, C. (2012). Interaction effects between laminar natural convection and surface radiation in tilted square and shallow enclosures. *International Journal of Thermal Sciences*, *60*, 70–84. doi:10.1016/j.ijthermalsci.2012.04.021

Wang, H., & Hamed, M. S. (2006). Flow mode-transition of natural convection in inclined rectangular enclosures subjected to bidirectional temperature gradients. *International Journal of Thermal Sciences*, *45*, 782–795. doi:10.1016/j.ijthermalsci.2005.07.008

Wang, Q., Maze, B., Vahedi Tafreshi, H., & Pourdeyhimi, B. (2007). On the pressure drop modeling of monofilament-woven fabrics. *Chemical Engineering Science*, *62*(17), 4817–4821. doi:10.1016/j.ces.2007.06.001

Wong, C. C., Long, A. C., Sherburn, M., Robitaille, F., Harrison, P., & Rudd, C. D. (2006). Comparisons of novel and efficient approaches for permeability prediction based on the fabric architecture. *Composites Part A: Applied Science and Manufacturing*, *37*(6), 847–857. doi:10.1016/j.compositesa.2005.01.020

Annexes

Annex 1 – Meshing parameters

A set of meshing parameters is defined in the following figure. These parameters are of two types: number of elements (*n*) and bias factor (*B*).

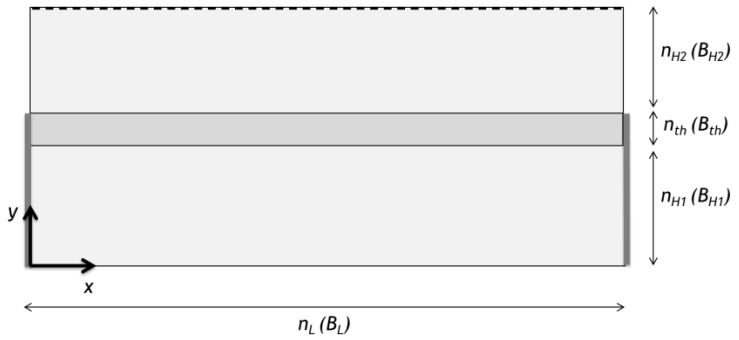

Figure A.1 – Correspondence between meshing parameters and geometry.

The following table presents values for each particular meshing parameter according to each mesh used in grid sensitivity tests (*AR* = 4).

Table A.1 – Meshing parameters[11] for the present configuration, *AR* = 4 and H_2 = 0.05 m.

Parameter	Mesh 1	Mesh 2	Mesh 3	Mesh 4
n_L B_L (bias type)	200 10 (_ _ ___ _ _)	400 10 (_ _ ___ _ _)	800 10 (_ _ ___ _ _)	1600 10 (_ _ ___ _ _)
n_{H1} B_{H1} (bias type)	60 10 (_ _ ___ _ _)	120 10 (_ _ ___ _ _)	240 10 (_ _ ___ _ _)	480 10 (_ _ ___ _ _)
n_{th} B_{th} (bias type)	5 0 (N/A)	10 0 (N/A)	20 0 (N/A)	40 0 (N/A)
n_{H2} B_{H2} (bias type)	50 10 (_ _ ___)	100 10 (_ _ ___)	200 10 (_ _ ___)	400 10 (_ _ ___)
Total number of elements, *n*	23,000	92,000	368,000	1,472,000

For cases with *AR* = 12, meshes of Table A.1 were altered by increasing the number of elements in proportion to geometrical changes (i.e. n_L was tripled).

The low-*x*/low-*y* corners of the resulting meshes are represented in the following figure, in which the fabric (domain B) can be identified as a region with higher density of grid cells (close to the top of each subset).

[11] These are given for *AR* = 4, which means that for other aspect ratios, the values of n_L had to be proportionally altered (thrice those present, in the case of *AR* = 12). However, these parameters remained unchanged when the height of the enclosure was decrease from 52 mm to 25 or 8 mm.

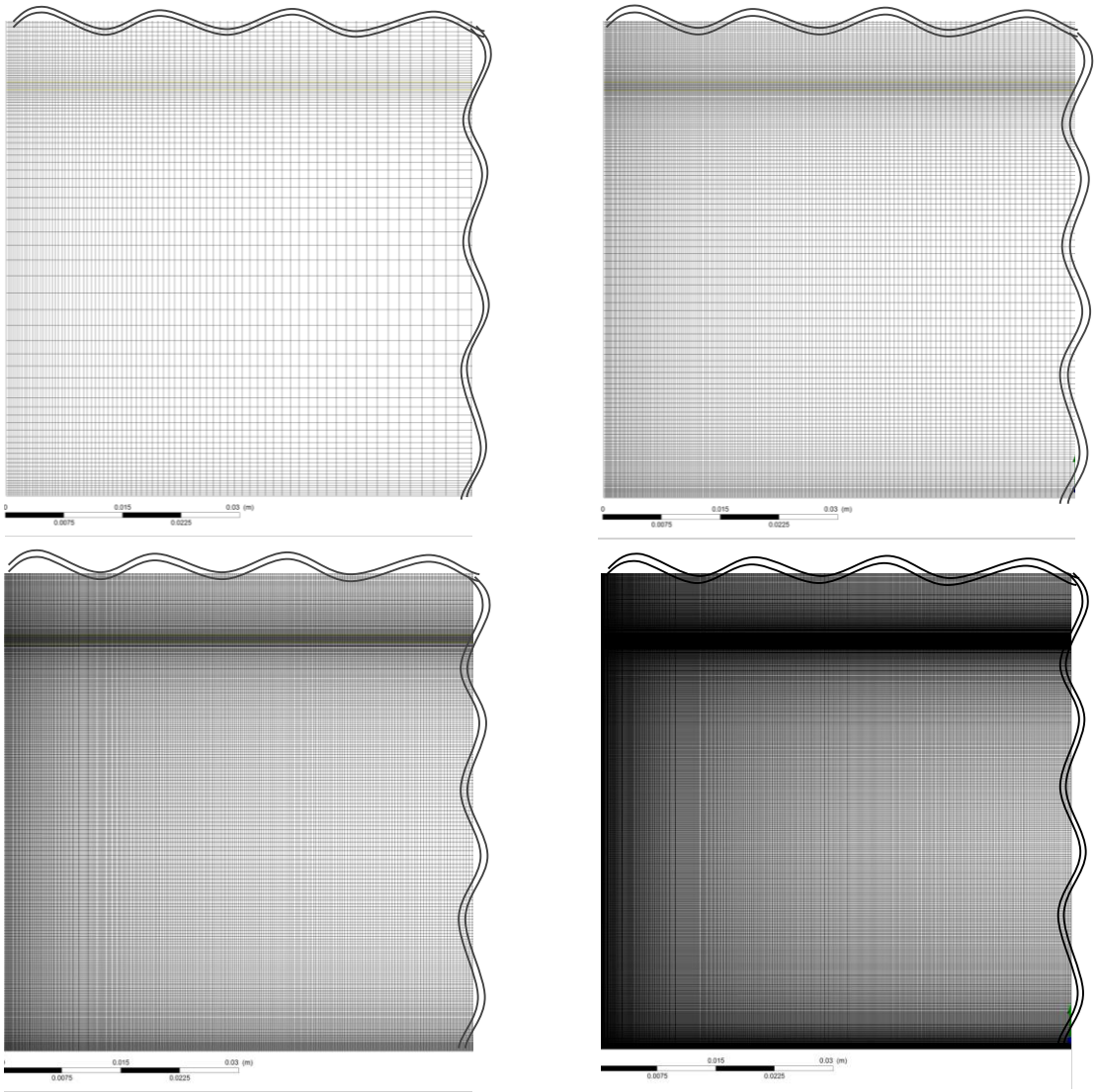

Figure A.2 - Tested meshes: left-to-right and top-to-bottom, mesh 1 through mesh 4. Only the low-*x*/low-*y* corner is represented. Total scale bar length is 0.03 m.

For the purpose of validating the height of the external domain, H_2, meshes were extended by simply adding a new meshing zone on the top, with a number of elements in *y*-direction that was proportional to the added length (half of the proportion corresponding to n_{H2} of Table A.1, given for H_2 = 0.05 m, was used, resulting in an added region with a less dense grid).

Annex 2 – Labelling of simulation cases

The significant amount of simulation cases presented in this study called for a systematic labelling procedure. The correspondence between each label and its respective set of conditions is given in the following table.

Table A.2 – Labelling correspondence for all simulations of this study (continues on the following page).

Label	u_{in} [m s^{-1}]	θ [º]	AR [-]	L_1 [m]	H_1 [m]	H_2 [m]	k_s [W m^{-1} K^{-1}]	$\varepsilon_{inner\ fabric}$ [-]
AR_4_Teta_-120_epsilon_05	0.5	-120	4	0.208	0.052	0.050	0.095240	0.05
AR_4_Teta_-120_epsilon_95	0.5	-120	4	0.208	0.052	0.050	0.095240	0.95
AR_4_Teta_-90_epsilon_05	0.5	-90	4	0.208	0.052	0.050	0.095240	0.05
AR_4_Teta_-90_epsilon_95	0.5	-90	4	0.208	0.052	0.050	0.095240	0.95
AR_4_Teta_-80_epsilon_05	0.5	-80	4	0.208	0.052	0.050	0.095240	0.05
AR_4_Teta_-80_epsilon_95	0.5	-80	4	0.208	0.052	0.050	0.095240	0.95
AR_4_Teta_-70_epsilon_05	0.5	-70	4	0.208	0.052	0.050	0.095240	0.05
AR_4_Teta_-70_epsilon_95	0.5	-70	4	0.208	0.052	0.050	0.095240	0.95
AR_4_Teta_-60_epsilon_05	0.5	-60	4	0.208	0.052	0.050	0.095240	0.05
AR_4_Teta_-60_epsilon_95	0.5	-60	4	0.208	0.052	0.050	0.095240	0.95
AR_4_Teta_-50_epsilon_05	0.5	-50	4	0.208	0.052	0.050	0.095240	0.05
AR_4_Teta_-50_epsilon_95	0.5	-50	4	0.208	0.052	0.050	0.095240	0.95
AR_4_Teta_-40_epsilon_05	0.5	-40	4	0.208	0.052	0.050	0.095240	0.05
AR_4_Teta_-40_epsilon_95	0.5	-40	4	0.208	0.052	0.050	0.095240	0.95
AR_4_Teta_-30_epsilon_05	0.5	-30	4	0.208	0.052	0.050	0.095240	0.05
AR_4_Teta_-30_epsilon_95	0.5	-30	4	0.208	0.052	0.050	0.095240	0.95
AR_4_Teta_-20_epsilon_05	0.5	-20	4	0.208	0.052	0.050	0.095240	0.05
AR_4_Teta_-20_epsilon_95	0.5	-20	4	0.208	0.052	0.050	0.095240	0.95
AR_4_Teta_-10_epsilon_05	0.5	-10	4	0.208	0.052	0.050	0.095240	0.05
AR_4_Teta_-10_epsilon_95	0.5	-10	4	0.208	0.052	0.050	0.095240	0.95
AR_4_Teta_-9_epsilon_05	0.5	-9	4	0.208	0.052	0.050	0.095240	0.05
AR_4_Teta_-9_epsilon_95	0.5	-9	4	0.208	0.052	0.050	0.095240	0.95
AR_4_Teta_-8_epsilon_05	0.5	-8	4	0.208	0.052	0.050	0.095240	0.05
AR_4_Teta_-8_epsilon_95	0.5	-8	4	0.208	0.052	0.050	0.095240	0.95
AR_4_Teta_-7_epsilon_05	0.5	-7	4	0.208	0.052	0.050	0.095240	0.05
AR_4_Teta_-7_epsilon_95	0.5	-7	4	0.208	0.052	0.050	0.095240	0.95
AR_4_Teta_-6_epsilon_05	0.5	-6	4	0.208	0.052	0.050	0.095240	0.05
AR_4_Teta_-6_epsilon_95	0.5	-6	4	0.208	0.052	0.050	0.095240	0.95
AR_4_Teta_-5_epsilon_05	0.5	-5	4	0.208	0.052	0.050	0.095240	0.05
AR_4_Teta_-5_epsilon_95	0.5	-5	4	0.208	0.052	0.050	0.095240	0.95
AR_4_Teta_0_epsilon_05	0.5	0	4	0.208	0.052	0.050	0.095240	0.05
AR_4_Teta_0_epsilon_95	0.5	0	4	0.208	0.052	0.050	0.095240	0.95
AR_4_Teta_5_epsilon_05	0.5	5	4	0.208	0.052	0.050	0.095240	0.05
AR_4_Teta_5_epsilon_95	0.5	5	4	0.208	0.052	0.050	0.095240	0.95
AR_4_Teta_10_epsilon_05	0.5	10	4	0.208	0.052	0.050	0.095240	0.05
AR_4_Teta_10_epsilon_95	0.5	10	4	0.208	0.052	0.050	0.095240	0.95
AR_4_Teta_20_epsilon_05	0.5	20	4	0.208	0.052	0.050	0.095240	0.05
AR_4_Teta_20_epsilon_95	0.5	20	4	0.208	0.052	0.050	0.095240	0.95

Table A.2 – (continued)

Label	u_{in} [m s^{-1}]	θ [º]	AR [-]	L_1 [m]	H_1 [m]	H_2 [m]	k_s [W m^{-1} K^{-1}]	$\varepsilon_{inner\ fabric}$ [-]
AR_4_Teta_30_epsilon_05	0.5	30	4	0.208	0.052	0.050	0.095240	0.05
AR_4_Teta_30_epsilon_95	0.5	30	4	0.208	0.052	0.050	0.095240	0.95
AR_4_Teta_40_epsilon_05	0.5	40	4	0.208	0.052	0.050	0.095240	0.05
AR_4_Teta_40_epsilon_95	0.5	40	4	0.208	0.052	0.050	0.095240	0.95
AR_4_Teta_50_epsilon_05	0.5	50	4	0.208	0.052	0.050	0.095240	0.05
AR_4_Teta_50_epsilon_95	0.5	50	4	0.208	0.052	0.050	0.095240	0.95
AR_4_Teta_60_epsilon_05	0.5	60	4	0.208	0.052	0.050	0.095240	0.05
AR_4_Teta_60_epsilon_95	0.5	60	4	0.208	0.052	0.050	0.095240	0.95
AR_4_Teta_70_epsilon_05	0.5	70	4	0.208	0.052	0.050	0.095240	0.05
AR_4_Teta_70_epsilon_95	0.5	70	4	0.208	0.052	0.050	0.095240	0.95
AR_4_Teta_80_epsilon_05	0.5	80	4	0.208	0.052	0.050	0.095240	0.05
AR_4_Teta_80_epsilon_95	0.5	80	4	0.208	0.052	0.050	0.095240	0.95
AR_4_Teta_90_epsilon_05	0.5	90	4	0.208	0.052	0.050	0.095240	0.05
AR_4_Teta_90_epsilon_95	0.5	90	4	0.208	0.052	0.050	0.095240	0.95
AR_4_Teta_120_epsilon_05	0.5	120	4	0.208	0.052	0.050	0.095240	0.05
AR_4_Teta_120_epsilon_95	0.5	120	4	0.208	0.052	0.050	0.095240	0.95
AR_4_Teta_180_epsilon_05	0.5	180	4	0.208	0.052	0.050	0.095240	0.05
AR_4_Teta_180_epsilon_95	0.5	180	4	0.208	0.052	0.050	0.095240	0.95
AR_4_Teta_0_H1_0008_epsilon_05	0.5	0	4	0.032	0.008	0.050	0.095240	0.05
AR_4_Teta_0_H1_0008_epsilon_95	0.5	0	4	0.032	0.008	0.050	0.095240	0.95
AR_4_Teta_90_H1_0008_epsilon_05	0.5	90	4	0.032	0.008	0.050	0.095240	0.05
AR_4_Teta_90_H1_0008_epsilon_95	0.5	90	4	0.032	0.008	0.050	0.095240	0.95
AR_4_Teta_0_H1_0025_epsilon_05	0.5	0	4	0.100	0.025	0.050	0.095240	0.05
AR_4_Teta_0_H1_0025_epsilon_95	0.5	0	4	0.100	0.025	0.050	0.095240	0.95
AR_4_Teta_90_H1_0025_epsilon_05	0.5	90	4	0.100	0.025	0.050	0.095240	0.05
AR_4_Teta_90_H1_0025_epsilon_95	0.5	90	4	0.100	0.025	0.050	0.095240	0.95
AR_4_Teta_0_U_3_epsilon_05	3.0	0	4	0.208	0.052	0.050	0.095240	0.05
AR_4_Teta_0_U_3_epsilon_95	3.0	0	4	0.208	0.052	0.050	0.095240	0.95
AR_4_Teta_90_U_3_epsilon_05	3.0	90	4	0.208	0.052	0.050	0.095240	0.05
AR_4_Teta_90_U_3_epsilon_95	3.0	90	4	0.208	0.052	0.050	0.095240	0.95
AR_4_Teta_0_epsilon_05_k/10	0.5	0	4	0.208	0.052	0.050	0.009524	0.05
AR_4_Teta_0_epsilon_95_k/10	0.5	0	4	0.208	0.052	0.050	0.009524	0.95
AR_4_Teta_90_epsilon_05_k/10	0.5	90	4	0.208	0.052	0.050	0.009524	0.05
AR_4_Teta_90_epsilon_95_k/10	0.5	90	4	0.208	0.052	0.050	0.009524	0.95

Annex 3 – Mass and Energy Balances

In this section, mass and energy balances are presented for each case of this study (please refer to Annex 2 – Labelling of simulation cases). In the entire set of simulations, absolute values of mass imbalance were always inferior to 10^{-5}, whereas absolute values of energy imbalance varied from 0.00003% ([12]) to 0.8% ([13]). For the formulae used in calculating mass and energy imbalances, please refer to Annex 6 – *Mathematical formulae*.

Table A.3 – Mass balances for each case presented in this study (mesh 3).
(continued on the following page)

Case	Area Integral of Velocity *u* [$m^3\ s^{-1}$]		% imbalance
	at inlet	at outlet	
AR_4_Teta_-120_epsilon_05	0.025	0.025	< $1x10^{-6}$
AR_4_Teta_-120_epsilon_95	0.025	0.025	< $1x10^{-6}$
AR_4_Teta_-90_epsilon_05	0.025	0.025	< $1x10^{-6}$
AR_4_Teta_-90_epsilon_95	0.025	0.025	< $1x10^{-6}$
AR_4_Teta_-80_epsilon_05	0.025	0.025	< $1x10^{-6}$
AR_4_Teta_-80_epsilon_95	0.025	0.025	< $1x10^{-6}$
AR_4_Teta_-70_epsilon_05	0.025	0.025	< $1x10^{-6}$
AR_4_Teta_-70_epsilon_95	0.025	0.025	< $1x10^{-6}$
AR_4_Teta_-60_epsilon_05	0.025	0.025	< $1x10^{-6}$
AR_4_Teta_-60_epsilon_95	0.025	0.025	< $1x10^{-6}$
AR_4_Teta_-50_epsilon_05	0.025	0.025	< $1x10^{-6}$
AR_4_Teta_-50_epsilon_95	0.025	0.025	< $1x10^{-6}$
AR_4_Teta_-40_epsilon_05	0.025	0.025	< $1x10^{-6}$
AR_4_Teta_-40_epsilon_95	0.025	0.025	< $1x10^{-6}$
AR_4_Teta_-30_epsilon_05	0.025	0.025	< $1x10^{-6}$
AR_4_Teta_-30_epsilon_95	0.025	0.025	< $1x10^{-6}$
AR_4_Teta_-20_epsilon_05	0.025	0.025	< $1x10^{-6}$
AR_4_Teta_-20_epsilon_95	0.025	0.025	$7.451x10^{-6}$
AR_4_Teta_-10_epsilon_05	0.025	0.025	$7.451x10^{-6}$
AR_4_Teta_-10_epsilon_95	0.025	0.025	< $1x10^{-6}$
AR_4_Teta_-9_epsilon_05	0.025	0.025	$7.451x10^{-6}$
AR_4_Teta_-9_epsilon_95	0.025	0.025	< $1x10^{-6}$

[12] AR_4_Teta_0_H1_0025_epsilon_05
[13] AR_4_Teta_180_epsilon_05

Table A.3 – (continued)

Case	Area Integral of Velocity *u* [$m^3 s^{-1}$]		% imbalance
	at inlet	at outlet	
AR_4_Teta_-8_epsilon_05	0.025	0.025	< $1x10^{-6}$
AR_4_Teta_-8_epsilon_95	0.025	0.025	< $1x10^{-6}$
AR_4_Teta_-7_epsilon_05	0.025	0.025	< $1x10^{-6}$
AR_4_Teta_-7_epsilon_95	0.025	0.025	< $1x10^{-6}$
AR_4_Teta_-6_epsilon_05	0.025	0.025	< $1x10^{-6}$
AR_4_Teta_-6_epsilon_95	0.025	0.025	< $1x10^{-6}$
AR_4_Teta_-5_epsilon_05	0.025	0.025	< $1x10^{-6}$
AR_4_Teta_-5_epsilon_95	0.025	0.025	< $1x10^{-6}$
AR_4_Teta_0_epsilon_05	0.025	0.025	< $1x10^{-6}$
AR_4_Teta_0_epsilon_95	0.025	0.025	< $1x10^{-6}$
AR_4_Teta_5_epsilon_05	0.025	0.025	< $1x10^{-6}$
AR_4_Teta_5_epsilon_95	0.025	0.025	< $1x10^{-6}$
AR_4_Teta_6_epsilon_05	0.025	0.025	< $1x10^{-6}$
AR_4_Teta_6_epsilon_95	0.025	0.025	< $1x10^{-6}$
AR_4_Teta_7_epsilon_05	0.025	0.025	< $1x10^{-6}$
AR_4_Teta_7_epsilon_95	0.025	0.025	$7x10^{-6}$
AR_4_Teta_8_epsilon_05	0.025	0.025	< $1x10^{-6}$
AR_4_Teta_8_epsilon_95	0.025	0.025	< $1x10^{-6}$
AR_4_Teta_9_epsilon_05	0.025	0.025	< $1x10^{-6}$
AR_4_Teta_9_epsilon_95	0.025	0.025	< $1x10^{-6}$
AR_4_Teta_10_epsilon_05	0.025	0.025	< $1x10^{-6}$
AR_4_Teta_10_epsilon_95	0.025	0.025	< $1x10^{-6}$
AR_4_Teta_20_epsilon_05	0.025	0.025	< $1x10^{-6}$
AR_4_Teta_20_epsilon_95	0.025	0.025	< $1x10^{-6}$
AR_4_Teta_30_epsilon_05	0.025	0.025	< $1x10^{-6}$
AR_4_Teta_30_epsilon_95	0.025	0.025	< $1x10^{-6}$
AR_4_Teta_40_epsilon_05	0.025	0.025	< $1x10^{-6}$
AR_4_Teta_40_epsilon_95	0.025	0.025	< $1x10^{-6}$
AR_4_Teta_50_epsilon_05	0.025	0.025	< $1x10^{-6}$
AR_4_Teta_50_epsilon_95	0.025	0.025	< $1x10^{-6}$
AR_4_Teta_60_epsilon_05	0.025	0.025	< $1x10^{-6}$
AR_4_Teta_60_epsilon_95	0.025	0.025	< $1x10^{-6}$
AR_4_Teta_70_epsilon_05	0.025	0.025	< $1x10^{-6}$
AR_4_Teta_70_epsilon_95	0.025	0.025	< $1x10^{-6}$
AR_4_Teta_80_epsilon_05	0.025	0.025	< $1x10^{-6}$
AR_4_Teta_80_epsilon_95	0.025	0.025	< $1x10^{-6}$
AR_4_Teta_90_epsilon_05	0.025	0.025	< $1x10^{-6}$
AR_4_Teta_90_epsilon_95	0.025	0.025	< $1x10^{-6}$

Table A.3 – (continued)

Case	Area Integral of Velocity *u* [$m^3 s^{-1}$]		% imbalance
	at inlet	at outlet	
AR_4_Teta_120_epsilon_05	0.025	0.025	< $1x10^{-6}$
AR_4_Teta_120_epsilon_95	0.025	0.025	< $1x10^{-6}$
AR_4_Teta_180_epsilon_05	0.025	0.025	$7x10^{-6}$
AR_4_Teta_180_epsilon_95	0.025	0.025	< $1x10^{-6}$
AR_4_Teta_0_H1_0008_epsilon_05	0.025	0.025	< $1x10^{-6}$
AR_4_Teta_0_H1_0008_epsilon_95	0.025	0.025	< $1x10^{-6}$
AR_4_Teta_90_H1_0008_epsilon_05	0.025	0.025	< $1x10^{-6}$
AR_4_Teta_90_H1_0008_epsilon_95	0.025	0.025	$7x10^{-6}$
AR_4_Teta_0_H1_0025_epsilon_05	0.025	0.025	< $1x10^{-6}$
AR_4_Teta_0_H1_0025_epsilon_95	0.025	0.025	< $1x10^{-6}$
AR_4_Teta_90_H1_0025_epsilon_05	0.025	0.025	< $1x10^{-6}$
AR_4_Teta_90_H1_0025_epsilon_95	0.025	0.025	< $1x10^{-6}$
AR_4_Teta_0_U_3_epsilon_05	0.15	0.15	$9.9x10^{-6}$
AR_4_Teta_0_U_3_epsilon_95	0.15	0.15	$9.9x10^{-6}$
AR_4_Teta_90_U_3_epsilon_05	0.15	0.15	$9.9x10^{-6}$
AR_4_Teta_90_U_3_epsilon_95	0.15	0.15	$9.9x10^{-6}$
AR_4_Teta_0_epsilon_05_k/10	0.025	0.025	< $1x10^{-6}$
AR_4_Teta_0_epsilon_95_k/10	0.025	0.025	< $1x10^{-6}$

Table A.4 - Energy balances for each case presented in this study (mesh 3), along with Rayleigh number.

Case	Area Integral of Boundary Heat Flux Sensible [W] at:		Area Integral of Heat flux [W] at:		% imbalance	*Ra* [-]
	at inlet	at outlet	boundary 9	boundary 1		
AR_4_Teta_-120_epsilon_05	-449.884	441.844	-3.132	11.173	-0.0008	2.91E+05
AR_4_Teta_-120_epsilon_95	-450.320	434.477	-6.706	22.548	-0.0019	2.13E+05
AR_4_Teta_-90_epsilon_05	-449.940	441.126	-3.463	12.281	0.0315	2.83E+05
AR_4_Teta_-90_epsilon_95	-450.361	433.978	-6.893	23.276	-0.0007	2.09E+05
AR_4_Teta_-80_epsilon_05	-449.949	441.039	-3.510	12.403	-0.1299	2.82E+05
AR_4_Teta_-80_epsilon_95	-450.367	433.931	-6.916	23.352	-0.0006	2.08E+05
AR_4_Teta_-70_epsilon_05	-449.954	441.017	-3.529	12.467	-0.0010	2.82E+05
AR_4_Teta_-70_epsilon_95	-450.372	433.923	-6.930	23.378	-0.0006	2.08E+05
AR_4_Teta_-60_epsilon_05	-449.958	441.049	-3.526	12.435	-0.0007	2.82E+05
AR_4_Teta_-60_epsilon_95	-450.374	433.953	-6.935	23.357	-0.0007	2.08E+05
AR_4_Teta_-50_epsilon_05	-449.959	441.138	-3.500	12.302	-0.1580	2.83E+05
AR_4_Teta_-50_epsilon_95	-450.376	434.020	-6.929	23.285	-0.0007	2.08E+05
AR_4_Teta_-40_epsilon_05	-449.956	441.291	-3.441	12.100	-0.0475	2.84E+05
AR_4_Teta_-40_epsilon_95	-450.375	434.126	-6.911	23.160	-0.0007	2.09E+05
AR_4_Teta_-30_epsilon_05	-449.951	441.497	-3.355	11.778	-0.2629	2.86E+05
AR_4_Teta_-30_epsilon_95	-450.373	434.270	-6.878	22.981	-0.0005	2.09E+05
AR_4_Teta_-20_epsilon_05	-449.938	441.765	-3.227	11.401	-0.0005	2.89E+05
AR_4_Teta_-20_epsilon_95	-450.367	434.441	-6.832	22.758	-0.0007	2.10E+05
AR_4_Teta_-10_epsilon_05	-449.920	442.059	-3.083	10.944	-0.0004	2.92E+05
AR_4_Teta_-10_epsilon_95	-450.357	434.648	-6.772	22.481	-0.0007	2.12E+05
AR_4_Teta_-9_epsilon_05	-449.917	442.095	-3.065	10.887	-0.0005	2.92E+05
AR_4_Teta_-9_epsilon_95	-450.355	434.673	-6.764	22.447	-0.0006	2.12E+05
AR_4_Teta_-8_epsilon_05	-449.915	442.135	-3.046	10.826	-0.0005	2.93E+05
AR_4_Teta_-8_epsilon_95	-450.354	434.699	-6.756	22.411	-0.0007	2.12E+05
AR_4_Teta_-7_epsilon_05	-449.912	442.177	-3.026	10.762	-0.0005	2.93E+05
AR_4_Teta_-7_epsilon_95	-450.353	434.727	-6.748	22.374	-0.0005	2.12E+05
AR_4_Teta_-6_epsilon_05	-449.910	442.222	-3.005	10.692	-0.0005	2.93E+05
AR_4_Teta_-6_epsilon_95	-450.351	434.756	-6.738	22.334	-0.0007	2.12E+05
AR_4_Teta_-5_epsilon_05	-450.002	440.927	-3.947	13.022	-0.0003	2.75E+05
AR_4_Teta_-5_epsilon_95	-450.393	434.197	-7.188	23.385	-0.0005	2.04E+05
AR_4_Teta_0_epsilon_05	-450.082	440.713	-4.037	13.406	-0.0004	2.72E+05
AR_4_Teta_0_epsilon_95	-450.430	434.160	-7.220	23.490	-0.0006	2.03E+05
AR_4_Teta_5_epsilon_05	-450.096	440.778	-4.046	13.365	-0.0003	2.72E+05
AR_4_Teta_5_epsilon_95	-450.442	434.457	-7.209	23.194	-0.0006	2.04E+05
AR_4_Teta_6_epsilon_05	-450.102	441.184	-3.991	12.909	-0.0003	2.74E+05
AR_4_Teta_6_epsilon_95	-450.444	434.458	-7.215	23.201	-0.0005	2.04E+05
AR_4_Teta_7_epsilon_05	-450.113	442.989	-3.218	10.343	-0.0003	2.90E+05
AR_4_Teta_7_epsilon_95	-450.446	434.459	-7.221	23.209	-0.0004	2.03E+05

Table A.4 – (continued)

Case	Area Integral of Boundary Heat Flux Sensible [W] at:		Area Integral of Heat flux [W] at:		% imbalance	*Ra* [-]
	at inlet	at outlet	boundary 9	boundary 1		
AR_4_Teta_8_epsilon_05	-450.115	442.947	-3.237	10.406	-0.0002	2.90E+05
AR_4_Teta_8_epsilon_95	-450.448	434.460	-7.227	23.215	-0.0005	2.03E+05
AR_4_Teta_9_epsilon_05	-450.117	442.907	-3.255	10.465	-0.0001	2.90E+05
AR_4_Teta_9_epsilon_95	-450.459	435.341	-6.796	21.914	-0.0005	2.12E+05
AR_4_Teta_10_epsilon_05	-450.119	442.871	-3.272	10.521	-0.0004	2.89E+05
AR_4_Teta_10_epsilon_95	-450.461	435.326	-6.807	21.943	-0.0005	2.12E+05
AR_4_Teta_20_epsilon_05	-450.476	435.236	-6.899	22.139	-0.0005	2.86E+05
AR_4_Teta_20_epsilon_95	-450.476	435.236	-6.899	22.139	-0.0005	2.10E+05
AR_4_Teta_30_epsilon_05	-450.143	442.388	-3.513	11.268	-0.0002	2.84E+05
AR_4_Teta_30_epsilon_95	-450.486	435.201	-6.969	22.254	-0.0006	2.08E+05
AR_4_Teta_40_epsilon_05	-450.155	442.228	-3.608	11.535	-0.0008	2.82E+05
AR_4_Teta_40_epsilon_95	-450.494	435.192	-7.030	22.331	-0.0010	2.07E+05
AR_4_Teta_50_epsilon_05	-450.166	442.124	-3.676	11.718	-0.0007	2.80E+05
AR_4_Teta_50_epsilon_95	-450.501	435.203	-7.080	22.378	-0.0011	2.06E+05
AR_4_Teta_60_epsilon_05	-450.174	442.072	-3.720	11.822	-0.0011	2.79E+05
AR_4_Teta_60_epsilon_95	-450.507	435.230	-7.116	22.393	-0.0017	2.05E+05
AR_4_Teta_70_epsilon_05	-450.180	442.065	-3.738	11.852	-0.0014	2.79E+05
AR_4_Teta_70_epsilon_95	-450.511	435.270	-7.138	22.379	-0.0018	2.05E+05
AR_4_Teta_80_epsilon_05	-450.183	442.102	-3.732	11.813	-0.0015	2.79E+05
AR_4_Teta_80_epsilon_95	-450.513	435.318	-7.145	22.339	-0.0017	2.05E+05
AR_4_Teta_90_epsilon_05	-450.183	442.185	-3.701	11.699	-0.0020	2.80E+05
AR_4_Teta_90_epsilon_95	-450.513	435.374	-7.135	22.274	-0.0019	2.05E+05
AR_4_Teta_120_epsilon_05	-450.165	442.826	-3.423	10.761	-0.0035	2.86E+05
AR_4_Teta_120_epsilon_95	-450.500	435.608	-6.986	21.877	-0.0016	2.08E+05
AR_4_Teta_180_epsilon_05	-449.801	446.997	-1.189	3.962	-0.7871	3.36E+05
AR_4_Teta_180_epsilon_95	-450.286	437.165	-5.846	18.999	0.1651	2.32E+05
AR_4_Teta_0_H1_0008_epsilon_05	-449.846	447.511	-0.132	2.467	0.0469	1.11E+03
AR_4_Teta_0_H1_0008_epsilon_95	-450.002	445.561	-0.257	4.699	0.0414	9.09E+02
AR_4_Teta_90_H1_0008_epsilon_05	-449.879	447.381	-0.147	2.645	0.0244	1.09E+03
AR_4_Teta_90_H1_0008_epsilon_95	-450.020	445.552	-0.264	4.735	0.0543	8.99E+02
AR_4_Teta_0_H1_0025_epsilon_05	-450.057	443.699	-1.414	7.772	0.00003	3.06E+04
AR_4_Teta_0_H1_0025_epsilon_95	-450.334	439.797	-2.411	12.947	-0.0002	2.40E+04
AR_4_Teta_90_H1_0025_epsilon_05	-450.100	444.661	-1.297	6.736	0.0002	3.15E+04
AR_4_Teta_90_H1_0025_epsilon_95	-450.371	440.502	-2.353	12.223	-0.0008	2.44E+04
AR_4_Teta_0_U_3_epsilon_05	-2698.320	2685.490	-2.456	15.284	0.0003	3.02E+05
AR_4_Teta_0_U_3_epsilon_95	-2698.530	2674.350	-4.764	28.943	-0.0006	2.47E+05
AR_4_Teta_90_U_3_epsilon_05	-2698.360	2687.460	-2.221	13.128	0.0193	3.09E+05
AR_4_Teta_90_U_3_epsilon_95	-2698.570	2675.670	-4.586	27.490	-0.0004	2.51E+05
AR_4_Teta_0_epsilon_05_k/10	-449.990	442.547	-3.192	10.634	-0.0002	2.23E+05
AR_4_Teta_0_epsilon_95_k/10	-450.183	438.636	-5.028	16.575	-0.0005	1.45E+05

Annex 4 – Validation of distance H_2

In order to choose the adequate height of the external domain, H_2, the value of 5 cm, previously used by Couto & Mayor (2013), was increased up to 20 cm. Results are next compared for the lowest inlet velocity[14] (u_{in} = 0.5 m s^{-1}), horizontal setups (θ = 0º) and AR = 4 (at $\varepsilon_{inner\ fabric}$ = 0.05 and 0.95), as well as AR = 12 (only for $\varepsilon_{inner\ fabric}$ = 0.05). For this purpose, mesh 3, which was regarded as giving grid-independent results (*Annex 8 - Grid sensitivity tests*), was extended by adding a new meshing zone on the top, with a number of elements in *y*-direction which was proportional to the added length (half of the proportion corresponding to n_{H2} of Table A.1, which corresponds to H_2 = 0.05 m, was used, resulting in an added region with a less dense grid).

In Table A.5, mass and energy imbalances are presented for each case (for the formulae used in calculating mass and energy imbalances, please refer to Annex 6 – *Mathematical formulae*). Maximum imbalances for mass and energy correspond to 0.51% and 0.0004%, respectively. Mass imbalances are seen to increase with H_2, probably due to the lower-density meshing region that was added to the external domain. Still, these imbalances are relatively low.

Average *Nu* and maximum velocity components in the enclosure are given in Table A.6. Local temperature and total heat transfer coefficient along the top of the fabric are given in Figure A.3, for AR = 4, and Figure A.5, for AR = 12. Velocity magnitude and temperature profiles in the external domain are given in Figure A.4, for AR = 4, and Figure A.6, for AR = 12.

[14] Lower inlet velocity means thicker external boundary layers. Thus, conclusions drawn here should also apply for higher inlet velocities.

Table A.5 – Mass and energy imbalances for each tested value of H_2 (0.05, 0.10 and 0.15 m). Both cases of AR = 4 and 12 were considered, at different values of $\varepsilon_{inner\ fabric}$ (0.05 and 0.95), inlet velocity u_{in} = 0.5 m s^{-1} and air gap thickness H_1 = 52 mm (mesh 3, serial processing).

	Mass imbalance [%]	Energy imbalance [%]			
		Enclosure	Fabric	Exterior	Global
AR_4_Teta_ 0_epsilon_05					
H2 = 0.05 m	-2.8E-02	9.2E-05	0.0E+00	-4.7E-04	-3.8E-04
H2 = 0.10 m	-1.1E-01	7.1E-05	7.0E-06	1.4E-04	2.2E-04
AR_4_Teta_ 0_epsilon_95					
H2 = 0.05 m	-2.6E-02	-9.7E-05	-2.4E-05	-4.8E-04	-6.0E-04
H2 = 0.10 m	-1.1E-01	-1.1E-04	-3.2E-05	5.9E-05	-7.9E-05
AR_12_Teta_ 0_epsilon_05					
H_2 = 0.05 m	-3.6E-02	8.3E-05	0.0E+00	1.3E-04	2.1E-04
H_2 = 0.10 m	-1.4E-01	1.1E-04	0.0E+00	-4.8E-04	-3.7E-04
H_2 = 0.15 m	-3.0E-01	9.1E-05	0.0E+00	-5.6E-05	3.6E-05
H_2 = 0.20 m	-5.1E-01	8.1E-05	1.0E-05	-2.6E-04	-1.7E-04

Table A.6 – Average Nu_{total} and maximum velocity components for each tested value of H_2 (0.05 and 0.10 m). Both cases of AR = 4 and 12 were considered, at constant inlet velocity u_{in} = 0.5 m s^{-1} and air gap thickness H_1 = 52 mm (mesh 3, serial processing). Figures between brackets correspond to absolute percentage difference relative to the results obtained with the highest H_2.

	Nu_{total} (on skin) [-]	Diff. [%]	u_{max} (enclosure) [m s^{-1}]	Diff. [%]	v_{max} (enclosure) [m s^{-1}]	Diff. [%]
AR_4_Teta_ 0_epsilon_05						
H_2 = 0.05 m	6.6437	(0.03)	0.097	(0.00)	0.104	(0.00)
H_2 = 0.10 m	6.6418	-	0.097	-	0.104	-
AR_4_Teta_90_epsilon_05						
H_2 = 0.05 m	15.5930	(0.03)	0.082	(0.00)	0.086	(0.00)
H_2 = 0.10 m	15.5881	-	0.082	-	0.086	-
AR_12_Teta_ 0_epsilon_05						
H_2 = 0.05 m	6.5059	(3.80)	0.101	(0.00)	0.098	(6.67)
H_2 = 0.10 m	6.8339	(1.05)	0.102	(0.99)	0.107	(1.90)
H_2 = 0.15 m	6.7619	(0.02)	0.101	(0.00)	0.104	(0.95)
H_2 = 0.20 m	6.7630	-	0.101	-	0.105	-

For AR = 4, Nu and maximum velocity components in the enclosure are nearly independent from H_2 already for a height of 5 cm (Table A.6). In addition to this, local temperature profiles and total heat transfer coefficient along the top of the fabric are practically overlapping for different values of H_2 (Figure A.3). Finally, velocity profiles in the external domain are also very similar (Figure A.4), especially regarding the thicknesses of boundary layers for flow and temperature. Therefore, results for AR = 4 are regarded as H_2-independent, supporting the use of H_2 = 0.05 m for this aspect ratio.

However, for AR = 12, a higher value of H_2 is necessary in order to obtain H_2–independent results. As can be seen in Table A.6, differences in Nu_{total} and maximum velocities are non-significant (relative difference inferior to 1%) only between H_2 = 0.15 and 0.20 m. Temperature and h_{total} profiles along the fabric vary quite significantly for $H_2 \leq 0.15$ (Figure A.5), with differences in external velocity and temperature profiles for the same interval of H_2 values (Figure A.6). Therefore, results for AR = 12 are regarded as H_2-independent for H_2 = 0.15 m.

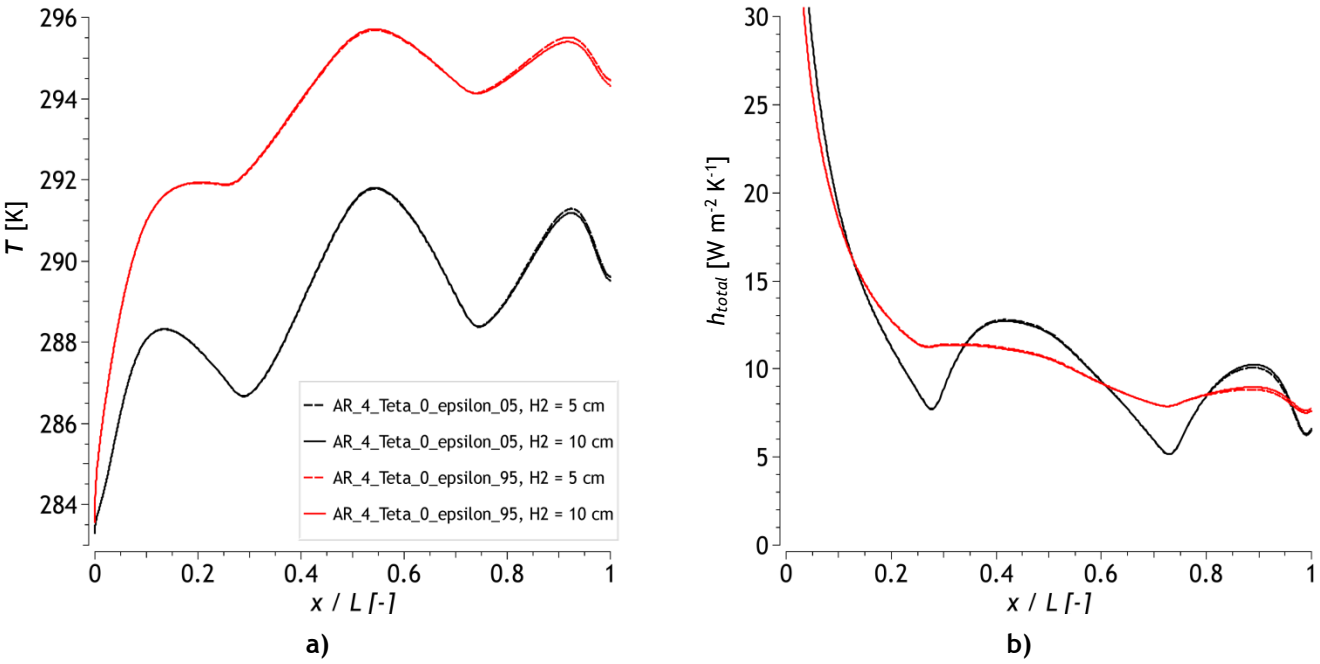

Figure A.3 - Local temperature and local heat transfer coefficient profiles along boundary 7 (top of the fabric) for *AR* = 4 and for each tested value of H_2 (0.05 and 0.10 m): a) temperature profiles; **b)** total heat transfer coefficient profiles. Two different values of $\varepsilon_{inner\ fabric}$ (0.05 and 0.95) were considered, with constant inlet velocity u_{in} = 0.5 m s^{-1} and air gap thickness H_1 = 52 mm (mesh 3, serial processing).

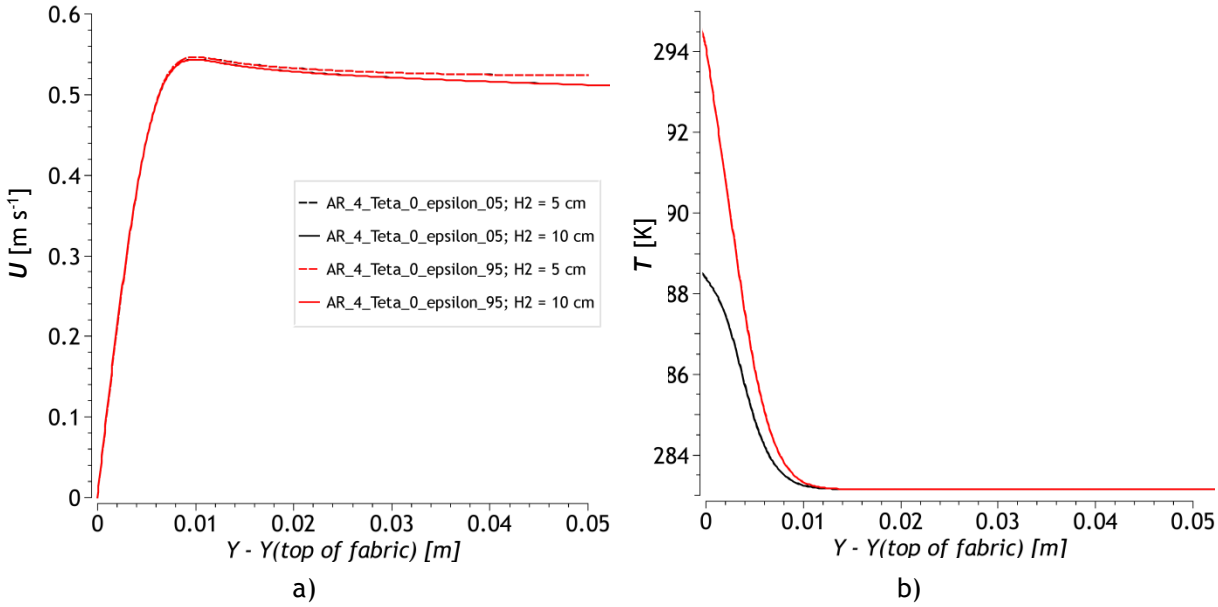

Figure A.4 - Velocity magnitude and temperature profiles along *y* for *AR* = 4 (location *x*/*L* = 0.75) and for each tested value of H_2 (0.05 and 0.10 m): a) velocity profiles; **b)** temperature profiles. Two different values of $\varepsilon_{inner\ fabric}$ (0.05 and 0.95) were considered, with constant inlet velocity u_{in} = 0.5 m s^{-1} and air gap thickness H_1 = 52 mm (mesh 3, serial processing). For temperature profiles (b), solid and dashed lines are superimposed; thus, differences between black and red curves are solely due to different emissivity values of the fabric.

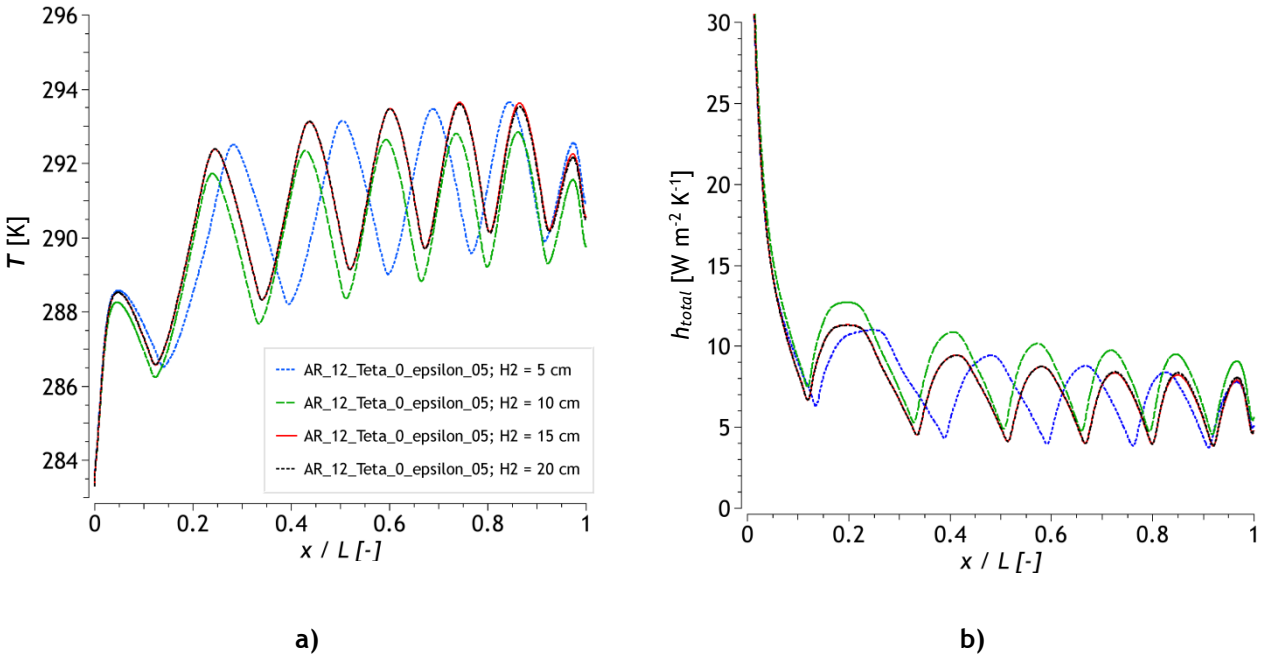

Figure A.5 - Local temperature and local heat transfer coefficient profiles along boundary 7 (top of the fabric) for *AR* = 12 and for each tested value of H_2 (0.05 to 0.20 m): a) temperature profiles; **b)** total heat transfer coefficient profiles. Two different values of $\varepsilon_{inner\ fabric}$ (0.05 and 0.95) were considered, with constant inlet velocity u_{in} = 0.5 m s^{-1} and air gap thickness H_1 = 52 mm (mesh 3, serial processing).

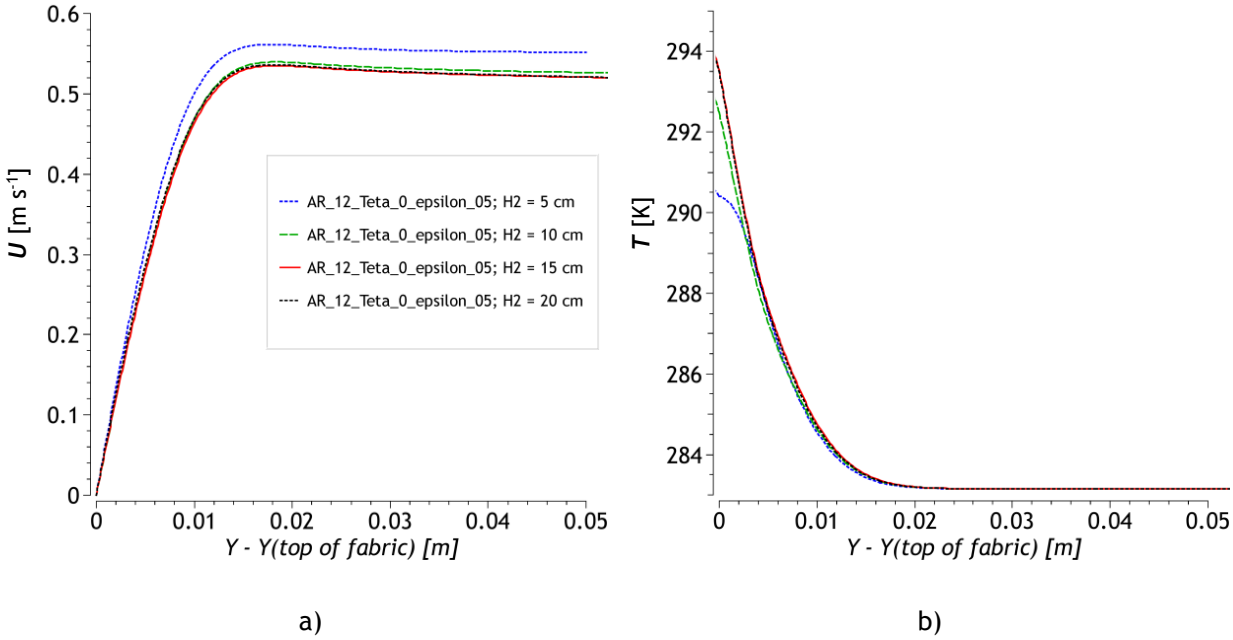

Figure A.6 - Velocity magnitude and temperature profiles along *y* for *AR* = 12 (location *x*/*L* = 0.75) and for each tested value of H_2 (0.05 to 0.20 m): a) velocity profiles; **b)** temperature profiles. Two different values of $\varepsilon_{inner\ fabric}$ (0.05 and 0.95) were considered, with constant inlet velocity u_{in} = 0.5 m s^{-1} and air gap thickness H_1 = 52 mm (mesh 3, serial processing).

Annex 5 – Parallel processing

Parallel processing was evaluated by increasing the number of processes from 1 (serial) up to 12 processes. Automatic partitioning of the mesh was allowed for each case (Fluent's default partitioning method). Computation time is presented in Table A.7 as a function of the number of processes and the number of elements in the mesh. The latter is dependent on the density of the mesh (mesh 2 through 4) and geometry of the enclosure (*AR* = 4 or *AR* = 12). Simulation results are compared in Table A.8 (average Nu_{total}), Figure A.7 (temperature contours for *AR* = 4) and Figure A.8 (temperature contours for *AR* = 12).

Regarding computation time, the optimal number of processes is 4 for *AR* = 4 with mesh 3, since a further increase in number of processes does not produce any significant decrease in computation time (Table A.7, AR_4_Teta_0_U_3_ epsilon_05, Mesh 3). Additionally, it is observed that, in some cases, convergence could not be attained (Table A.7, AR_4_Teta_0_U_3_epsilon_05, Mesh 4*), showing that convergence may be affected by the choice of number of processes.

It was further observed that the chosen number of processes could also alter the results. Indeed, average Nu_{total} values suffered changes, especially for high number of processes: from Table A.8, for mesh 4, there is an almost 16% change in Nu_{total} when increasing the number of processes from 2 to 12. Flow patterns were affected in such cases, most notably the number of roll cells, which either increased or decreased with increasing the number of processes (Figure A.7 and Figure A.8). Still, for parallel processing with 4 processes, the maximum difference in average Nu_{total} (relative to the solution obtained using serial computing) is always below 5% (Table A.8).

Table A.7 – Computation time as a function of number of processes (proc.) and number of elements in the mesh.

Case, Mesh	Nr. of elements	Serial	Parallel			
		Solver CPU time [min]	*Wall-clock time* [min]			
			2 proc.	4 proc.	8 proc.	12 proc.
AR_4_Teta_ 0_U_3_epsilon_05, Mesh 2	92,000	1.6	1.1	0.6	0.4	0.8
AR_4_Teta_ 0_U_3_epsilon_05, Mesh 3	368,000	20.0	9.3	3.8	4.1	3.3
AR_4_Teta_ 0_U_3_epsilon_05, Mesh 4 *	1,472,000	N/A [(a)]	150	101	N/A [(b)]	21
AR_12_Teta_ 0_epsilon_05, Mesh 3	1,104,000	1017	-	290	-	-

[(a)] - solver diverged after 18 iterations (5 minutes solver CPU time);
[(b)] – momentum and continuity residuals started oscillating within the first 30 iterations (6.557 sec/iteration).
(*) – energy residuals < $1x10^{-12}$.

Table A.8 – Average Nu_{total} at the skin as a function of number of processes (proc.) and according to mesh's size. "% diff." corresponds to the percentage difference to results from serial processing (or, when results were not available, to parallel with 2 processes).

Case	Serial	Parallel							
		2 proc.		4 proc.		8 proc.		12 proc.	
	Nu_{total}	Nu_{total}	% diff.	Nu_{total}	% diff.	Nu_{total}	% diff.	Nu_{total}	% diff.
AR_4_Teta_ 0_U_3_epsilon_05 (mesh 2)	6.81000	6.80996	-0.0006%	6.8099	-0.0015%	6.80996	-0.0006%	7.01879	3.07%
AR_4_Teta_ 0_U_3_epsilon_05 (mesh 3)	6.81176	6.81175	-0.0001%	6.81173	-0.0004%	6.81091	-0.0125%	6.81177	0.0001%
AR_4_Teta_ 0_U_3_epsilon_05 (mesh 4*)	N/A [(a)]	6.81122	-	6.81119	-0.0004%	N/A [(b)]	-	5.74462	-15.66%
AR_12_Teta_ 0_epsilon_05 (mesh 2)	6.76435	-	-	6.50589	-3.82%	-	-	-	-
AR_12_Teta_ 0_epsilon_95 (mesh 2)	16.30900	-	-	15.9809	-2.01%	-	-	-	-
AR_12_Teta_ 90_epsilon_05 (mesh 2)	4.61205	-	-	4.61203	-0.0004%	-	-	-	-
AR_12_Teta_ 90_epsilon_95 (mesh 2)	14.3423	-	-	14.3423	0.0000%	-	-	-	-

[(a)] - solver diverged after 18 iterations (5 minutes solver CPU time);
[(b)] – momentum and continuity residuals started oscillating within the first 30 iterations (6.557 sec/iteration).
(*) – energy residuals < $1x10^{-12}$.

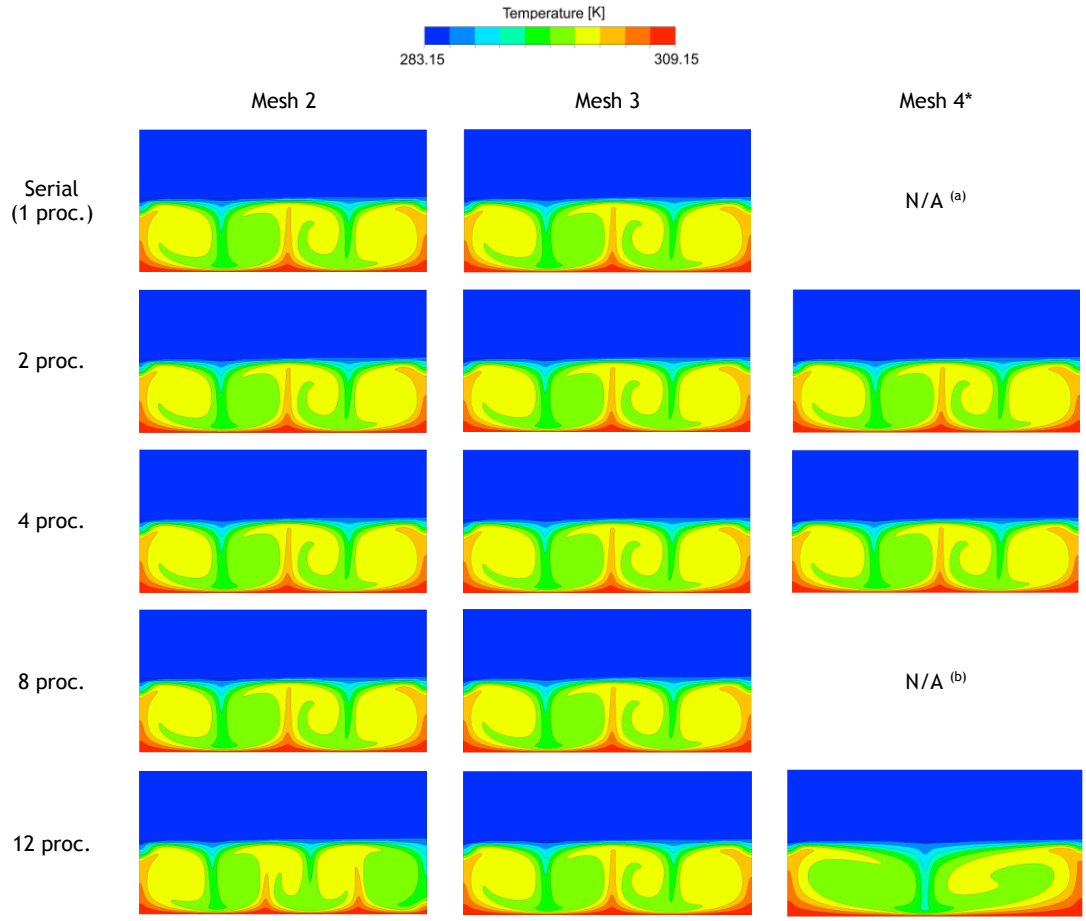

Figure A.7 - Temperature contours for case *AR_4_Teta_ 0_U_3_epsilon_05* and each mesh / number-of-processes combination. Notes: (a) - solver diverged after 18 iterations (5 minutes solver CPU time); (b) - momentum and continuity residuals started oscillating within the first 30 iterations (6.557 sec/iteration); (*) - energy residuals < $1x10^{-12}$.

In order to further investigate the influence of mesh partitioning (i.e. the distribution of grid elements within a given number of processes) on obtained solutions, manual partitioning was tested and compared to automatic partitioning. It was hypothesized that splitting the internal domain into several partitions, as obtained by automatic partitioning (Figure A.9), could be the cause of the above mentioned differences in results.

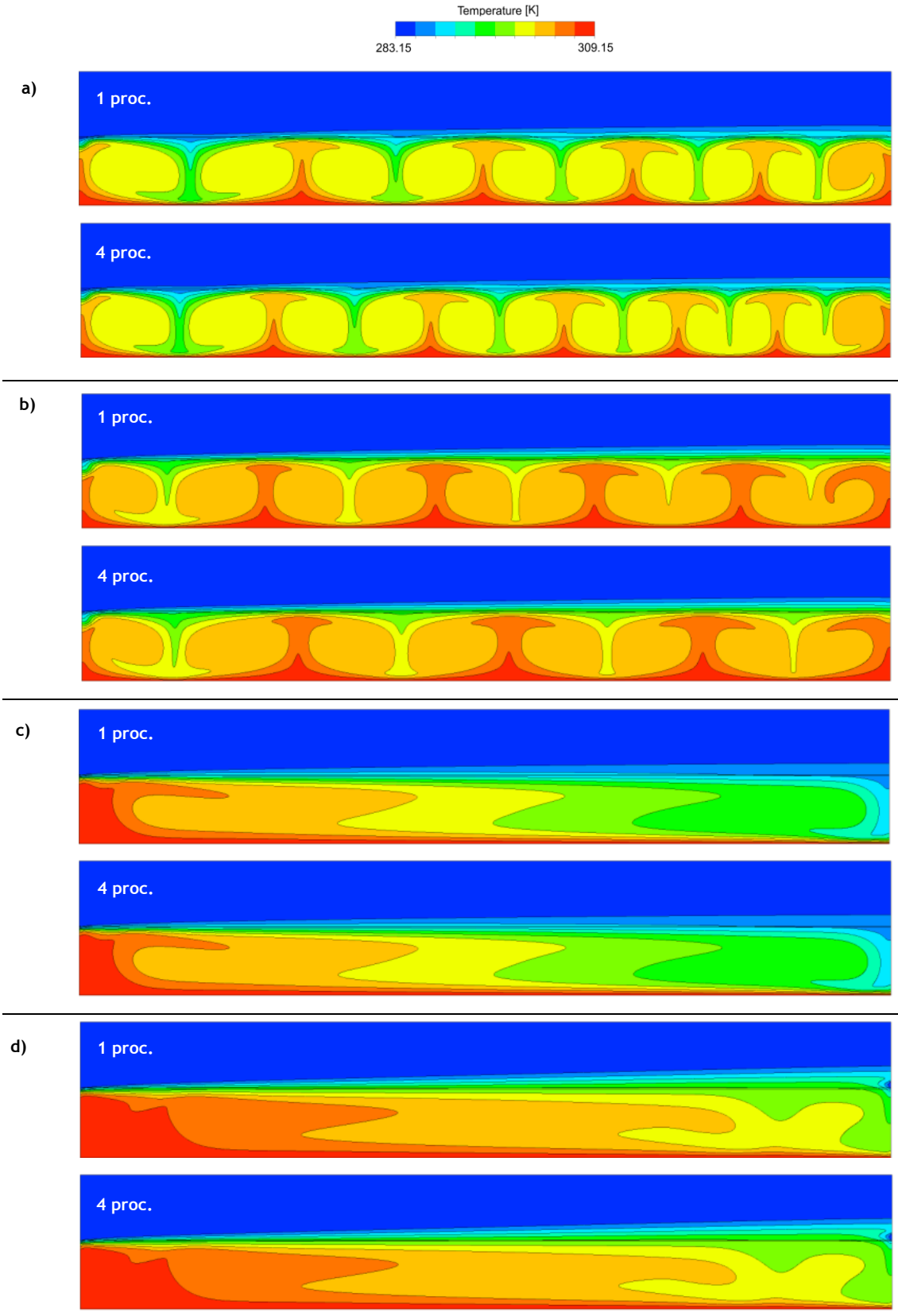

Figure A.8 - Resulting temperature fields for 1 process (serial) and 4 processes (parallel) for cases a) AR_12_Teta_0_epsilon_05, **b)** AR_12_Teta_0_epsilon_95, **c)** AR_12_Teta_90_epsilon_05, and **d)** AR_12_Teta_90_epsilon_95.

Figure A.9 - Contour for cell partition after automatic partitioning: yellow shading – partition ID 0; red shading – partition ID 1. Both external and internal domains are included (*AR* = 12).

Case *AR_12_Teta_0_epsilon_05* was selected for comparison of results obtained with manual partitioning to those obtained by serial processing. Resulting temperature profiles are presented in Figure A.10. It is noticed that results still differ in the number of roll cells, from serial processing to parallel with 2 manual partitions, even though *Nu* at the skin differed by less than 5%. Thus, these differences have apparently nothing to do with the previous splitting of the internal domain into several partitions. Therefore, as in Annex 4 – Validation of distance *H2*, we hypothesize that both results of Figure A.10 might be real, admitting the possible existence of multiple steady-states.

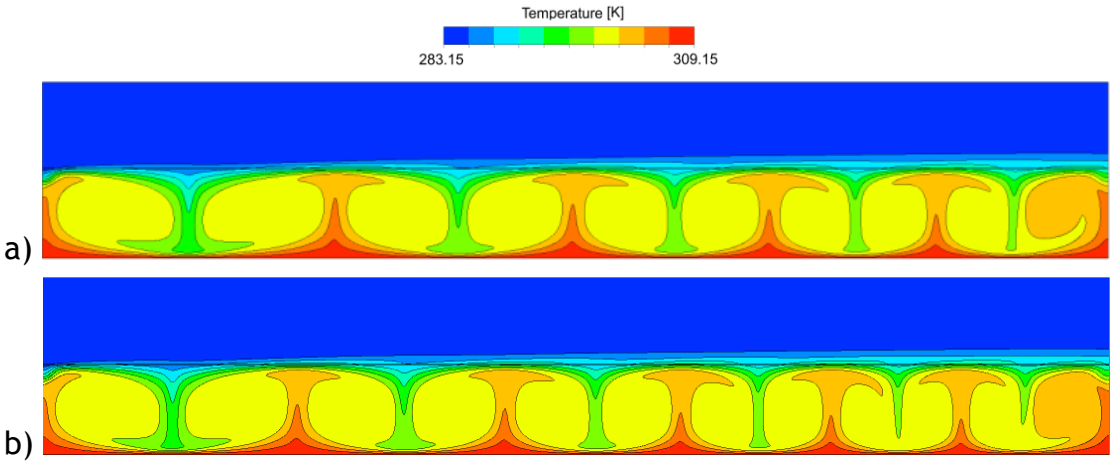

Figure A.10 - Comparison of temperature contours for a) serial processing and b) parallel processing with 2 manual partitions (case *AR_12_Teta_0_ epsilon_05*).

Finally, by taking all the above results into account, it was decided to avoid the influence of partitioning at any rate. Therefore, results considered throughout this study were all obtained by use of serial processing, though computationally more expensive than parallel processing.

Annex 6 – Mathematical formulae

In this section, definitions are given regarding several quantities presented throughout this study.

Local heat transfer coefficients (h_{total}, h_{conv} and h_{rad}) were calculated using:

$$h_a = \frac{q_a}{(T - T_c)}$$

Equation A.1

where q_a corresponds to total (*a* = *total*), convective (*a* = *conv*) or radiative (*a* = *rad*) heat flux. In ANSYS CFD-Post the following formula was used for h_{total}: "*= Heat flux / (Temperature - areaAve(Temperature)@boundary 8)*", where "*Heat flux*" should be replaced by "*Heat flux - Wall Radiative Heat Flux*" or simply "*Wall Radiative Heat Flux*", for convective and radiative heat transfer coefficients, respectively. Boundary 8 corresponds to the air inlet (Figure 2).

Average heat fluxes (average q_{total}, q_{conv} and q_{rad}) were calculated using:

$$q_{a,avrg} = \frac{1}{L} \times \int_{x=0}^{x=L} q_a \, dx$$

Equation A.2

where *L* corresponds to the length of the surface and q_a corresponds to total (*a* = *total*), convective (*a* = *conv*) or radiative (*a* = *rad*) heat flux. In ANSYS CFD-Post the following formula was used for average q_{total}: "*areaAve(Heat flux) @ boundary 1*", where "*Heat flux*" should be replaced by "*Heat flux - Wall Radiative Heat Flux*" or simply "*Wall Radiative Heat Flux*", for convective and radiative average heat fluxes, respectively. Boundary 1 corresponds to the skin (Figure 2).

Average Nusselt numbers (Nu_{total}, Nu_{conv} and Nu_{rad}) were obtained using:

$$Nu_a = \frac{q_{a,avrg}}{(k_f/H_1) \times (T_h - T_{avrg,\ inner\ fabric})}$$

Equation A.3

where $q_{a,avrg}$ corresponds to total (*a* = *total*), convective (*a* = *conv*) or radiative (*a* = *rad*) average heat flux. In ANSYS CFD-Post the following formula was used for Nu_{total}: "*areaAve(Heat flux *maxVal(Y)@boundary 3 / (Temperature - areaAve(Temperature)@boundary_3)) @ boundary 1 / 0.0260[W m^-1 K-1]*", where "*Heat flux*" should be replaced by "*Heat flux - Wall Radiative Heat Flux*" or simply "*Wall Radiative Heat Flux*", for convective and radiative *Nu*, respectively. Boundaries 1 and 3 correspond to the skin and the inner surface of the fabric, respectively (Figure 2).

Rayleigh number (*Ra*) was calculated using:

$$Ra = \frac{\beta \times g \times \left(T_h - T_{avrg,inner\ fabric}\right) \times {H_1}^3 \times \rho^2 \times Pr}{\mu^2}$$

Equation A.4

which, in ANSYS CFD-Post, corresponded to: "= 0.0033767 [K^-1] * 9.81 [m*s-1] * (areaAve(Temperature) @ boundary 1 - areaAve(Temperature) @ boundary 3)* (maxVal(Y) @ boundary 3)^3*(1.192[kg*m-3])^2 * 0.71 / (1.83E-5[Pa*s])^2". Boundaries 1 and 3 correspond to the skin and the inner surface of the fabric, respectively (Figure 2).

Mass imbalances were calculated using:

$$\%\ Mass\ Imbalance = \frac{\left(\int_{y=y_1}^{y=y_2} u\ dy\right)|_{x=0} - \left(\int_{y=y_1}^{y=y_2} u\ dy\right)|_{x=L}}{\left(\int_{y=y_1}^{y=y_2} u\ dy\right)|_{x=0}} \times 100$$

Equation A.5

where $y_1 = H_1 + H_{th}$ and $y_2 = y_1 + H_2$. In ANSYS CFD-Post, this was implemented as: "=(areaInt(Velocity u)@boundary 8-areaInt(Velocity u)@boundary 10)/areaInt (Velocity u) @ boundary 8*100". Boundaries 8 and 10 correspond to the inlet and the outlet, respectively (Figure 2).

Energy imbalances were calculated using:

$$\%\ Energy\ Imbalance\ |_{enclosure} = \frac{\left(\int_{x=0}^{x=L} q_{total}\ dx\right)|_{y=0} - \left(\int_{x=0}^{x=L} q_{total}\ dx\right)|_{y=H_1}}{\left(\int_{x=0}^{x=L} q_{total}\ dx\right)|_{y=0}} \times 100$$

Equation A.6

$$\%\ Energy\ Imbalance\ |_{fabric} = \frac{\left(\int_{x=0}^{x=L} q_{total}\ dx\right)|_{y=H_1} - \left(\int_{x=0}^{x=L} q_{total}\ dx\right)|_{y=H_1+H_{th}}}{\left(\int_{x=0}^{x=L} q_{total}\ dx\right)|_{y=H_1}} \times 100$$

Equation A.7

$$\%\ Energy\ Imbalance\ |_{exterior} = \frac{\left(\int_{x=0}^{x=L} q_{total}\ dx\right)|_{y=H_1+H_{th}} - \Delta E - Q_{rad}}{\left(\int_{x=0}^{x=L} q_{total}\ dx\right)|_{y=0}} \times 100$$

Equation A.8

$$\%\ Energy\ Imbalance\ (global) = \frac{\left(\int_{x=0}^{x=L} q_{total}\ dx\right)|_{y=0} - \Delta E - Q_{rad}}{\left(\int_{x=0}^{x=L} q_{total}\ dx\right)|_{y=0}} \times 100$$

Equation A.9

where ΔE corresponds to the enthalpy change between the inlet and the outlet (boundaries 8 and 10, respectively; Figure 2) and Q_{rad} corresponds to the radiative heat losses through the parallel slipping wall (boundary 9, Figure 2). These last four equations (Equation A.6 - Equation A.9) were implemented in ANSYS CFD-Post, respectively, as:

- *"=(areaInt(Heat flux)@boundary 1+areaInt(Heat flux)@boundary 3)/areaInt(Heat flux)@ boundary 1*100"*
- *"=(areaInt(Heat flux)@boundary 3+areaInt(Heat flux)@ boundary 7)/areaInt(Heat flux)@ boundary 3*100"*
- *"=(areaInt(Heat flux)@boundary 7+areaInt(Boundary Heat Flux Sensible)@boundary 8+areaInt(Boundary Heat Flux Sensible)@boundary 10 + areaInt(Heat flux)@boundary 9)/areaInt(Heat flux)@ boundary 1 *100"*
- *"=(areaInt(Heat flux)@boundary 1+areaInt(Boundary Heat Flux Sensible)@ boundary 8+areaInt(Boundary Heat Flux Sensible)@boundary 10 + areaInt(Heat flux)@ boundary 9)/areaInt(Heat flux) @ boundary 1 *100"*

where boundaries 1, 3, 7, 8, 9 and 10 correspond to the skin, inner fabric, outer fabric, inlet, parallel slipping wall and outlet, respectively (Figure 2).

Annex 7 – Polynomial regressions

Third order polynomial regressions for average Nu_{conv} on the skin were obtained (in Microsoft Excel) for the range of inclinations at which the single-cell flow mode was observed. Resulting expressions are given in the following table, for cases studied in sub-section 3.3. *Effects of Inclination.*

Table A.9 – Expressions for $Nu_{conv} = f(\theta)$, corresponding to 3rd order polynomial regressions obtained for ranges of θ associated with single-cell flow mode in the enclosure.

AR	$\varepsilon_{inner\ fabric}$	Range of θ	Nr. of datapoints	Expression	Correlation coefficient (r^2)
4	0.05	$-180° \leq \theta \leq -6°$	15	Nu_{conv} = 6.029252E-07xθ^3 - 1.677495E-04xθ^2 + - 3.223837E-02xθ + 4.140118	0.9998619
4	0.05	$7° \leq \theta \leq 180°$	14	Nu_{conv} = -7.753615E-07xθ^3 - 1.030866E-04xθ^2 + + 2.676182E-02θ + 4.038508	0.9996612
4	0.95	$-180° \leq \theta \leq -6°$	15	Nu_{conv} = 2.775270E-07xθ^3 - 2.268078E-04xθ^2 + - 3.368392E-02xθ + 3.902974	0.9998719
4	0.95	$9° \leq \theta \leq 180°$	12	Nu_{conv} = -7.296132E-07xθ^3 - 7.507176E-05xθ^2 + + 2.226075E-02xθ + 3.687811	0.9992779

Annex 8 - Grid sensitivity tests

Four meshes were tested for the configuration under study, each mesh with a 4-fold increase in number of elements relative to the previous (please refer to Annex 1 – Meshing parameters for more details regarding meshing). The particular case of AR = 4, with high air velocity (u_{in} = 3.0 m s^{-1}) and low emissivity ($\varepsilon_{inner\ fabric}$ = 0.05), was used for the purpose of testing grid sensitivity, since higher gradients are expected in such case, as noted before by Couto & Mayor (2013). Two inclination values were tested: θ = 0º and θ = 90º. Results are compared in Table A10 (Nusselt numbers and maximum velocity components), Figure A.11 (profiles for temperature and heat transfer coefficient) and Figure A.12 (external velocity profiles). Lower energy residuals were set for mesh 4 ("Mesh 4 *" corresponds to a criterion of $1x10^{-12}$ and "Mesh 4 **" to $5x10^{-12}$), since results had been observed to vary with the number of iterations, i.e. solutions were not yet fully converged when the energy criterion of $1x10^{-9}$ was used for mesh 4.

From Table A10, small changes in Nu_{total} ([15]) and maximum velocity components suggest that results for mesh 2 are grid independent. From Figure A.11, temperature profiles practically overlap for meshes 2, 3 and 4*. However, in Figure A.12, external velocity profiles for mesh 3 are seen to better match those of the densest mesh 4, compared to mesh 2. Therefore, since only a few selected cases were tested for grid independence, mesh 3 was chosen (and not mesh 2) for further analysis.

In addition to grid independency, the level $1x10^{-9}$ for energy residuals is seen to be adequate for mesh 3, since results are highly similar to those of a denser mesh 4, the later with lower energy residuals (as mentioned above).

[15] Nusselt numbers were calculated in ANSYS CFD-Post using the formula: *"=areaAve(Heat Flux/(Temperature-areaAve(Temperature)@boundary3))@boundary1*maxVal(Y)@boundary3/0.0260[W m^-1 K^-1]"*, where 0.0260 W m^{-1} K^{-1} corresponds to the conductivity of air.

Table A10 - Comparison of Nu_{total} and maximum velocities for several tested meshes.
Figures between brackets correspond to absolute percentage deviation relative to mesh 3.
(*) – energy residuals inferior to $1x10^{-12}$; (**) - energy residuals inferior to $5x10^{-12}$.

	Nu_{total} (on skin) [-]		u_{max} (enclosure) [m s^{-1}]		v_{max} (enclosure) [m s^{-1}]	
AR_4_Teta_ 0_U_3_epsilon_05						
Mesh 1 (23,000 elements)	5.7398	(15.74)	0.105	(3.96)	0.065	(42.48)
Mesh 2 (92,000 elements)	6.8100	(0.03)	0.101	(0.00)	0.112	(0.88)
Mesh 3 (368,000 elements)	6.8117	-	0.101	-	0.113	-
Mesh 4 * (1,472,000 elements)	6.8112	(0.01)	0.101	(0.00)	0.113	(0.00)
AR_4_Teta_90_U_3_epsilon_05						
Mesh 1 (23,000 elements)	5.7354	(0.16)	0.100	(0.99)	0.057	(1.72)
Mesh 2 (92,000 elements)	5.7321	(0.11)	0.101	(0.00)	0.057	(1.72)
Mesh 3 (368,000 elements)	5.7261	-	0.101	-	0.058	-
Mesh 4 ** (1,472,000 elements)	5.7330	(0.12)	0.101	(0.00)	0.057	(1.72)

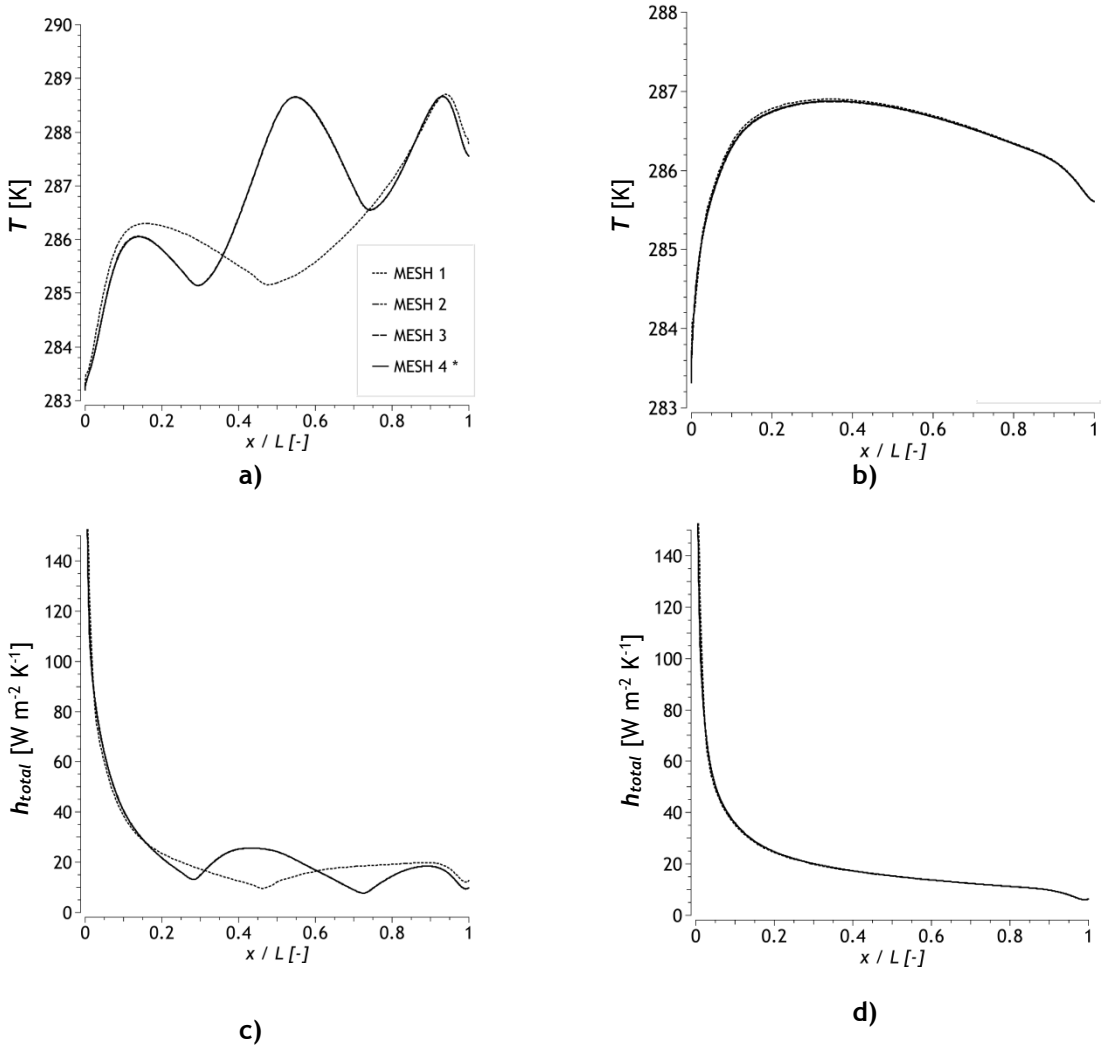

Figure A.11 - Comparison between each tested mesh regarding temperature and total heat transfer coefficient profiles along boundary 7 (top of the fabric), for cases: a,c) AR_4_Teta_ 0_U_3_epsilon_05; **b,d)** AR_4_Teta_ 90_U_3_epsilon_05.

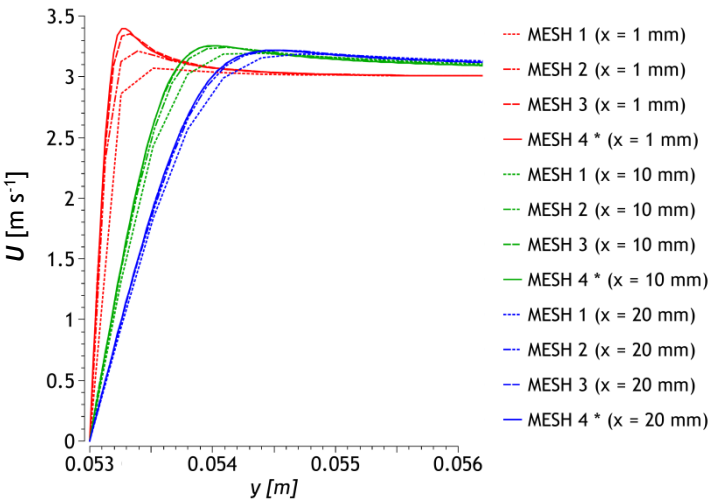

Figure A.12 - Comparison of velocity profiles in the external domain C for each tested mesh, at several values of x (1, 10 and 20 mm). Only results for case AR_4_Teta_ 0_U_3_epsilon_05 are represented (results for AR_4_Teta_ 90_U_3_epsilon_05 closely resemble these profiles and were therefore omitted).

Annex 9 – Validation of computational methods

The present numerical approach was validated in a stepwise manner. Comparison of results with those of reference studies concerned: natural convection in both horizontal (Corcione, 2003; Couto & Mayor, 2013) and vertical enclosures([16]) without radiation (Davis, 1983), natural convection coupled with radiation (Vivek et al., 2012) and, finally, natural convection coupled with radiation and external forced convection (Couto & Mayor, 2013). For each validation step, results are presented in Table A.11, Table A.12, Figure A.13 and Figure A.14, respectively.

Good agreement could be found between present results and reference results: percentage differences in averaged values are lower than 1% and local profiles closely match. Thus, the present numerical results can be regarded as valid.

Table A.11 - Validation for natural convection in horizontal enclosures (without radiant exchange): comparison of average *Nu* ([17]) at the hot horizontal wall obtained in this study to those obtained by reference studies, for aspect ratio up to *AR* = 2.

AR [-]	***Ra*** [-]	Nu_{avrg} [-]		
		This study	Couto & Mayor 2013	% Diff.
0.66	$1x10^5$	2.948	2.954	-0.22
1	$1x10^5$	3.906	3.911	-0.12
2	$1 x10^3$	0.999	1.000	-0.14
2	$1 x10^4$	2.403	2.404	-0.04
2	$1 x10^5$	4.418	4.429	-0.25
2	$1 x10^6$	7.382	7.363	0.26

[16] Horizontal enclosures are heated from below and cooled from above, with adiabatic sidewalls, whereas vertical enclosures have active sidewalls and adiabatic top and bottom walls.

[17] Nusselt number was calculated for horizontal walls according to Corcione (2003): $Nu = |Q| \times H/(L \times k(T_h - T_c) \times 1[m])$, where the denominator is multiplied by the depth of the domain (1 m in the z-direction) and $|Q|$ stands for the absolute of heat transfer rate at the hot wall, obtained in ANSYS CFD-Post using the formula: "*=areaInt(Heat flux)@hot_wall*".

Table A.12 - Validation for natural convection in vertical enclosures (without radiant exchange): comparison of average *Nu*([18]) at the hot vertical wall obtained in this study to those obtained by Davis 1983, for several values of Rayleigh number. Aspect ratio of the enclosure: *AR* = 1 (square enclosure).

Ra [-]	*Nu* $_{avrg}$ [-]		
	This study	Davis 1983	% Diff.
$1x10^3$	1.116	1.117	0.128
$1x10^4$	2.244	2.238	-0.254
$1x10^5$	4.510	4.509	-0.017
$1x10^6$	8.817	8.817	-0.002

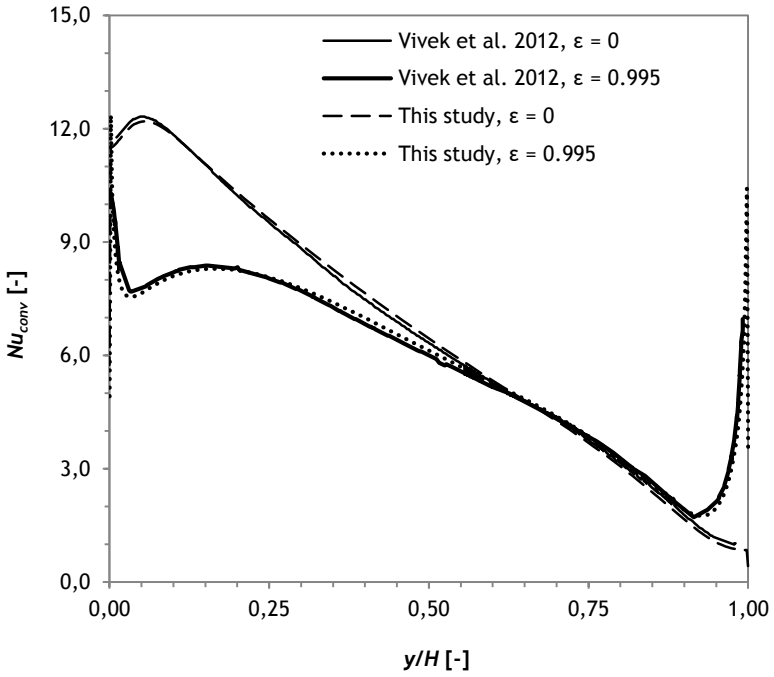

Figure A.13 - Validation for natural convection in enclosures, coupled with radiation: comparison of local convective *Nu* ([19]) along the hot wall obtained in this study to results obtained by Vivek et al. 2012 (as cited by Couto & Mayor 2013). Two emissivity values for the walls were considered (ε = 0 and ε = 0.995). Rayleigh number corresponds to *Ra* = $3.56x10^5$. Aspect ratio of the enclosure: *AR* = 1 (square enclosure).

[18] Nusselt number was calculated for vertical walls according to Corcione (2003): $Nu = |Q|/(k(T_h - T_c) \times 1[m])$, where the denominator is multiplied by the depth of the domain (1 m in the z-direction) and $|Q|$ stands for the absolute of heat transfer rate at the hot wall, obtained in ANSYS CFD-Post using the formula: *"=areaInt(Heat flux)@hot_wall"*.

[19] Local convective Nusselt number at the hot vertical wall was calculated as: $Nu_{conv} = (q_{total} - q_{rad}) \times H/[k(T_h - T_c)]$, where q_{total} and q_{rad} were directly exported from ANSYS Fluent as "Total Surface Heat Flux" and "Radiation Heat Flux", respectively.

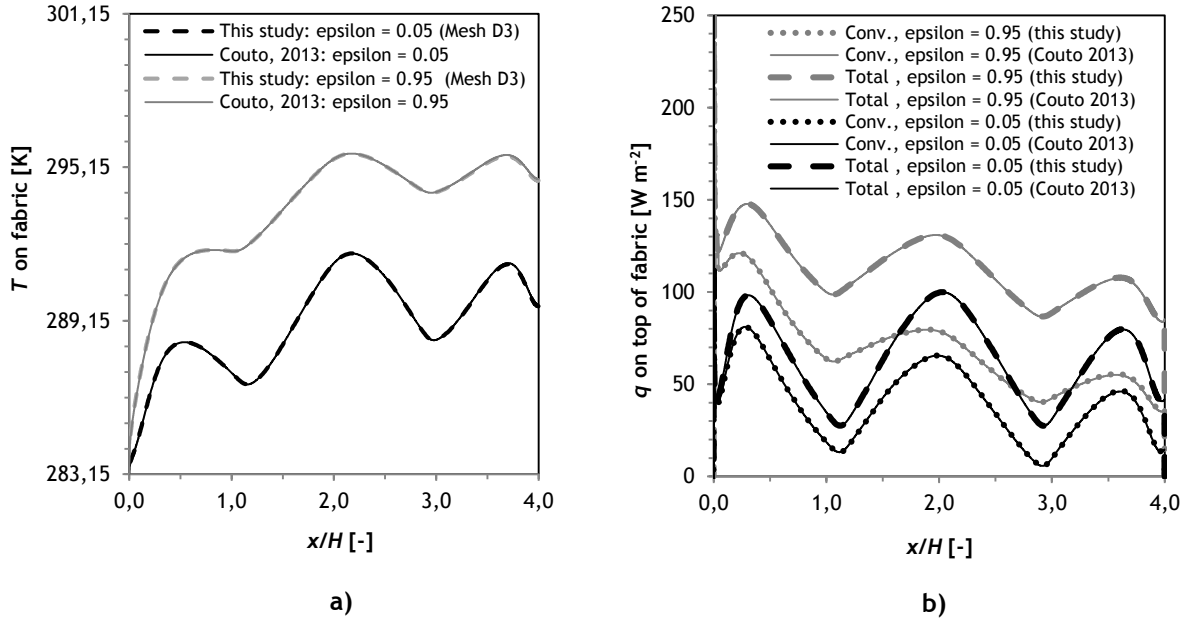

Figure A.14 - Validation for natural convection coupled with radiation and external forced convection: a) comparison of temperature profiles along the top of the fabric to those obtained by Couto & Mayor 2013; **b)** comparison of local heat fluxes (convective and total) along the top of the fabric to those obtained by Couto & Mayor 2013. Two values of inner fabric emissivity were considered (0.05 and 0.95). Geometrical configuration corresponds to the one presented above in section 2. *Materials and methods* (AR = 4; H_1 = 52 mm; θ = 0º).

Annex 10 – Flow pattern inversion

From positive to corresponding negative inclination values, flow patterns in the microclimate (domain A of Figure 1a) were inverted in the *x*-direction. This is exemplified in temperature and velocity contours of Figure A.15, for inclination values θ = +90º and θ = -90º.

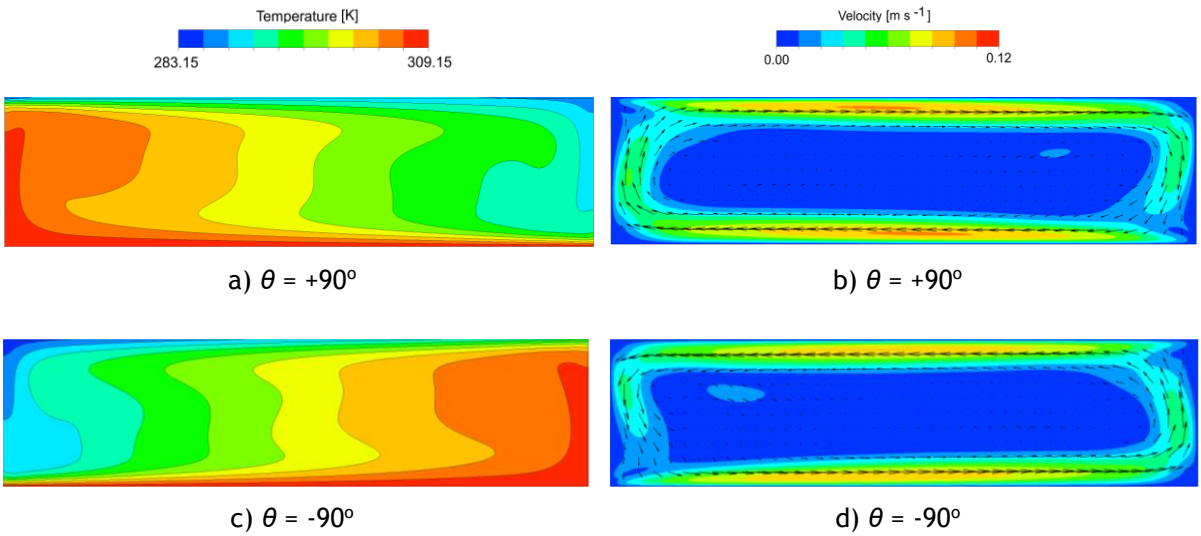

a) θ = +90º b) θ = +90º

c) θ = -90º d) θ = -90º

Figure A.15 - Temperature and velocity contours in the air gap (domain A, Figure 1a) for inner fabric emissivity of 0.05 and two inclination values: a-b) θ = +90º ; c-d) θ = -90º.